Scuola di dottorato in Ingegneria “Leonardo da Vinci”

Corso di Dottorato di Ricerca in

TELERILEVAMENTO

Tesi di Dottorato di Ricerca

Photonic Technologies for Radar and Telecommunications Systems

PhD Dissertation of:

Francesco Laghezza

Advisory Committee:

Prof. Fabrizio Berizzi

Dr. Antonella Bogoni

2010-2012

SSD ING-INF/03

This page was intentionally left blank

To Giulia and my family

This page was intentionally left blank

CONTENT

ACRONYM LIST

ADC *Analog-to-Digital Converter*

AF *Autocorrelation Function*

BW *Bandwidth*

CO Centralized Office

CW *Continuous-Wave*

DC *Direct Current*

DDS *Direct Digital Synthesizer*

DFBG *Dual Fiber Bragg Grating*

D-MZM *Dual-output Mach Zehnder Modulator*

EDFA *Erbium-Doped Fiber Amplifier*

EHF *Extremely High Frequency*

EMI *Electromagnetic Interference*

ENOB *Effective Number of Bits*

E\O *Electro-Optical*

EOM *Electro-Optical Modulator*

ESA *Electrical Spectrum Analyzer*

EVM *Error Vector Magnitude*

FBG *Fiber Bragg Grating*

FCC *Federal Comunication Committee*

FFT *Fast Fourier Transform*

GPON *Gigabit Passive Optical Network*

HFR *Hybrid Fibre-Radio*

HPA *High Power Amplifier*

IF *Intermediate Frequency*

LSB *Lower-Side Band*

MIC *Microwave Integrated Ciscuits*

MLL *Mode Locked Laser*

MMB *Millimeter Band*

MZM *Mach Zehnder Modulator*

MWP *Microwave Photonics*

NF *Noise Figure*

OBFN *Optical Beamforming Network*

OBPF *Optical Band-Pass Filter*

OFDM *Orthogonal Frequency Division Multiplexing*

O\E *Opto- Electrical*

OPLL *Optical Phase-Lock Loop*

OSSB *Optical Single Sideband*

PAA *Phased Array Antenna*

PADC *Photonic Analog to Digital Conveter*

PD *Photodiode*

PRBS *Pseudo Random Binary Sequence*

PRF *Pulse Repetition Frequency*

PRI *Pulse Repetition Interval*

PW *Pulse Width*

QAM *Quadrature Amplitude Modulation*

RAU *Remote Acces Unit*

RIN *Relative Intensity Noise*

RF *Radio Frequency*

SINAD *Signal-to-Noise & Distortion*

SDR *Software Defined Radio*

SFDR *Spurious-Free Dynamic Range*

SNR *Signal-to-Noise Ratio*

SSA *Signal Source Analyzer*

TDM *Time Division Multiplexing*

TIA *Trans-Impedance Amplifier*

TLS *Tunable Laser Source*

TTD *True Time Delay*

VCO *Voltage Controlled Oscillator*

VSA *Vector Signal Analyzer*

VSG *Vector Signal Generator*

UHF *Ultra High Frequency*

USB *Upper-Side Band*

UTC-PD *Uni-traveling-carrier photodiodes*

UWB *Ultra Wide Band*

UWBoF *Ultra Wide Band over Fiber*

VCSEL *Vertical Cavity Surface Emitting Lasers*

WDM *Wavelength Division Multiplexing*

LIST OF FIGURES

This page was intentionally left blank

INTRODUCTION

The growing interest in flexible architectures radio and the recent progress in the high speed digital signal processor make a software defined radio system an enabling technology for several digital signals processing architecture and for the flexible signal generation. In this direction wireless radar\telecommunications receiver with digital backend as close as possible to the antenna, as well as the software defined signal generation, reaches several benefits in term of reconfigurabilty, reliability and cost with respect to the analogical front-ends. Unfortunately the present scenario ensures direct sampling and digital downconversion only at the intermediate frequency. Therefore these kinds of systems are quite vulnerable to mismatches and hardware non-idealities in particular due to the mixers stages and filtering process. Furthermore, since the limited input bandwidth, speed and precision of the analog to digital converters represent the main digital system's bottleneck, today's direct radio frequency sampling is only possible at low frequency. On the other hand software defined signals can be generated exploiting direct digital synthesizers followed by an up-conversion to the desired carrier frequency. State-of-the-art synthesizers (limited to few GHz) introduce quantization errors due to digital-to-analog conversion, and phase errors depending on the phase stability of their internal clock. In addition the high phase stability required in modern wireless systems (such as radar systems) is becoming challenging for the electronic RF signal generation, since at high carrier frequency the frequency multiplication processes that are usually exploited reduce the phase stability of the original RF oscillators. Over the past 30 years microwave photonics (MWP) has been defined as the field that study the interactions between microwave and optical waves and their applications in radar and communications system as well as in hybrid sensor's instrumentation. As said before software defined radio applications drive the technological development trough high speed\bandwidth and high dynamic range systems operating directly in the radio frequency domain. Nowadays, while digital electronics represent a limit on system performances, photonic technologies perfectly engages the today's system needs and offers promising solution thanks to its inherent high frequency and ultrawide bandwidth. Moreover photonic components with very high phase coherence guarantees highly stable microwave carriers; while strong immunity to the electromagnetic interference, low loss and high tunability make a MWP system robust, flexible and reliable. Historical research and development of MWP finds space in a wide range of applications including the generation, distribution and processing of radio frequency signals such as, for example, analog microwave photonic link, antenna remoting, high frequency and low noise photonic microwave signal generation, photonic microwave signal processing (true time delay for phased array systems, tunable high Q microwave photonic filter and high

speed analog to digital converters) and broadband wireless access networks. Performances improvement of photonic and hybrid devices represents a key factor to improve the development of microwave photonic systems in many other applications such as Terahertz generation, optical packet switching and so on. Furthermore, advanced in silicon photonics and integration, makes the low cost complete microwave photonic system on chip just around the corner. In the last years the use of photonics has been suggested as an effective way for generating low phase-noise radio frequency carriers even at high frequency. However while a lot of efforts have been spent in the photonic generation of RF carriers, only few works have been presented on reconfigurable phase coding in the photonics-based signal generators. In this direction two innovative schemes for optically generate multifrequency direct RF phase modulated signals have been presented. Then we propose a wideband ADC with high precision and a photonic wireless receiver for sparse sensing. This dissertation focuses on microwave photonics for radar and telecommunications systems. In particular applications in the field of photonic RF signal generation, photonic analog to digital converters and photonic ultrawideband radio will be presented with the main objective to overcome the limitations of pure electrical systems. Schemes and results will be further detailed and discussed. The dissertation is organized as follows. In the first chapter an overview of the MWP technologies is presented, focusing the attention of the limits overcame by using hybrid optoelectronic systems in particular field of applications. Then optoelectronic devices are introduced in the second chapter to better understand their role in a MWP system. Chapters 3,4, and 5 present results on photonic microwave signal generation, photonic wideband analog to digital converters and photonic ultrawideband up\down converter for both radar and telecommunications applications. Finally in the chapter 6 an overview of the photonic radar prototype is given.

CHAPTER 1

1. OVERVIEW ON MICROWAVE PHOTONICS TECHNOLOGIES AND APPLICATIONS

In the last decades of the 20th century the cross fertilization between fiber-optic and radio wave engineering starts to create new interdisciplinary macro-area called Microwave Photonics. Basically the main objective of the MWP technology is to reaching improved performances, emerging functionalities and new application fields in modern wireless systems that cannot be immediately achieved by using classical and univocal technologies [1][2][3]. The basic concept of the MWP system is based on the radio over fiber distribution with electro-optical and opto-electrical conversions at the ends of the link. The key advantages of a MWP system are high speed and high bandwidth (with consequently high transfer data rate), very high dynamic range, reduced cost, size and weight, low power consumption and attenuation, reliability, tunability and high immunity to the electromagnetic interference [4].

Modulation, control and detection of high frequency and high bandwidth signals represent the key factors of photonic devices and vibrant research field for rapidly growing manufacturing capability. For example interesting progress has been made in the field of the laser sensors (semiconductor lasers, cavity lasers, MLL, VCSEL) and their bandwidth for direct modulation and injection locking [5][6]. For the external modulation several investigations have been made in the last decades concerning lithium niobate interferometric external modulators with more than 40GHz of bandwidth [7][8].

High speed photodetectors with high responsivities, bandwidths and optical power-handling capability are used for the detection of optical signals in MWP systems [9][10]. Recently the UTC-PD overcomes the saturation power limitation, given by the nonlinearity of the photodetector response [11][12].

Talking about the MWP applications, EW systems for defense applications drive the research activity in this filed for the signal generation, distribution and

processing up to the today's concepts of the future access networks for broadband communications [13]. To better explain the helpful contribution of the MWP for RF applications in the following text a brief review on the most important microwave photonics techniques is given. In the Figure 1.1 the four macro-areas of MWP and their relative application fields are presented.

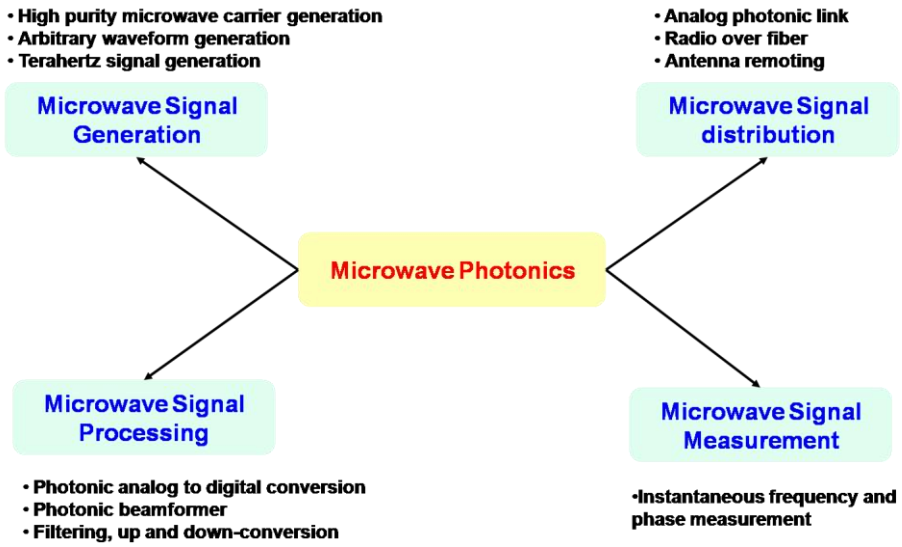

Figure 1.1 MWP macro-areas and applications

Radio over Fiber

The low loss, broadband bandwidth of the state of the art optical fibers represent a well known and very interesting solution for the distribution of wide band radio signals over optical fiber (compared with electrical media) for deployed systems in many practical applications such as antenna remoting (Figure 1.3), wireless signal distribution (Figure 1.2) and UWBoF for GPON. As example the weight and attenuation are typically 1.7 kg km–1 and 0.5 dB km–1 for optical fibre and 567 kg km–1 and 360 dB km–1 at 2 GHz for a coaxial cable.

The integration of fibre-optic and wireless networks for the HFR is the more successful application of RoF technology, to distribute telecommunication standards and to provide untethered access to broadband wireless communications. HFR networks have been deployed in the last decade due to the increasing demand of high-bitrates communication services in today's access network [1][2][14][15]. The most important benefit is the ability to reduce system complexity by using a centralized architecture and flexible approach for remotely interfacing to multiple simplified antennas as close as possible to the final users.

Radio frequency signal processing is represented by a shared centralized location also called Central Office. Then state of the art optical fibers are used to distribute

multiple signals (or communication standards) to the remote access units (Figure 1.2). RAUs can be drastically simplified, as they only need to perform optoelectronic conversion, filtering and amplification functions allowing important cost reductions. It is possible to use WDM in order to increase capacity and to implement advanced network features such as dynamic allocation of resources. The CO and the RAU perform electro-optical and opto-electronic conversion respectively. E/O conversion is achieved employing either injection locking or external Mach Zehnder modulators. O/E conversion is done employing photodetectors or TIA.

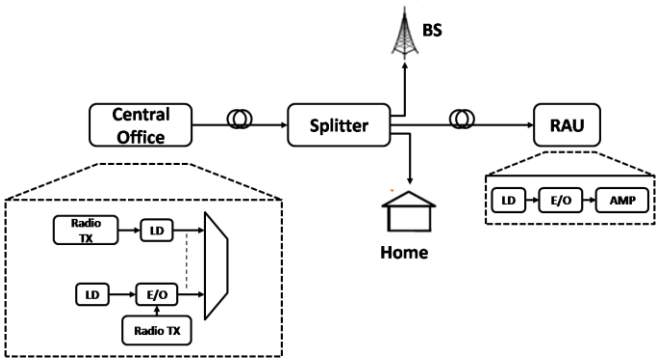

Figure 1.2 Basic scheme of RoF and UWBoF system

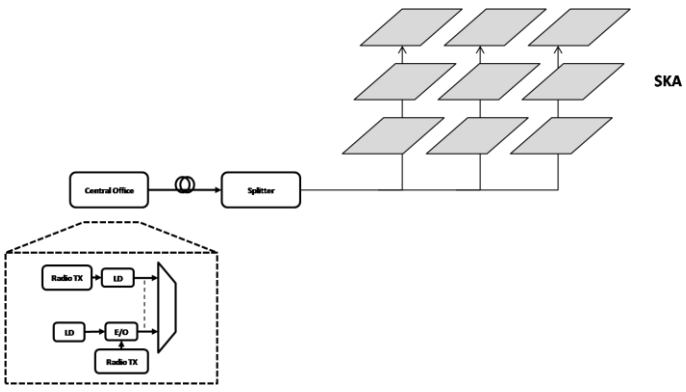

Figure 1.3 Basic scheme of RoF antenna remoting for Square Kilometers Array (SKA)

Furhtermore thanks to the low loss and broad bandwidth of the state-of-the-art fiber, the distribution of UWB signals [16][17] over fiber, or UWB-over-fiber (UWBoF) [18][19][20], is also considered a promising solution for the UWB indoor communications or IR systems from 3.1 GHz to 10.6 GHz (FCC compliance) and for the 60GHz WiGig standard [21].

To distribute radio signals over optical fiber a few key points have to be taken into account such as the dynamic range, the noise figure and gain of the optical link

directly related to the device's parameters as RIN, photodetector's responsivity, phase noise, input power and more. In this direction, considering different trade-offs and figures of merit few possible approaches to transporting radio signals over optical fibre, is implemented: baseband-over-fi bre, intermediate-frequency(IF)-over-fi bre and RF-over-fi bre. Since the photonic link is considered a good solution for radio signal distribution, problems related to link gain and noise, figure and dynamic range are under investigation. Several techniques provided for link optimization by using feed-forward linearization, predistortion, MZM hardware and software linearization, balanced detection, bias control are reported in [22][23][24][25][26][27][28].

Optical Beamforming

Phased array antennas (PAA) play an important role in modern multifunctional radar, sonar and wireless communication systems with no moving part (electroning sttering) and less drag. The basic principle is the control of the relative phase of an RF signal between successive radiating elements of an antenna array. Therefore a beam-forming network is used to create the required phase shifts at the input of the antenna in order to create an oriented beam. The bottolnecks of a PAA could be finded in the operational bandwidth often limited to narrowband functionalities due to the well know squint phenomenon which cause frequency depended orientation and beam corruption[29][30]. Desiderable solution should have the usage of a true time delay lines to provide real delay and wideband operation.

In a phased-array, photonic TTD beamforming by using optical fiber networks (called OBFN) is the best way to provide squintfree electronic beam steering for wideband applications (see Figure 1.4).

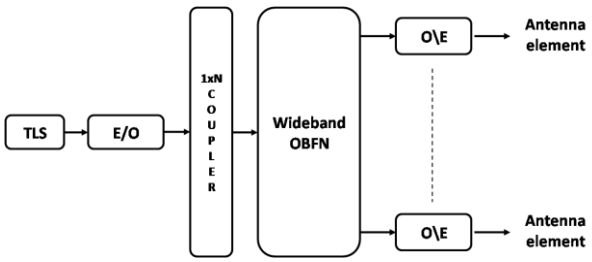

Figure 1.4 Basic scheme of optical beamforming system

A first TTD network has fixed-length optical fibres as the delay elements and N sets of switchable fi bre-optic delay lines with multiple sources to create an N-bit delay [31]. After that TTD networks incorporated high-dispersion optical fibres was used.The dispersion property of the fibre-optic link creates variable delays for

variable wavelengths of a TLS [32]. To reduce the size, cost and drag of the fiberoptic prism, the dispersive delay lines have been replaced by FBG delay. In this way the time delay for the RF signal can be continuously steered by sweeping the wavelength of a TLS [33][34][35][36]. If the FBG arrays in the delay lines are replaced by linearly chirped FBGs, a true-time delay beamforming system with continuous beam steering capability can be realized [37][38][39].

Photonic Microwave Signal Generation

A frequency-agile RF or mm-wave system with very low phase and amplitude noise on the transmitted signal is an important requirement for radar and wireless communications with enhanced performances in terms of sensitivity and precision. In a conventional system, the spectral purity of the microwave signal also depends on the frequency stability of the local oscillators. In order to satisfy the microwave regime and to improve the RF signal stability, the combination of different type of oscillators (i.e. acoustic and electrical) is necessary. Some of the weaknesses of this implementation is the usage of low frequency resonant modes, the necessity of a great number of multiplication stages, and the strongly frequency dependent performance of microwave signal in terms of amplitude and phase jitter. The aim of the historical proposed photonic approaches is to give an alternative way for a flexible microwave signal generation suitable for high frequencies systems (THz signals) [40][41].

The optical heterodyning concept is the basic principle of the microwave or mm-wave signal generation. It is often based on the beating in a photodetector of two optical waves of different wavelengths (Figure 1.5), where the spacing of the two optical waves represents the corresponding generated frequency in the electrical domain [42][43].

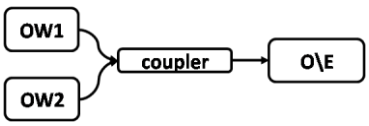

Figure 1.5 Basic scheme of photonic microwave signal generation

In this direction four different techniques have been proposed and demonstrated: the optical injection locking, the optical phase-lock loop, the microwave generation using external modulation, and finally the dual-wavelength laser source.

An optical injection locking system consists of a master laser and two slave lasers. The signal at the output of the master laser (driven by a reference RF signal) is then injected into the two slave lasers which are wavelength-locked by the +nnd-

order and -nnd-order sidebands from the output of the master laser producing RF signals after the photodiode [44]. The OPLL instead, is based on the fact that the optical phase of one laser is actively locked to the phase of a second laser by using a feedback network, where the obtained beating phase is compared with that of an RF reference given from a microwave oscillator [45][53]. High-quality microwave signals (with fixed carrier or frequency tunability) can also be generated based on external modulation using a Mach-Zehnder modulator, fixed or tunable laser sources, optical filters and a photodetector [46][47][48][49][50][52][53]. On the other hand by using a dual wavelength laser source with wavelengths difference set to the desired RF carrier is possible to generate microwave signals with good phase stability since wavelengths are generated starting from the same cavity [54].

Furthermore the photonic generation of arbitrary waves for applications including pulsed radar, UWB, optical \electronic measurements and ground penetrating radar is an attractive and growing research field [55][56][57].

Photonic Analog-to-Digital Converters

The software defined radio paradigm, benefiting of adaptive digital signal processing, represent the unique way to increment system reconfigurability and performances. To do that great enhancements have been made in the field of the high speed digital signal processing but the real system's bottleneck is represented by the UWB analog-to-digital converters which are often limited in speed and precision by the sampling clock jitter and analog input bandwidth [58][59].

The photonic ADCs present key advantages with respect to the classical approaches, which include more precise sampling times, narrower sampling apertures, and the ability to sample without contaminating the incident signal. Recently, the use of optical techniques to achieve photonic ADC has attracted great interest in particular regarding the photonic sampling and electronic quantizing ADCs where UWB sampling is performed in the optical domain while quantization is performed in the electrical once. The great success of the photonic sampled and electronically quantized ADCs is thanks to the technological breakthrough in mode-lock laser sources, able to producing very low jitter, ultra-narrow and high-repetition-rate optical pulses. Basically a PADC is composed by an ultra-stable pulsed laser, an external optical modulator, and a high speed detector (see Figure 1.6).

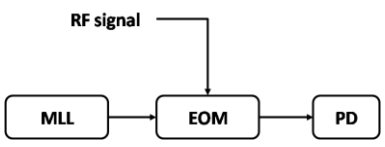

Figure 1.6 Basic scheme of PADC.

Since the system is similar to an analog photonic link its performances are characterized by the link SNR, SFDR, modulator bandwidth and index, photodiode responsivity and so on, but has the potential for a sampling time equal to the optical pulse width and a sampling jitter equal to the laser jitter. In addiction the system bandwidth and overall dynamic range capability (given by the MZM and the PD) may eliminate the need for downconverting and filtering stages to reduce the carrier frequency of the RF signal to an intermediate frequency allowing a simplified system with reduced cost. Furthermore the PADC is suitable for remoting since only the electro-optic modulator needs to be in the vicinity of the RF source. Other devices could be placed in a remote central unit allowing compact and light modules. The parallel nature of the back-end digitization portion of the system allows parallel processing; in fact, after the optical sampling process, a subsequent pulse switching is capable to split the pulsed samples into several parallel flows at lower sample rate, allowing to exploit precise narrow-BW electronic ADCs, Figure 1.7 [60]. Techniques used for the parallel PADC are TDM and WDM.

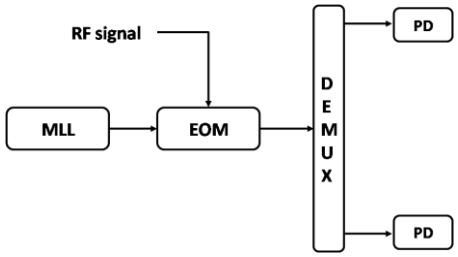

Figure 1.7 Basic scheme of interleaved PADC

Time interleaving multiplexing was implemented by using an active 1-to-N optical switch to distribute the interferometer output pulses to N parallel channels of detection electronics since a temporal window is created to route every Nth pulse to the same channel, thereby reducing the effective data rate into each electronic ADC by a factor of N [65][66].

In a WDM approach after the modulation optical pulses are separated into N distinct pulses each at a different wavelength. Discrete-wavelength pulse separation has been achieved using a wavelength-division multiplexer (WDM) along with fiber delay lines [61][62] and an arrayed-waveguide grating (AWG) with integrated feedback waveguides [63][64]. The demultiplexed pulse trains are demodulated by photodetectors and digitized in parallel using electronic ADCs. This passive demultiplexing is an advantage of the wavelength-division technique relative to the time-division technique, which requires an active demultiplexer containing accurately timed optical switches. However, this advantage is attained at the expense of a significantly more complex optical source that must generate a

periodically repeating mutliwavelength pulse train with very precise interpulse spacing. While wavelength-interleaving is most sensible to the time skew, time-interleaving suffers the inter-channels crosstalk due to the limited extinction ratio of the optical switching matrix.

Photonic Filters

Basically signal filtering is a useful tool to perform signal processing after the reception of RF signals. High performances microwave filters usually operates at low frequency (IF) after several down conversion stages. The concept of the MWP filters is based on the direct RF processing after the optical sampling architectures; in fact after amplitude or phase modulation (by an external MZM) the RF signal is directly processed in the optical domain by fibre and integrated optical delay lines, devices and circuits (Figure 1.8).

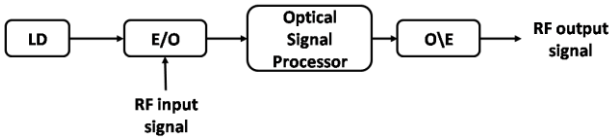

Figure 1.8 Basic scheme of photonic signal processing and filters

Microwave photonic filters are of great interest in many applications such as RoF or UWBoF systems for both channel-rejection or channel selection applications; radio-astronomy, where the signal transmission from several stations to a remote central site requires the removal of strong man-made interfering signals from the astronomy bands. In addiction MWP filters for RF signals can also be useful for light weight applications as for instance co-channel interference suppression in digital satellite communications. Another interesting application is the MTI filter for clutter and noise rejection (directly in the optical domain) in radar applications making the complete system more agile, flexible and tunable [67][68][69][70].

CHAPTER 2

2. PHOTONIC COMPONENTS FOR MICROWAVE APPLICATIONS

A brief discussion about the most important devices for a microwave photonic link is presented in this chapter. In particular the basic concept and equations will be given of the Mode Locked Laser, the Mach Zehnder Modulator (E\O conversion) and the photodiode (O\E conversion).

2.1. MODE LOCKED LASER

A Mode Locked Laser has the peculiarity of a well-defined and fixed phase relationship between all modes in the laser cavity. If the phases are locked in such way that there is a constructive interference between the modes at an instant and a destructive interference at other times, the output will appear as a pulse.

A mode locked laser time domain can be represented as a periodic function with equally spaced pulses. The period of the laser function is $T = \frac{2\pi}{\Delta\omega}$ where $\Delta\omega$ represents a laser characteristic repetition frequency. The pulse duration instead is a function of the number of modes (The pulse duration decreases as the number of modes increases) and it can be represented as $\tau = \frac{2\pi}{(2N+1)\Delta\omega} = \frac{1}{\Delta\upsilon}$ where $\Delta\upsilon$ is a full width of the generation band also called laser bandwidth BW. Therefore a time domain equation which represent the laser time domain function can be expressed as following where $i(t)$ is the laser intensity and N the number of modes [1][73].

$$i(t) = (A + a(t)) \frac{\sin^2\left[(2N+1)\frac{\Delta\omega}{2}(t + j(t))\right]}{\sin^2\left(\frac{\Delta\omega}{2}(t + j(t))\right)} \tag{2.1}$$

In the next figures (Figure 2.1, Figure 2.2) some examples of the time domain mode locked laser signal are reported for different values of propagating modes, time and amplitude jitter called respectively $j(t)$ and $a(t)$. The laser repetition frequency has been setting to 400 MHz which represent the final value of the selected commercial device. In the figures the time and amplitude jitter are represented as two Gaussian random process with mean value set to zero and standard deviation set to 10 fsec and one part over one million.

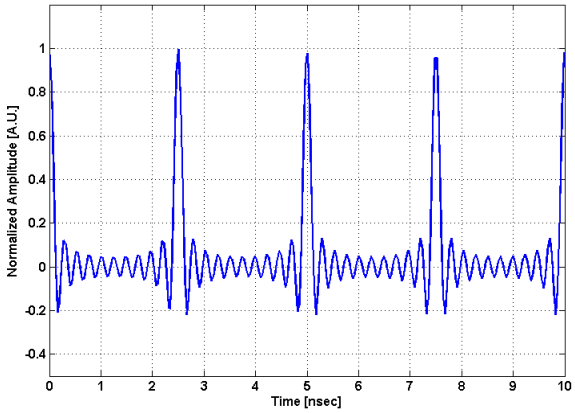

Figure 2.1 Time domain mode locked laser representation (N=10)

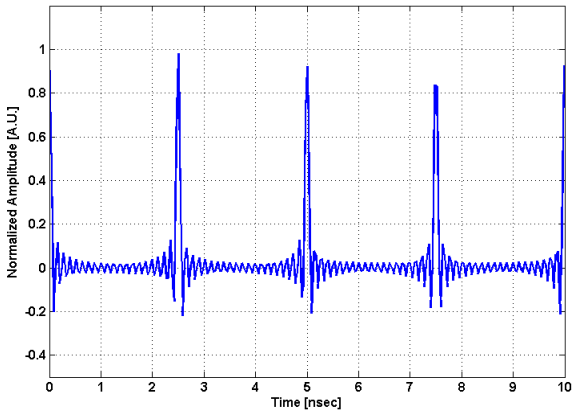

Figure 2.2 Time domain mode locked laser representation (N=20)

As previously said the subsidiary peaks are more attenuated when the number of modes increases and the pulse time duration decrease as results of the direct relation.

A simple structure of the obtained laser spectrum due to the Fast Fourier Transform of the time domain representation is shown in the Figure 2.3 where it is easily distinguishable the line spectrum modulated by the Gaussian laser envelope with bandwidth $\Delta\upsilon$. Each laser line is spaced by the pulse repetition frequency.

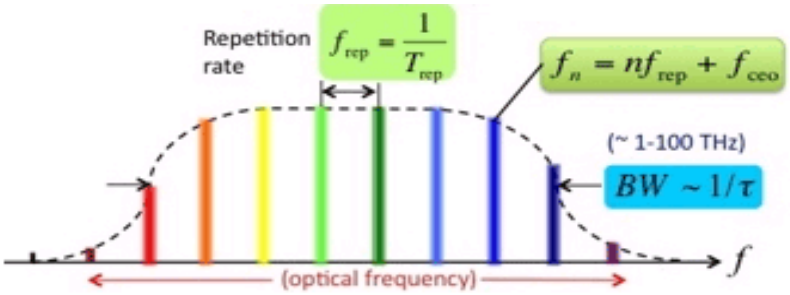

Figure 2.3 Mode Locked Laser Spectrum

The mathematical equation for the frequency domain representation can be written as:

$$MLL(f) = FFT\{i(t)\} = FFT\left\{\left(A + a(t)\right)\frac{\sin^2\left[(2N+1)\frac{\Delta\omega}{2}\left(t + j(t)\right)\right]}{\sin^2\left(\frac{\Delta\omega}{2}\left(t + j(t)\right)\right)}\right\} \tag{2.2}$$

and finally as a superposition of 2M+1 Gaussian shaped optical modes centred at the frequency $f_0 = c/\lambda_0$ and with a pulse repetition frequency f_{REP}. The amplitude, phase and time jitter input of the generated laser modes are indicated respectively as A_n, φ_n, and $j(t)$.

$$MLL(f) = \sum_{n=-M}^{M} \sqrt{A_n} e^{i\left[2\pi(f_0 + nf_{REP})t + 2\pi(f_0 + nf_{REP})j(t) + \varphi_n\right]} \tag{2.3}$$

2.2.MACH ZEHNDER MODULATOR

An electro-optic modulator (EOM) is a device which can be used for controlling the power, phase or polarization of a laser beam with an electrical control signal. The most important electro optic modulator is the Mach Zehnder Modulator which is device used to determine the relative phase shift between two collimated beams from a coherent light source [77]. The basic function of the MZM is further decrypted. Lightwave is split (a 3-dB splitting) into two arms when entering the modulator. Each arm of the LiNbO3 modulator employs an electro-optic phase modulator in order to manipulate the phase of the optical carrier if required. At the output of the MZIM, the light is combined from these arms at the output it can vary between a minimum level (corresponding to destructive interference) and a maximum (due to constructive interference) (Figure 2.4).The simplest Mach Zehnder design is one in which phase modulation is applied to only one of the arms, but it is also possible to have dual electrode designs and these have been used for optical single sideband generation (OSSB) in order to overcome the dispersion penalty which occurs in mm-wave fiber radio systems

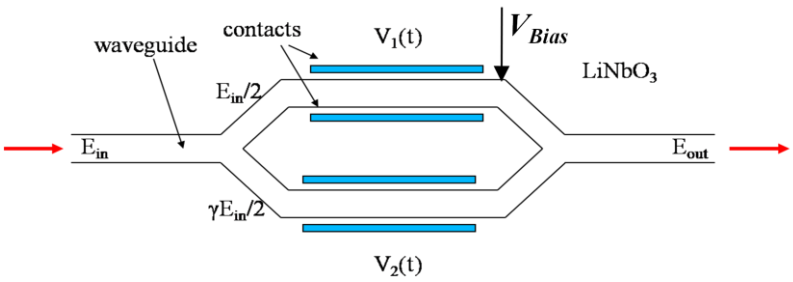

Figure 2.4 MZM diagram

The basic approach of the MZM is based on:

1. The actual optical power level (Po) depends not only on the modulator but also on the power supplied by the laser source (Pi); so the y-axis is a ratio of powers rather than being absolute power.
2. The x-axis is also a ratio, of the drive voltage V_m to V_π (defined as the voltage required for a phase shift of 180° between the two modulator arms).
3. The transfer characteristic is periodic, in principle allowing more choice in terms of choosing the bias point.

Considering T_{ff} the modulator's insertion loss when the MZM is biased in its minimum transmission point the transfer characteristic of the, modulator is given by:

$$\frac{P_0}{P_I} = \frac{T_{ff}}{2}\left[1+\cos\left(\frac{\pi V_m}{V_\pi}\right)\right] \tag{2.4}$$

And it can be seen in the Figure 2.5.

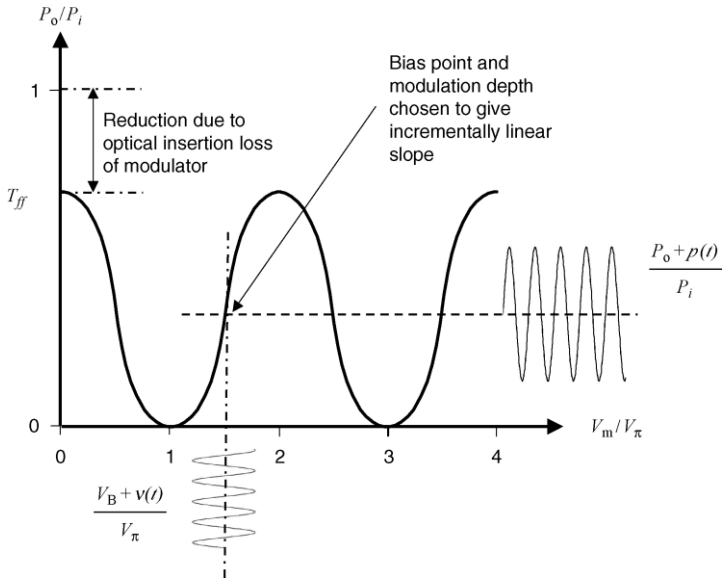

Figure 2.5 MZM transfer characteristic

Applying a bias voltage of $V_B=n\ V_\pi/2$ (where n is an integer) the drive voltage becomes $V_M=V_B+v_m(t)$ and, assuming a small signal modulation $v_m(t)$ (with $v_m(t) << V_M$), the equation can be rewritten as:

$$\frac{P_0}{P_I} = \frac{T_{ff}}{2}\left[1+\cos\left(\frac{\pi\left(V_B+v_m(t)\right)}{V_\pi}\right)\right] \approx \frac{T_{ff}}{2}\left(1\pm\frac{\pi v_m(t)}{V_\pi}\right) \tag{2.5}$$

Therefore the optical output power of the MZM is given by:

$$P_O \approx \frac{P_I T_{ff}}{2}\left(1 \pm \frac{\pi v_m(t)}{V_\pi}\right) \tag{2.6}$$

The electro\optical conversion efficiency (the slope efficiency) is obtained as:

$$\eta_{MOD} = \frac{dP_O}{dv_m} = \frac{\pi P_I T_{ff}}{2V_\pi} \tag{2.7}$$

Considering the case where $v_m(t)$ is comparable with V_M the effective output power and the conversion efficiency can be written as ($v_m(t)/V_\pi$ represent the modulation depth m_d):

$$P_O \approx \frac{P_I T_{ff}}{2}\left(1 \pm \cos\left(\frac{\pi v_m(t)}{V_\pi}\right)\right) \tag{2.8}$$

$$\eta_{MOD} = \frac{dP_O}{dv_m} = \frac{\pi P_I T_{ff}}{2V_\pi}\sin\left(\frac{\pi v_m(t)}{V_\pi}\right) \tag{2.9}$$

In Figure 2.6 an example of the optical output power of the MZM is presented in function of the modulation depth as reported in equation 2.7. Other simulation parameters are: V_π=3.5V and the modulator's insertion loss equal to 1dB.

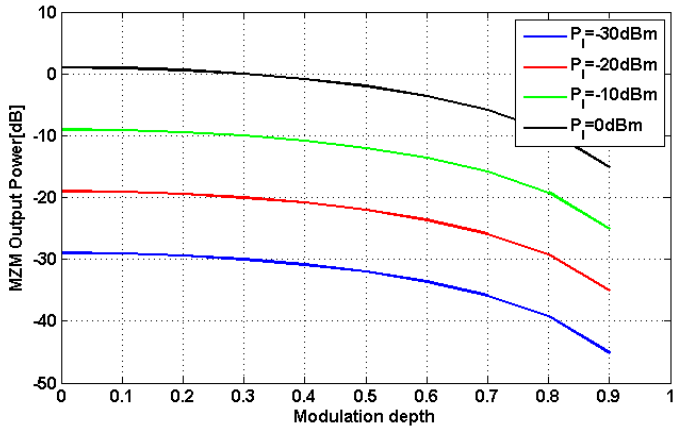

Figure 2.6 MZM Outupu power as function of the modulator modulation depth

For a laser optical input power of -10dB the time domain representation of the MZM output is reported in Figure 2.7 for four different modulation depths.

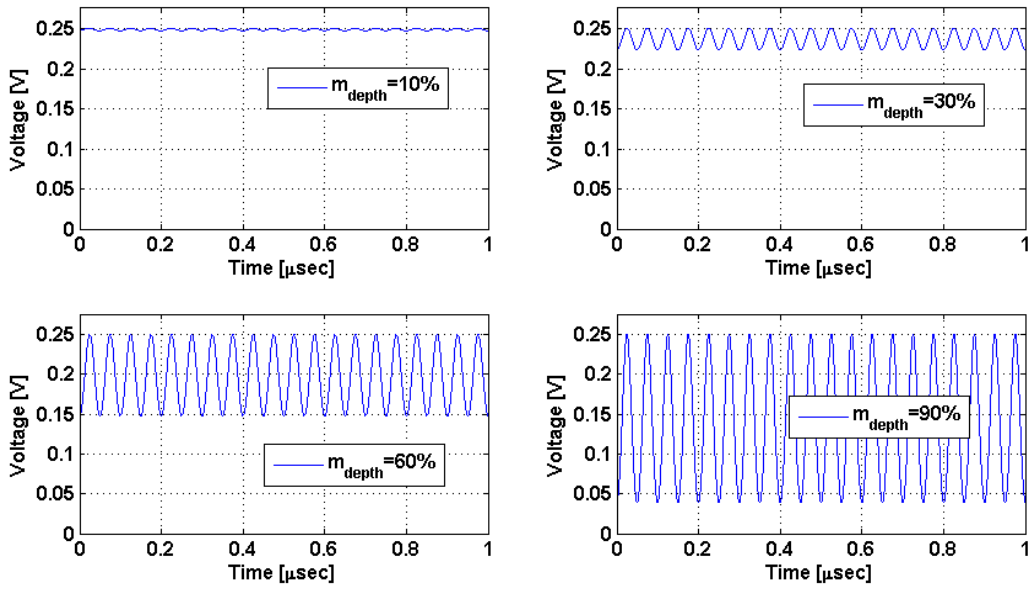

Figure 2.7 MZM output in function of the modulation depth

So main that in order to increase the efficiency of the external modulation is possible to increase the input optical power in addition to a low V_π MZM with minimum insertion losses.

A Mach Zehnder modulator will in general produce multiple optical sidebands when modulated by a microwave sinusoid, leading to terms in $\omega_0 \pm n\omega_0$. This is a consequence of the nonlinearity of the E/O conversion process. However, through appropriate bias and modulation conditions, it is possible to suppress higher order sidebands, leaving a carrier plus an upper and lower sideband, namely ω_0 and $\omega_0 \pm n\omega_0$ [75][76][78][73].

2.3.PHOTODETECTOR

In general an O/E device (commonly called photodetector) converts incoming modulated light into corresponding variations of current. The most important requiremetns for a photodiode are represented by the quantum efficiency, the responsivity and the device's bandwidth.

The quantum efficiency η is defined as the ratio between the number of the electrons $\eta_{electron}$ generated by the photoelectric effect in the absorption region and the number of photons incident on the detector surface $\eta_{photons}$.

$$\eta = \frac{\eta_{electron}}{\eta_{photons}} \tag{2.10}$$

This value for a PIN diode is an integer number <1 and expresses the efficiency of the conversion process of the optical-electrical photodetector.

The photodetector responsivity is strictly related to the quantum efficiency and represents the value of the generated photocurrent per unit of optical power incident on the detector it is commonly represented in A\W.

$$\Re = \frac{I}{P_0} = \frac{\eta_{electron}\, q/T}{\eta_{photon}\, E_{photon}/T} = \eta \frac{q}{hf} = \eta\lambda \frac{q}{hc} \tag{2.11}$$

In Figure 2.8 is possible to see the wavelength effect of the photodetector responsivity for some of the most common materials.

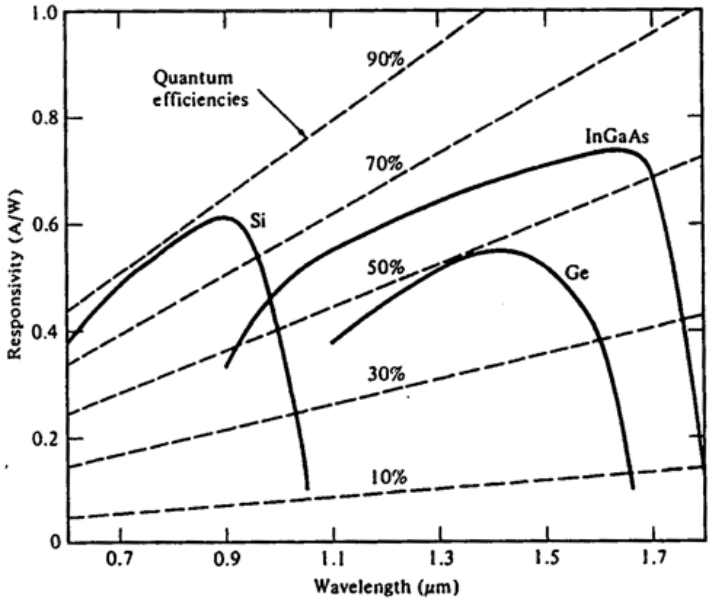

Figure 2.8 Photodetector responsivity

The time response and the bandwidth of a photodetector are mainly related by two factors: the transit time of the electrons through the device and the characteristic electrical time constant of the component [74][75].

The photodetection process imposes a lower limit to the maximum obtainable sensitivity and it is the cause of the noisy phenomenon intrinsically related to the quantization energy associated with the incident radiation (shot noise). The shot noise can be represented as a random fluctuation in time that goes to overlap the average current I_{PD} detected by the opto-electronic device. The shot noise spectral distribution is uniform and it is proportional to the level of the current $I_{PD.}$

$$\left\langle i_{shot}^2(t)\right\rangle = 2qI_{PD}B \tag{2.12}$$

Where B represents the overall bandwidth of the photodiode.

Is it possible to see that the shot noise increases when the current I_{PD} increase. Being $I_{PD} = \Re\left\langle P_{OPT}\right\rangle$ it grows within the average value of the optical input power to the detector.

On the other hand the optical detectors are characterized by an intrinsic noise source that can not be eliminated even in the absence of the optical input signal and it is called dark noise. Therefore when the inoput signal presents a level below its dark noise, it will be completely hidden and no detectable. This kind of noise could be represented as:

$$\left\langle i_{dark}^2(t)\right\rangle = 2qI_{D}B \tag{2.13}$$

Where I_D represent the dark current of the photodiode [79].

2.4. GAIN, NOISE FIGURE AND DYNAMIC RANGE OF AN EXTERNALLY MODULATED PHOTONIC LINK

In this paragraph a brief discussion about the photonic link gain and effective noise figure is presented.

The effective gain of a two port device is given by the ratio between the available power at the device's output and the input power (equation 2.14).

$$G = 10\log_{10}\left(\frac{P_{out}}{P_{in}}\right) \tag{2.14}$$

Considering a microwave photonic link the expression is given by:

$$G_{dB} = \left(\frac{\eta_{MOD}\Re}{A_{opt}}\right)^2 \frac{R_{load}}{R_{in\_MZM}} \tag{2.15}$$

Where η_{MOD} is the conversion efficiency, $\Re$ is the photodiode responsivity, A_{opt} is the attenuation of the optical path and R_{load} and R_{in_MZM} represent the load impedance of the link and load impedance of the modulator. By referring to a perfect matching device with an external modulation we can assume $R_{load}=R_{in\_MZM}$ and the equation 2.15 becomes:

$$G = \left(\frac{\frac{T_{ff}P_i\pi}{2V_\pi}\Re\sin(\pi m_d)}{A_{opt}}\right)^2 \frac{R_{load}}{R_{MZMin}} \tag{2.16}$$

Therefore the photonic link effective gain is directly related to the laser input power and by increasing the optical power the gain increases up to a maximum value corresponding to the maximum accepted power by the guide and the photodiode.

In Figure 2.9 a simulated effective gain of a photonic microwave link is shown. Simulation parameters are $T_{ff}=0.1$, $m_d=0.8$, $\Re=0.9$, $A_{opt}=0.1$.

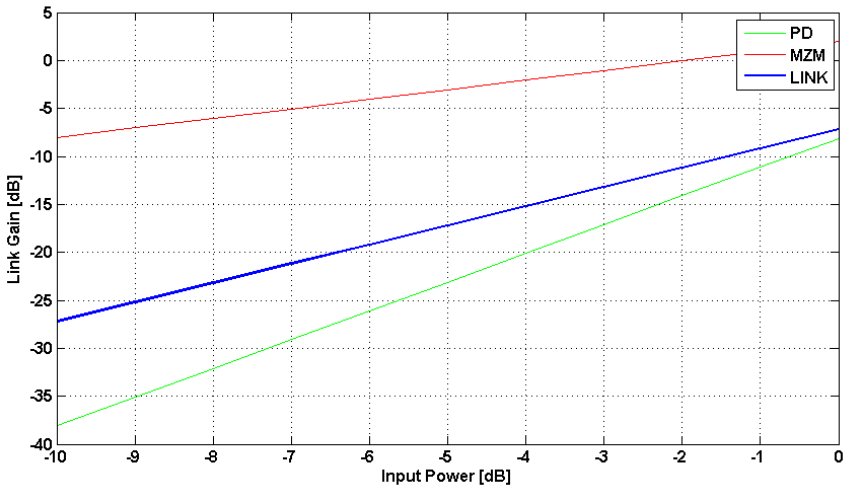

Figure 2.9 Simulated photonic link gain vs input power.

The photonic link effective noise figure represents the signal to noise degradation when a signal is processed by a generic device and is defined as:

$$NF = 10\log_{10}\left(\frac{S_{in}/N_{in}}{S_{out}/N_{out}}\right) = \frac{1}{S_{out}/S_{in}}\frac{N_{out}}{N_{in}} = \frac{1}{G}\frac{N_{out}}{N_{in}} \tag{2.17}$$

Where S_{in} and S_{out} represent the values of the signal input and output power respectively while N_{in} and N_{out} represent respectively the values of the noise input and output power. By taking into account the photonic link the most important noise contributions are due to the laser RIN and shot noise of the photodetector.

Considering a loss free system the noise figure of a microwave photonic link can be expressed as:

$$NF = 10\log_{10}\left(2 + \frac{1}{G} + \frac{\left(I_D^2 RIN + 2qI_D\right)R_{PDout}}{4kTG}\right) \tag{2.18}$$

Where I_D is given by:

$$I_D = \frac{\Re T_{ff} P_i}{2}\left[1 + \cos\left(\pi m_d\right)\right] \tag{2.19}$$

For an external modulation the NF decreases when the optical input power increase because the optical gain becomes greater than the contribution of the shot noise [79][80][81][82].

Figure 2.10 shown the noise figure in function of the optical input power and it is possible to see that the noise figure decreases for high input power approaching the theoretical limit 3dB imposed by the equation 2.19. Figure 2.11, and Figure 2.12 show the photonic link gain and noise figure in function of the modulation depth.

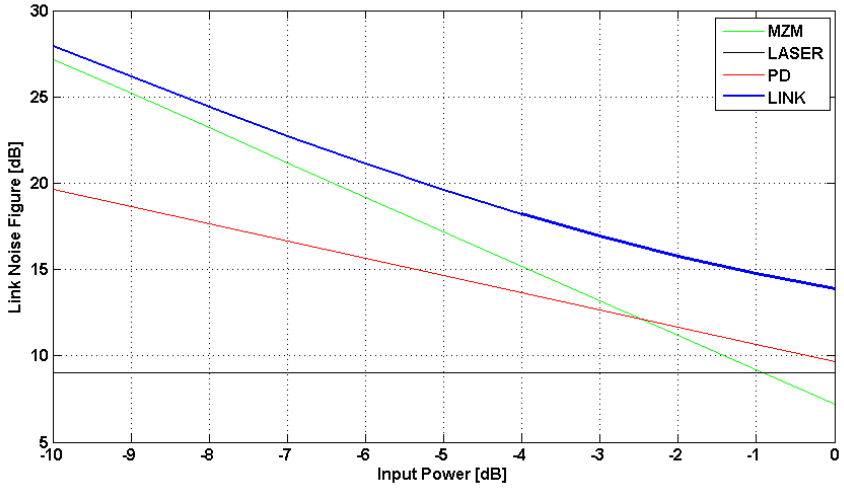

Figure 2.10 Simulated photonic link noise figure vs input power

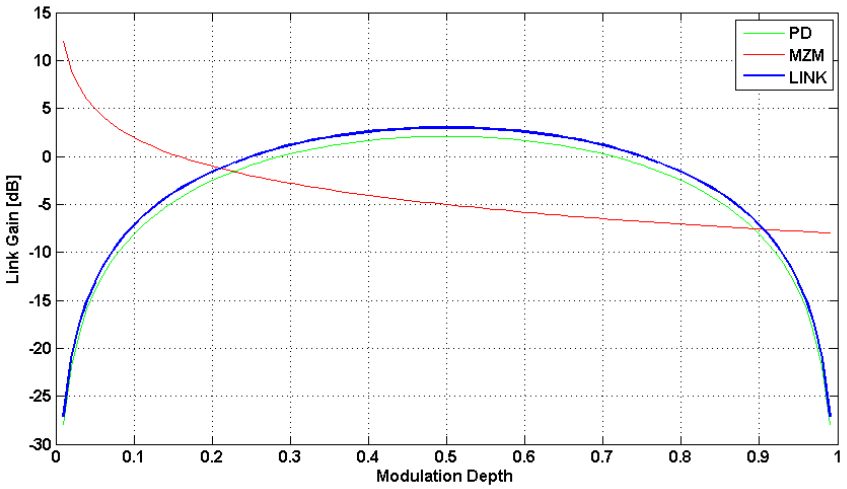

Figure 2.11 Simulated photonic link gain vs modulation depth.

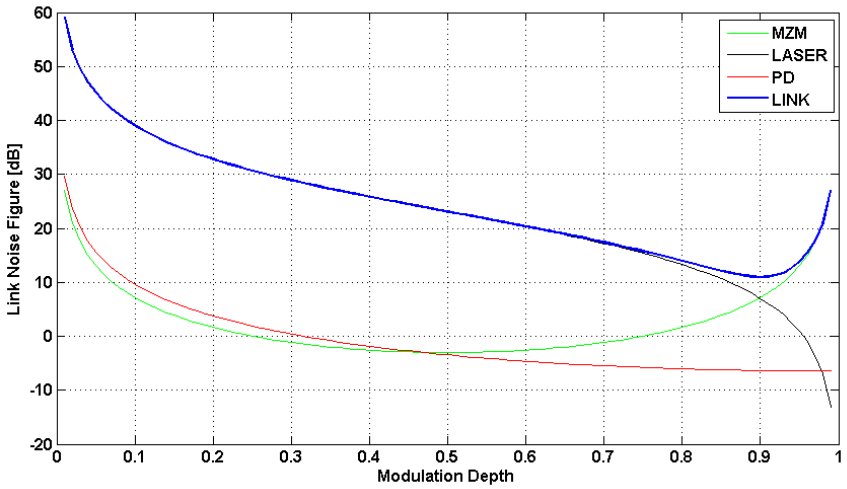

Figure 2.12 Simulated photonic link noise figure vs modulation depth

The carrier to noise ratio (2.20) represents the main parameters for a photonic link. In the following Figure 2.13 and Figure 2.14 show the CNR as function of the optical input power and modulation depth.

$$CNR = \frac{\left(m\Re P_{PDin}\right)^2 \backslash 2}{\left(\sigma_s^2 + \sigma_{th}^2 + \sigma_{RIN}^2\right)} \tag{2.20}$$

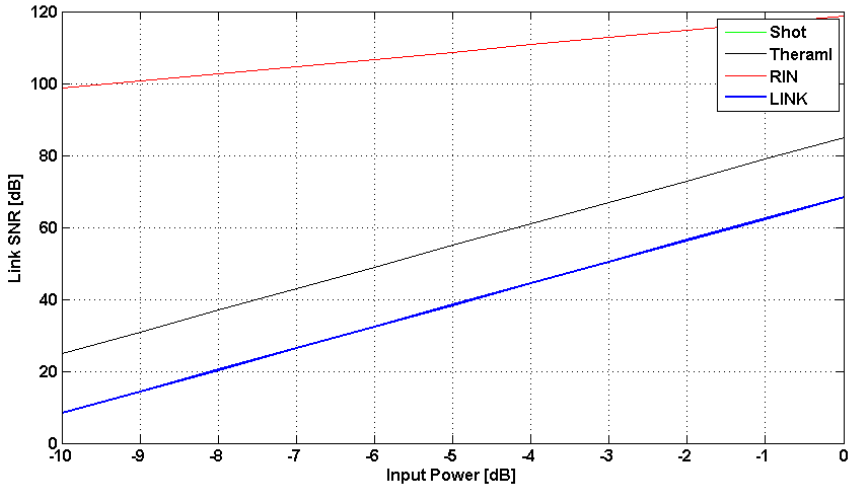

Figure 2.13 Simulated photonic link CNR vs input power

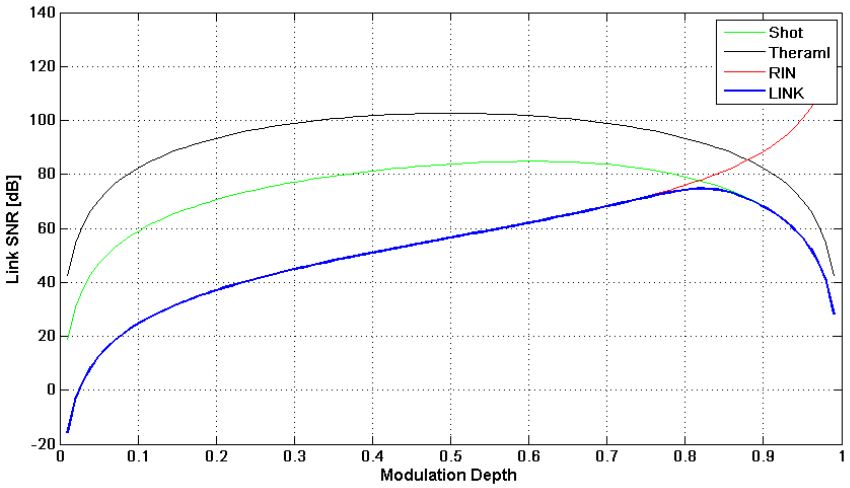

Figure 2.14 Simulated photonic link CNR vs modulation depth

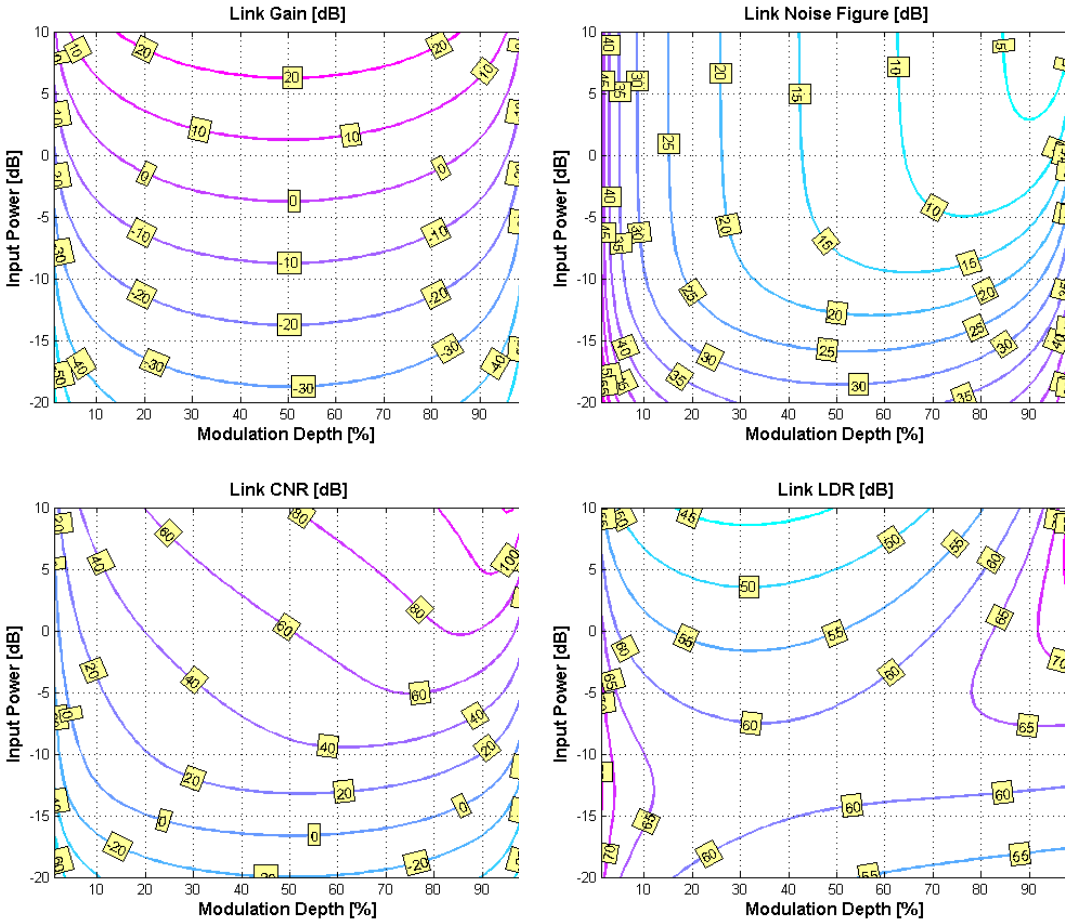

Figure 2.15 Simulated photonic link parameters (RIN=-165dB/Hz, B=100GHz, V_π=3V, *R*=0.9)

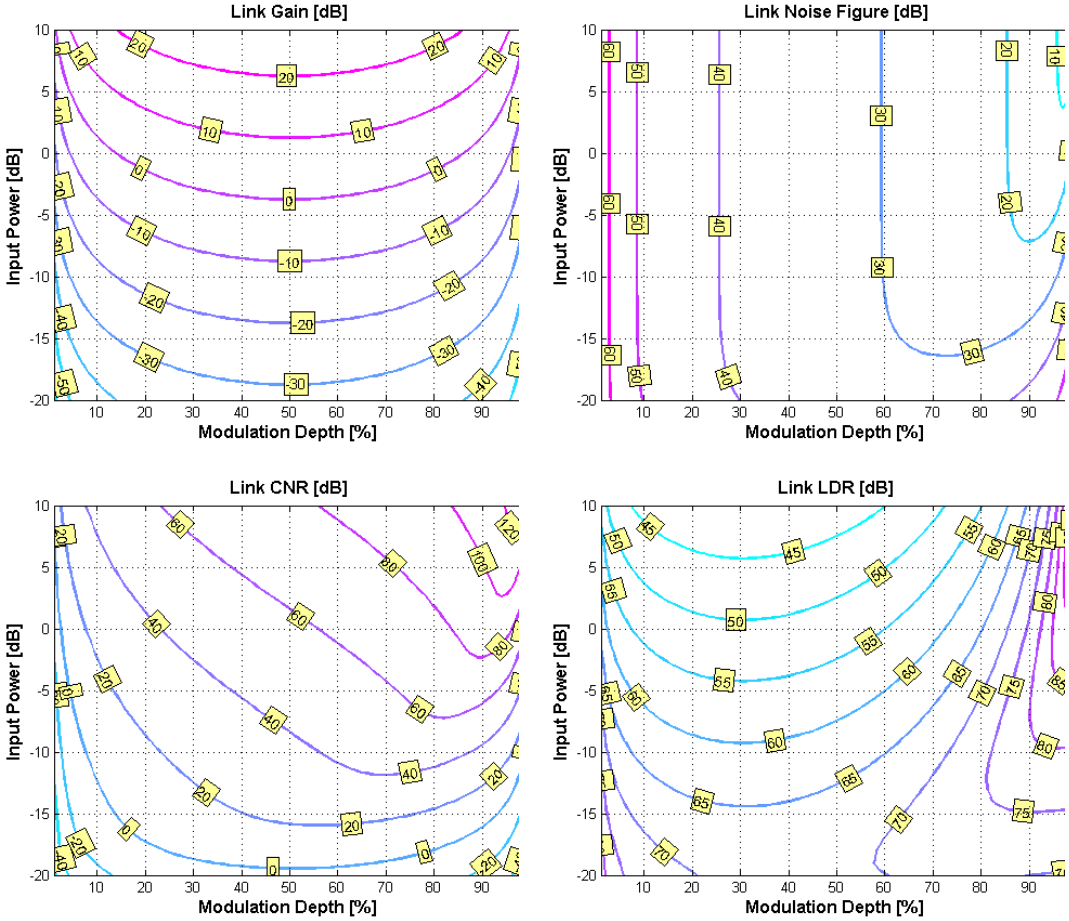

Figure 2.16 Simulated photonic link parameters (RIN=-145dB/Hz, B=2GHz, V_π=3V, *R*=0.9)

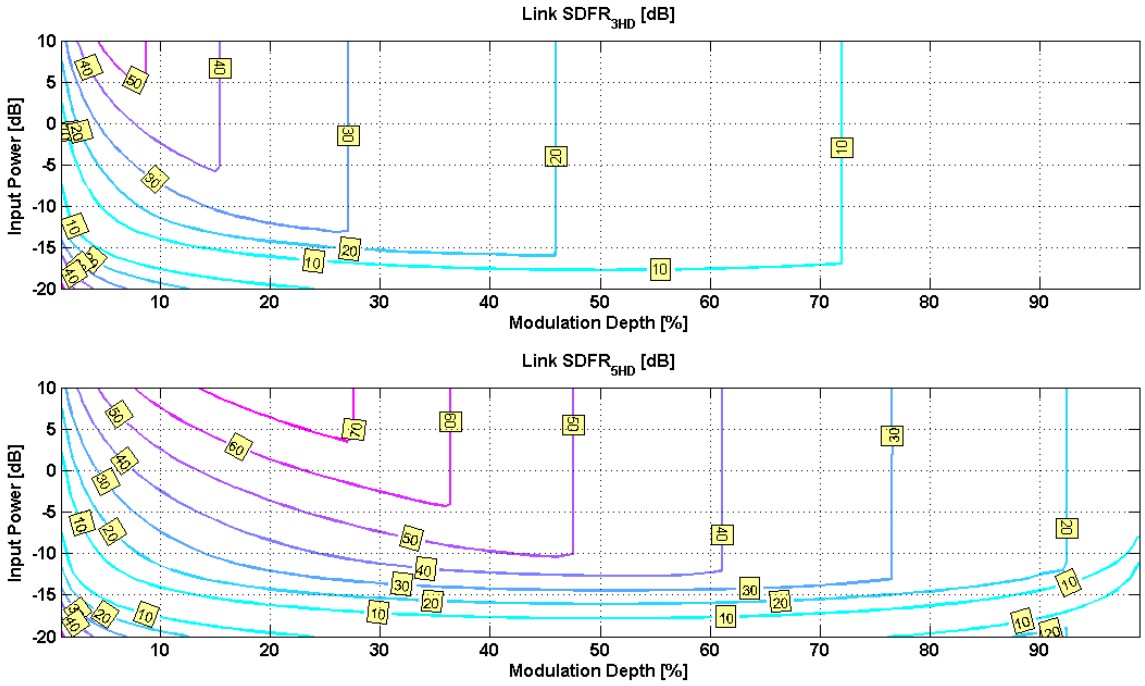

Figure 2.17 Simulated photonic link SFDR (RIN=-165dB/Hz, B=2GHz, V_π=3V, *R*=0.9)

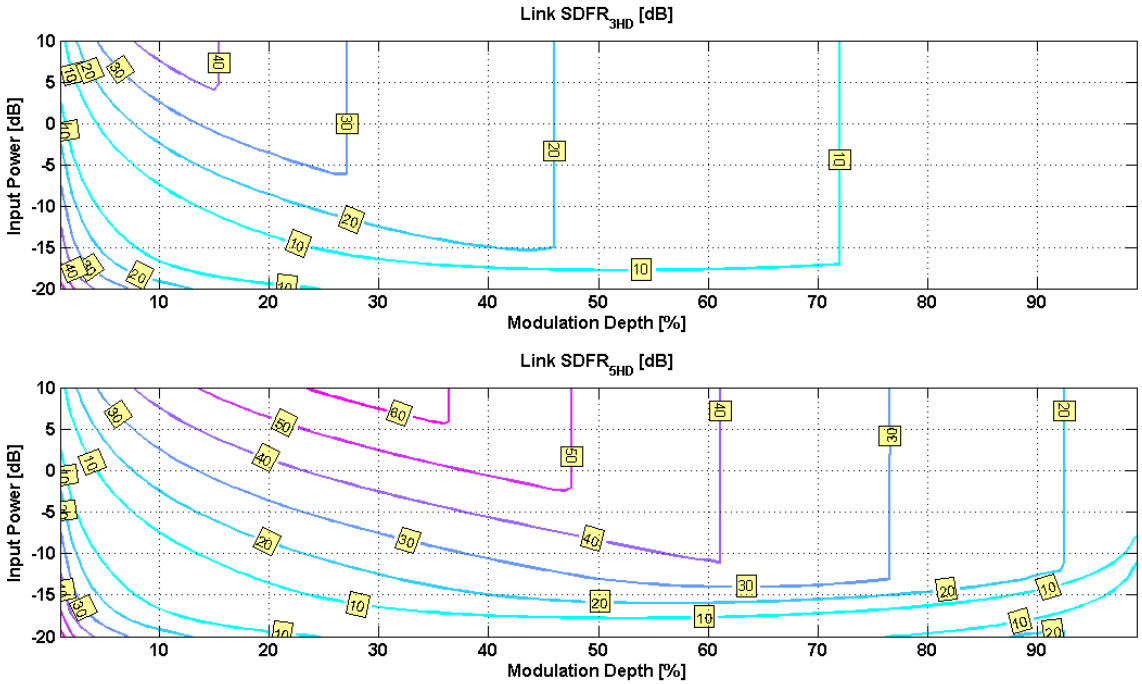

Figure 2.18 Simulated photonic link SFDR (RIN=-145dB/Hz, B=2GHz, V_π=3V, *R*=0.9)

CHAPTER 3

3. PHOTONIC MICROWAVE SIGNAL GENERATION

Coherent radar systems are able to detect moving objects by analyzing the Doppler shift in the carrier frequency of the reflected echo pulses. The increasing need for radars with high sensitivity and small antennas are demanding carrier frequencies with low phase noise and high frequency. Moreover, radar systems are seeking increased resolution as well as the carrier frequencies to detect and recognize small objects. To this aim, rather than reducing the duration of the radar pulses, so-called pulse compression techniques have been implemented which broaden the signal bandwidth by modulating the phase of the radar pulse carrier, thus avoiding the expensive transmission of dangerous high-power RF peaks [1][30]. The increasing resolution represent a most important requirement in security applications as human imaging radar for criminal or terrorist action prevention, detection of hidden objects, or in automotive applications [83].

Moreover the transmission of two or more radar signals at different carrier frequency is often implemented to increase the detection probability and to reduce the risk of false detections in adverse conditions, by reducing the target signature fluctuations and by averaging and smoothing the complex echo signals. This technique, called frequency agility (or diversity), also implies additional benefits. In fact, it allows the elimination of the Doppler blind speed and of the Doppler dilemma. In weather radars it can be used to build up a composite image of clouds and rainfalls. Frequency agility is also useful for jamming immunity, making more difficult to disturb the radar and, if the system rapidly switches between several frequencies, can render the jamming ineffective. Finally, radar systems with multiple carriers are becoming of interest in dual-band multifunctional radars, where surveillance and detection & tracking are implemented simultaneously using a single radar apparatus [84].

The requirement of phase stability at high carrier frequency is a challenge for the electronic RF signal generation since the frequency multiplication processes that are usually exploited, reduce the phase stability of the original RF oscillators. On

the other hand, frequency diversity radars are commonly realized by using two or more radar transmitters, implying a significant increase in cost and power consumption.

In the last years the use of photonics has been suggested as an effective way for generating low phase-noise RF carriers even at high frequency. Among other techniques, the heterodyning of modes from a mode locking laser (MLL) has proven to generate low-phase noise RF carriers up to the EHF band (30-300GHz) [44][85]. On the other hand, few works have been proposed so far for optically generating software-defined phase-modulated RF signals [86][87].

In the paragraph 3.1 the concept of the multifrequency photonic generation of microwave signals is presented. In addition two innovative techniques for optically generating phase-modulated RF pulses with flexible carrier frequency, and with a phase stability suitable for coherent radar systems is presented in 3.2 and 3.3. Both the proposed schemes exploit a commercial device: a standard MZM in the first scheme, and an optical in-phase/quadrature (I/Q) modulator, also referred to as a dual-parallel Mach Zehnder modulator, in the second scheme. Both the implemented schemes are capable of generating arbitrary phase modulated RF pulses with high stability, even at very high carrier frequency, with potentials for wideband modulation.

3.1. PHOTONIC RADIO FREQUENCY SIGNAL GENERATION

3.1.1. Principle of operation and experiment set up

The architecture of the reconfigurable full digital radar transmitter is shown in Figure 3.1. The generation of the RF carrier frequency is realized by beating two laser modes coming from a fiber mode locked laser into a photodiode. The MLL is a fiber laser with excellent stability, thanks to the auto-regenerative feedback. It is able to produce very stable narrow optical pulses with repetition rate in the range from 1 to 40 GHz. The optical spectrum is composed of a number of modes, whose spacing is equal to the pulse repetition rate. All the laser modes are phase locked with each other, thanks to the mode locking condition and the regenerative feedback that keeps the modes well locked [88][44]. The selection of the two beating modes is realized by splitting the optical signal emitted by the MLL in two arms by an optical splitter with a 50% splitting ratio. Each replica of the signal is filtered by an optical filter in order to select only one mode from the spectrum. In order to achieve a stable RF signal after the photodiode, the two arms of the scheme should be mechanically stable. The RF up conversion system can be realized by means of an electro-optical modulator (EOM), such as a MZM biased along its quadrature point [89], into one of the two arms.

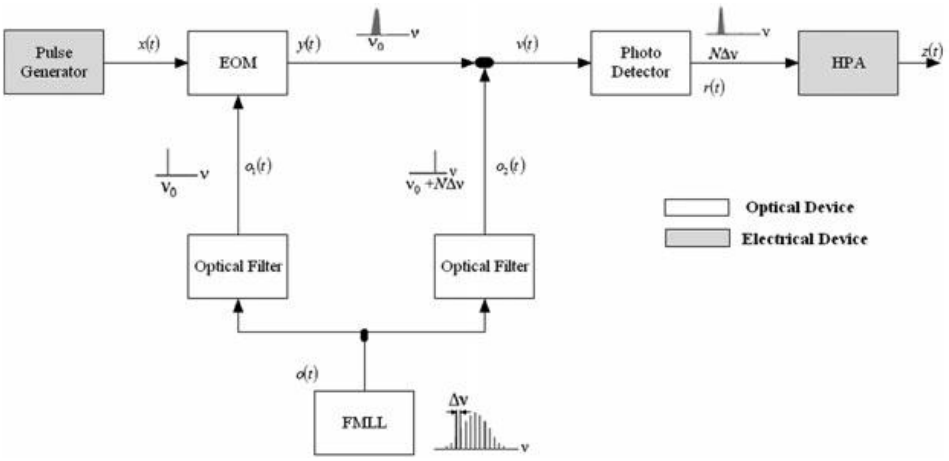

Figure 3.1 Reconfigurable photonic microwave system

The MZM is driven by a baseband signal generation block which addresses the digital synthesis of arbitrary waveforms (such as pulse trains, coded waveforms, frequency modulated waveforms such as chirp) with an adaptive bandwidth optimized according to the targets of interest and the environment. For example some of the key features of the baseband signal generation are the frequency,

phase and amplitude sweeping capability, the number of bits of the digital to analog convert, and so on. The two modes, the modulated and the unmodulated ones, are then combined together in a coupler and then sent in a photodiode which realizes the heterodyning, generating the final microwave signal. Finally, the RF amplification stage or a single high power amplifier (HPA) provides the necessary power for transmission [90].

Under this assumption, the concept of reconfigurable transmitter becomes feasible. As a matter of fact, it possible to tune the optical filters changing the operative wavelength by means of an electrical control. We are therefore able to select different laser modes with specified tuning frequency (i.e. a multiple of the laser repetition rate) according to the optical filter bandwidth. Therefore, exploiting a single photodetector, we can easily generate a modulated radar signal at different RF carriers up to W band and achieve frequency flexibility and reconfigurability. Obviously, in order to make the proposed architecture operatively flexible, we should make use of a wideband direct digital synthesizer able to realize different type of radar signals (such as unmodulated pulses, chirp, and Barker codes). Moreover, an amplification stage composed of RF filters and power amplifiers capable of dealing with wide bandwidth are necessary.

Referring to Figure 3.1, a mathematical expression of the transmitted signal is detailed in the following equations. Under the assumption of $\omega_0 = c/\upsilon_0$, where c is the speed of light, υ_0 is the central wavelength, and $\Delta\omega = 2\pi\Delta f$. The MML laser signal o(t) can be represented by a superposition of 2N + 1 sinusoidal functions which represent the different modes propagating in the cavity:

$$o(t) = \sum_{q=-N}^{N} e^{i\left[(\omega_0 + q\Delta\omega)t + \varphi_q\right]} \tag{3.1.1}$$

According to the mode locked condition, each mode is locked with each other because they have the same phase relation. Therefore equation (3.1.1) can be rewritten changing the term φ_q in φ.

$$o(t) = \sum_{q=-N}^{N} e^{i\left[(\omega_0 + q\Delta\omega)t + \varphi\right]} \tag{3.1.2}$$

The two selected adjacent laser modes with a detuning equally to the laser repetition rates $\Delta\omega$ are:

$$o_1(t) = o(t) \otimes h_{OF1}(t) = Ae^{i[\omega_0 t+\varphi]} \tag{3.1.3}$$

$$o_2(t) = o(t) \otimes h_{OF2}(t) = Ae^{i[(\omega_0+\Delta\omega)t+\varphi]} \tag{3.1.4}$$

The MZM output signal y(t) represents the modulated radar signal obtained through the electro-ptical modulator and can be written as:

$$y(t) = A\left\{0.5 + 0.5\cos\left[\frac{\pi(x(t)+V_{bias})}{V_\pi}\right]\right\}e^{i[\omega_0 t+\varphi]} \tag{3.1.5}$$

x(t) is the baseband radar signal, Vπ is a characteristic parameter of the Mach Zehnder modulator, and V_{bias} is the selected voltage useful to drive the modulator in a quadrature point. The signal v(t), before the photodetection process, can be written as:

$$v(t) = y(t) + o_2(t) = A\left\{0.5 + 0.5\cos\left[\frac{\pi(x(t)+V_{bias})}{V_\pi}\right]\right\}e^{i[\omega_0 t+\varphi]} + Ae^{i[(\omega_0+\Delta\omega)t+\varphi]} \tag{3.1.6}$$

The photodiode realizes the beating between the modulated and the unmodulated signal and the output is given by

$$r(t) = v(t)^2 = (y(t) + o_2(t))^2 \tag{3.1.6}$$

Some higher frequency terms, on the order of hundreds of THz, such as the ones at $2\omega_0$ and $2\omega_0+2\omega_0+2\Delta\omega$ have been filtered out by the photodetector with an analog bandwidth of the order of GHz.

Therefore the photodetector output becomes:

$$r(t) = A^2\left\{0.5 + 0.5\cos\left[\frac{\pi(x(t)+V_{bias})}{V_\pi}\right]\right\}e^{i[\Delta\omega t+\varphi]} \tag{3.1.7}$$

As previously stated, the proposed scheme offers the capability of reconfigurable transmission. As a matter of fact, by tuning the filters, it is possible to select laser modes at different detuning frequencies at any multiple of the laser repetition rate (i.e. the mode at frequency $2\pi\omega_0$ and the mode at frequency $2\pi\omega_0+2\pi N\Delta\omega$, where N represents the mode spacing). Moreover, the use of a digital baseband signal generator allows matching the RF signal modulation to the target and the environment.

3.1.2. Results on single carrier experiment

The architecture set up of the single-carrier experiment (Figure 3.2) consists of a MLL provided by PhoTrix operating at 10 GHz and able to emit 4 ps very stable pulses centered at 1550 nm. An erbium-doped fiber amplifier is used before the filtering process to guarantee sufficient optical power at the photodiode and a band pass filter with a 3 dB bandwidth of 0.15 nm and steep edges has been used to select two adjacent laser lines.

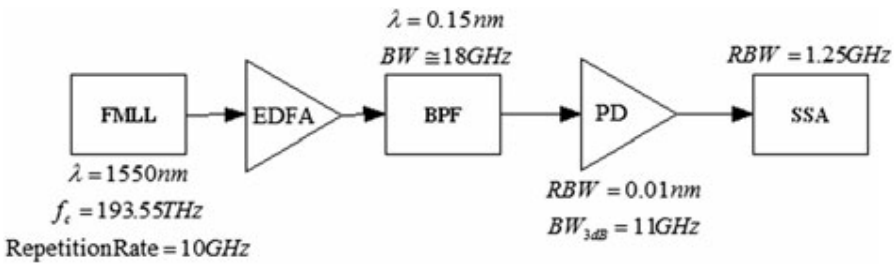

Figure 3.2 Single carrier experiment set up

Figure 3.3 shows the filtered optical spectrum taken by an optical spectrum analyzer with a resolution bandwidth of 0.01 nm (corresponding to 1.25 GHz), compared with the original spectrum of the FMLL. The undesired modes are suppressed more than 20 dB. The two selected modes are then injected in an amplified photo-detector with a 3 dB bandwidth of 11 GHz. Since the photodiode realizes a quadratic function of its optical input, the two inserted laser modes beat together generating a RF signal at a frequency that is equal to their detuning frequency (i.e. 10 GHz).

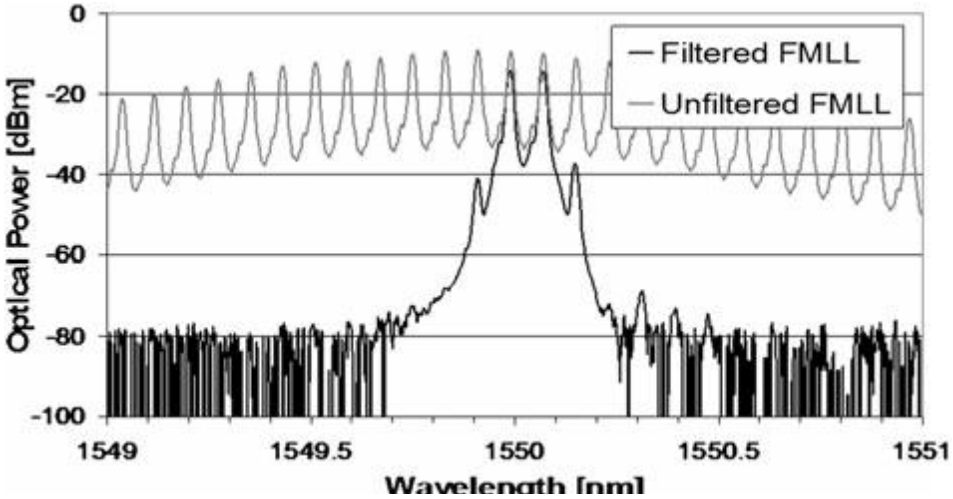

Figure 3.3 Optical spectrum of the FMLL and the two selected adjacent modes.

The microwave signal thus generated is analyzed by means of a signal source analyzer (Agilent E5052A). The obtained results are shown in Figure 3.4, where the phase noise of the beating signal is compared with other RF sources, namely aVCO at 10 GHz (Narda FFCM), a state of the art synthesizer (Agilent E8257D), and the Anritsu RF generator. The performances of the heterodyning of two distributed-feedback (DFB) lasers with a detuning frequency of 10 GHz (EXFO IQS-2400 modules) have been presented in [88].

The comparison is realized for a frequency offset in the range 100–40 MHz. These range limits are due to the intrinsic limitation of the measurement instruments.

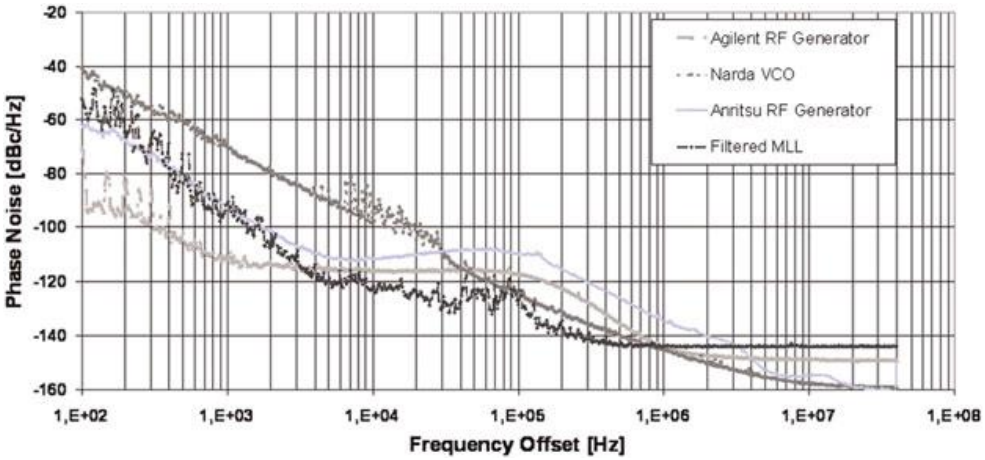

Figure 3.4 Comparison of phase noise levels for different RF sources at 10 GHz.

It should be noted that the proposed architecture (black line) and the state of the art RF synthesizer provided by Agilent (light gray line), show comparable behaviors,

whereas the other RF generation methods present the worst performance, with phase noise levels tens of dB higher along most of the analyzed frequency range. The proposed RF generation technique works better than the synthesizer in a wide range of frequency, from about 5 kHz up to 1 MHz. For offset frequencies above 1 MHz, even though the synthesizer shows less phase noise, both the RF sources perform well. On the other hand, for offset frequencies lower than 5 kHz, the state-of-the-art synthesizer shows extremely low phase noise, whereas our proposed photonic RF generation becomes more instable, although its behavior is still better than other RF sources.

Integrating the phase noise curve reported in Figure 3.4 it is possible to calculate the timing jitter of the RF signal. The numerical equation used to calculate the signal time jitter is shown below [91]:

$$jitter_{RMS} = \frac{1}{2\pi f_0}\sqrt{2\sum_{k=1}^{K-1} 10^{\upsilon_k/10} f_k^{-s_k/10}\left(\frac{s_k}{10}+1\right)^{-1}\left[f_{k+1}^{\left(-s_k/10-1\right)} - f_k^{\left(-s_k/10-1\right)}\right]} \qquad (3.1.8)$$

The terms f_0 and f_k in equation (3.1.8) represent, respectively, the carrier frequency (equal to 10 GHz) and the frequency interval between two adjacent values of frequency offset (where the frequency offset axis has been divided into K-1 values used for the numerical integration).

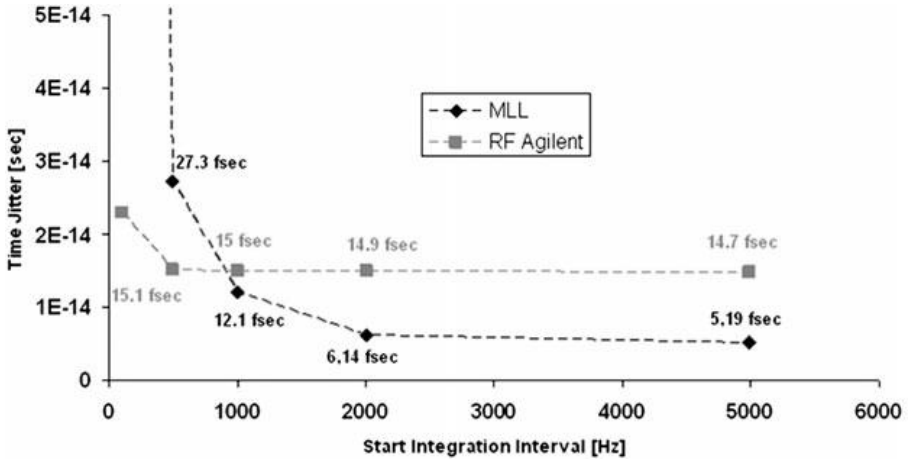

Figure 3.5 Time jitter values for filtered MLL and Agilent E8257D synthesizer at 10 GHz.

Instead the terms υ_k and s_k represent, respectively, the phase noise value at a frequency offset f_k and the relative slope in the same point (the term Φ represent the phase noise level expressed in dBc/Hz) [92]:

$$\upsilon_k = \Phi(f_k) \tag{3.1.9}$$

$$s_k = \frac{\Phi(f_{k+1}) - \Phi(f_k)}{\log[\Phi(f_{k+1})] - \log[\Phi(f_k)]} \tag{3.1.10}$$

The integration interval should be chosen accordingly with the observation time related to the radar application (i.e. the phase coherence must be maintained for the whole observation time necessary to obtain a coherent detection of the target) and due to the limits of the measurement device. We performed the calculation for different frequency intervals starting for example from 100 Hz up to 40 MHz, from 1 kHz up to 40 MHz and so on. The results comparing the proposed RF generation method and the Agilent synthesizer are reported in Figure 3.5.

When the phase noise is integrated starting from 1 kHz up to 40 MHz, the obtained jitter for the filtered MLL decreases with respect to the time jitter of the Agilent RF synthesizer (i.e. between 1 kHz and 40 MHz, the obtained jitter is 12.1 fs for the filtered MLL and 15 fs for the Agilent synthesizer). On the other hand, when the integration time starts from 500 Hz the timing jitter from the photonic architecture is larger than the microwave state of the art source (27.3 fs for the filtered MLL and 15.1 fs for the Agilent synthesizer).

The electrical spectra have been calculated, with a resolution bandwidth of 100 Hz, for the proposed technique and the RF Agilent synthesizer. The results have been presented in a previous work showing the same value of signal to noise floor ratio (above 80 dB) for both the signals and presenting very narrow line widths [93].

3.1.3. Results on multi carrier experiment

For the multicarrier RF generation experiment, we exploit integrated optics technology and pecially designed dua- wavelength fiber Bragg gratings (DFBG) which allow to select two different laser modes from a FMLL. Under this assumption we do not separate the physical paths of the two modes avoiding any additional reciprocal phase fluctuations due to mechanical vibrations of the structure. The DFBGs are designed in order to reflect two narrow bands with a detuning frequency, respectively, of 20 and 30 GHz and so on, up to 100 GHz [94].

Therefore, the two selected modes are then injected into an amplified photo-detector with a given 3 dB bandwidth. Figure 3.6 shows the before mentioned

optical spectrum measured by an optical spectrum analyzer with a resolution bandwidth of 0.01 nm (corresponding to 1.25 GHz), compared with the original spectrum of the FMLL. The undesired modes are suppressed more than 20 dB.

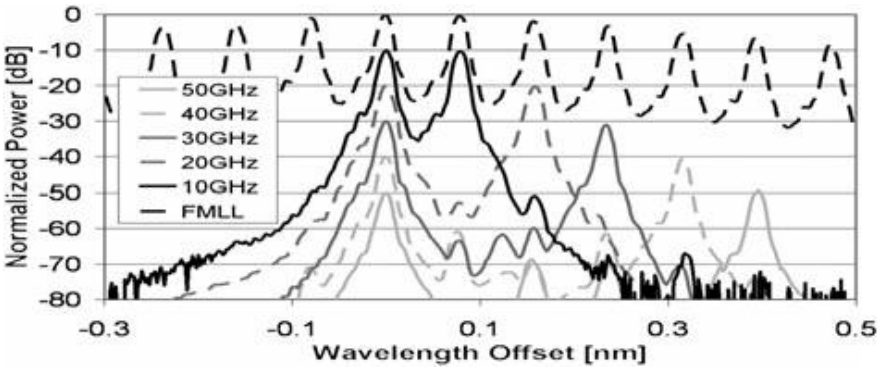

Figure 3.6 Optical spectrum of the FMLL and the selected modes at multiple frequencies.

The relative phase noise measurements are shown in Figure 3.7, where the phase noise values are compared between the 10 and 40 GHz RF generation for both optical and electrical carrier. The 40 GHz phase noise level increases for lower frequencies and, as expected it is slightly higher for higher carrier frequencies and shifted up of few dBs.

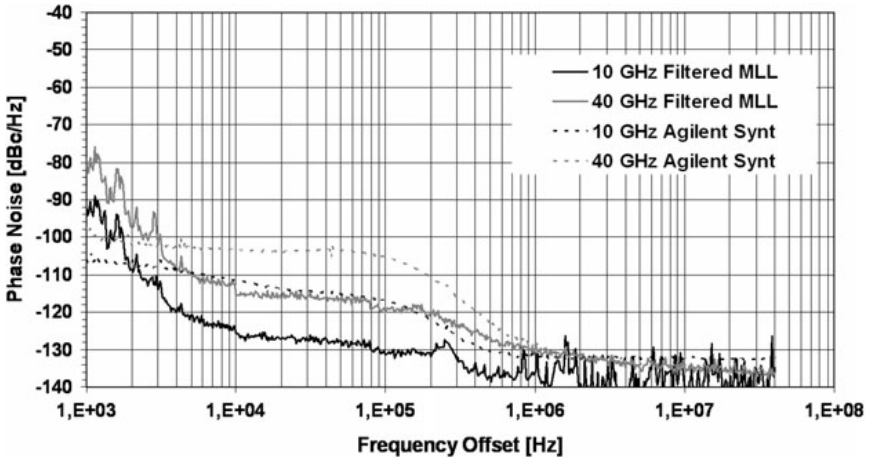

Figure 3.7 Phase noise levels at different carrier frequencies (10 and 40 GHz) for the FMLL and for Agilent synthesizer.

In this case the frequency interval starts from 1 kHz in order to better distinguish each line. Each curve decreases rapidly with the offset frequency, reaching very low levels from around 5 kHz. In this experiment the two carriers are simultaneously generated. Accordingly, this set-up shows a non-perfect

equalization of the selected modes and the loss of responsivity of the photodiode. As a consequence, phase noise degradation at higher frequencies has been experimented. As shown in Figure 3.7 the optical microwave generation performs better than the classical electrical generation in particular starting from 5 kHz.

The time jitter analysis has been carried out separately for each RF generated carrier when the others have been switched off. Under this assumption, the evaluated time jitter (see equation (3.1.8)) appears to be constant for the multicarrier generation, with frequency integration upper limit fixed to 40 MHz, where the thermal noise is dominant (Figure 3.8).

It should be noted that considering an integration interval starting from 100 Hz up to 1 MHz (where the thermal noise is not dominant), the time jitter values for 10 and 40 GHz generated carrier are still comparable [88]. Therefore, the proposed RF generation based on photonic techniques allows generating high stable signals up to the W band suitable for the new generation of radar applications.

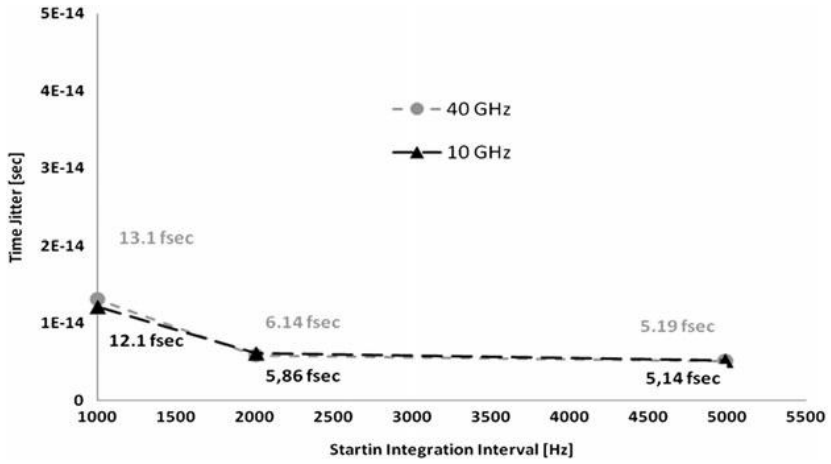

Figure 3.8 Time jitter evaluation for a filtered MLL at 10 and 40 GHz.

3.1.4. Conclusions

The architecture of a photonic microwave radar transmitter based on the beating in a photodiode of two laser modes coming from a MLL has been presented in this paper. The stability performances in terms of time jitter of the RF source have been evaluated at 10 and 40 GHz. The results, at 10 GHz, show excellent spectral purity above 5 kHz for the proposed technique compared to a state of the art Agilent synthesizer even though the time jitter increases for integration time greater than 10 ms. This architecture offers the capability for reconfigurable transmission, as a matter of fact by tuning the filters it is possible to select laser modes at different detuning frequencies, thus generating into the photodiode an RF

carrier at any multiple frequency of the laser repetition rate. Moreover, the evaluated performances are guaranteed up to ultra-high frequencies (an example at 40 GHz have been presented) differently from conventional microwave sources whose performance strongly deteriorates with increasing frequencies. The proposed technique represents a cost-effective solution for microwave signal generation and has also been proposed for digitizing the received signal via an electrooptical sampling.

3.2.PHASE CODED SIGNAL GENERATION BASED ON STANDARD MZM

3.2.1. Principle of operation

To optically generate a phase-modulated RF signal at a specific carrier frequency f_c, it is necessary to heterodyne two stable continuous-wave (CW) lasers with a frequency detuning $\Delta\nu=f_c$, one of which must be phase modulated. The practical problem in this procedure is to process the two lasers independently without affecting their reciprocal phase stability. In fact, if both the lasers are modulated by a baseband signal in the same setup, the phase information would be lost after the heterodyning. Therefore if two lasers are modulated by a signal centered at intermediate frequency f_{IF}, new sidebands are generated in the optical spectrum at $\pm f_{IF}$ from each laser. If the original laser carriers are not suppressed during the modulation process, after the photodetection several components are present, including those centered at frequency $\Delta\nu\pm f_{IF}$ that are the beating between the original unmodulated laser modes and the newly generated sidebands, which bring the desired modulation including the phase. Therefore an RF filter centered at $\Delta\nu\pm f_{IF}$ will permit to select the desired RF signal.

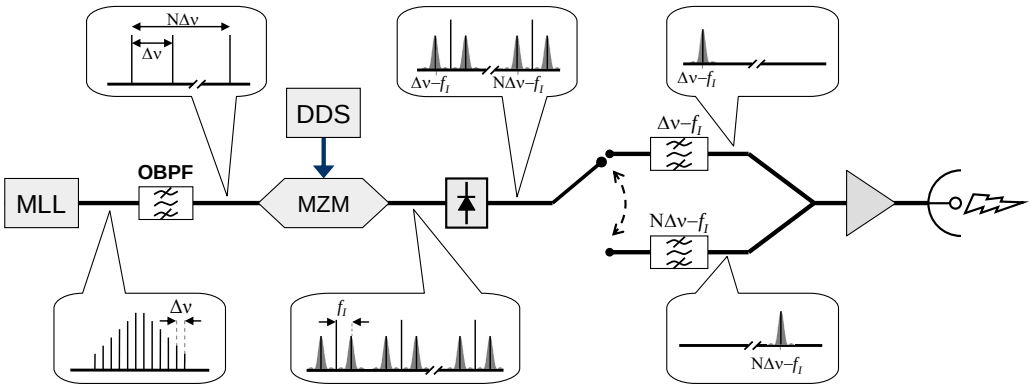

Figure 3.9 .Experimental setup

This scheme can be easily extended to generate flexible carrier radar signals if more than two CW lasers (e.g., the laser comb provided by a MLL) are modulated by the signal centered at f_{IF} and heterodyned in a photodiode with sufficient bandwidth (see Figure 3.9). In this case, phase-modulated RF signals are generated at $\pm f_{IF}$ from any beating frequency between the considered lasers. Then a set of RF filters can be used to select the signal at the desired carrier frequency.

The operation of modulating the RF carriers with a signal at intermediate frequency must not affect the phase stability of the unmodulated carriers. An

interesting solution is generating the modulating signal with a low-frequency high-quality direct digital synthesizer (DDS), which also allows to flexibly change the modulating waveform and the intermediate frequency, thus realizing a software-defined radar signal.

To better explain the principle of operation, in particular when the laser comb from a MLL is exploited, we add here a more formal description of the involved signals. If we take into account a series of N+1 laser modes produced by a MLL, the time domain signal can be expressed as:

$$s_{MLL}(t) = \sum_{n=0}^{N} A_n \cos[2\pi(\nu + n\Delta\nu)t] \quad (3.2.1)$$

where A_n is the modes amplitude, ν represent the mode optical frequency, and Δν is the mode spacing given by the laser repetition rate. Let's consider a modulating signal centered at intermediate frequency, whose time domain expression is:

$$s_{IF}(t) = rect_T(t)\cos[2\pi f_{IF} t + \varphi(t)] \quad (3.2.2)$$

where f_{IF} is the intermediate frequency (IF), $\varphi(t)$ is the phase modulation carried on the IF, and the function $rect_T(t)$ represents the pulsed signal with a limited time duration T and bandwidth B=1/T (the typical shape of a radar pulse).

The amplitude of the optical signal $s_{MLL}(t)$ is modulated by the signal $s_{IF}(t)$ (with a modulation depth M):

$$s_{MOD}(t) = s_{MLL}(t) \cdot [1 + M \cdot s_{IF}(t)] \quad (3.2.3)$$

that becomes

$$s_{MOD}(t) = \sum_{n=0}^{N} \{B_n \cos[2\pi(\nu + n\Delta\nu)t] + C_n \cos[2\pi(\nu + n\Delta\nu \pm f_{IF})t + \varphi(t)] \cdot rect_T(t) \quad (3.2.4)$$

with B_n and C_n amplitude terms.

After the heterodyning in a photodiode, we obtain the beatings of all the different carriers, i.e.

$$s_{PD}(t) = \sum_{n=0}^{N} \{D_n \cos[2\pi(n\Delta\nu \pm f_{IF})t + \varphi(t)]rect_T(t) + E_n \cos(2\pi n\Delta t)\} + [\ldots] \quad (3.2.5)$$

where the first term represents the phase-modulated signal upconverted to nΔυ±fIF, and the second term represents the beatings between the unmodulated carriers; Dn and En are the amplitudes of the components; […] denotes the omitted beatings between all the sidebands at υ+nΔυ±f_{IF}, the component at DC, and the components at twice the optical frequency. A graphical representation of the optical components at the input of the photodiode and of the beatings of interest is reported in Figure 3.10.

The frequency carrier desired for transmission can be finally selected by exploiting an RF filter with central frequency nΔυ-f_{IF} (or nΔυ+f_{IF}), with 0<n<N:

$$s_{TX}(t) = \cos[2\pi(n\Delta\nu - f_{IF})t + \varphi(t)]rect_T(t) \quad (3.2.6)$$

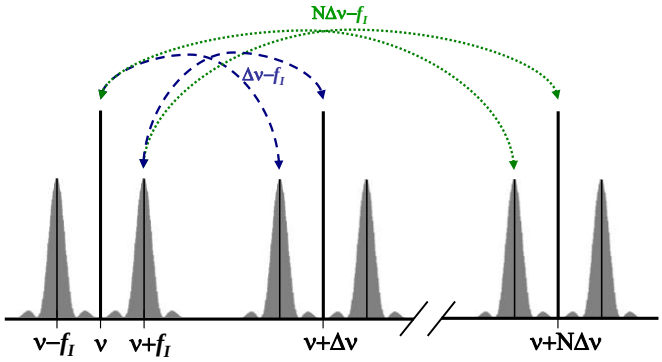

Figure 3.10 Optical spectrum before the photodiode.

3.2.2. Experiment set up

Figure 3.9 reports the exploited experimental setup. The laser source is a regenerative fiber MLL with a repetition rate of 10GHz, an optical bandwidth of 250GHz, and an output power of about 13dBm. An optical band-pass filter (OBPF) with a bandwidth of 0.4nm selects a bunch of about five adjacent modes, which are launched into a Mach-Zehnder modulator (MZM) biased at its quadrature point. The optical modes are modulated by the electrical signal generated by a 16-bit 400Msample/s DDS. The modulating signal is a phase-coded RF pulse centered around f_{IF}=100MHz or f_{IF}=184MHz, which will be used to generate RF signals respectively at 9.9GHz and 39.816GHz, as explained in the

following. The RF pulse has a duration of 5μs and a repetition time of 15μs. In the experiment, two different phase codes will be used, the linear chirp and the Barker code, which will be described in the following. Figure 3.11 reports a time domain representation (at an arbitrary low frequency, for the sake of clarity) of the RF pulse in the two considered case.

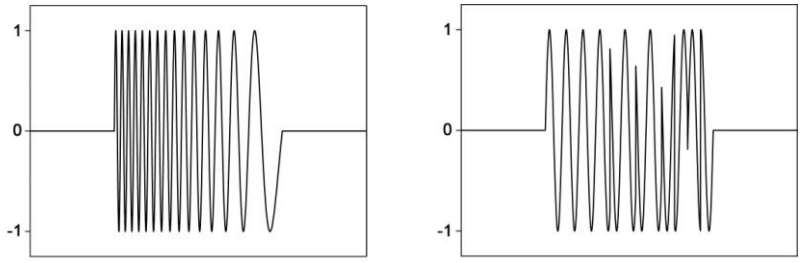

Figure 3.11 Time domain representation (at an arbitrary low frequency) of the applied phase-coded RF pulses

The modulation produces sidebands around each laser modes, and when the optical signal thus generated is detected by a 50GHz-bandwidth photodiode, all the beatings between modes and sidebands are produced. Two RF filters with a bandwidth of 40MHz and centered at 9.9GHz and at 39.816GHz are then used to alternately select the phase-modulated signal when f_{IF} is respectively equal to 100MHz and 184MHz (in order to match the center frequency of the filters), and a broadband electrical amplifier with a gain of 27dB allows to perform the analyses.

3.2.3. Results

First, the phase noise of the signal at 9.9GHz is analyzed to study the effect of the modulation at f_{IF} on the phase stability of the carrier. The frequency-shifted signal, generated with the DDS programmed to emit only a sinusoid at 100MHz, is measured by means of a signal source analyzer (SSA), and compared with the signal generated by the beating of the original laser modes at 10GHz, and with the phase noise of the shifting signal at 100MHz. The phase noise curves are reported in Figure 3.12(left). As shown by the graphs, the signal generated by the low-frequency high-quality DDS presents a lower phase noise than that of the carrier at 10GHz. Therefore the frequency shift induced on the optical modes does not affect the stability of the desired carrier at 9.9GHz, which shows the same behavior as the non-shifted one. Only a higher noise floor is present for frequency offset above 100kHz, which is due to the higher thermal noise in the measure and can be reduced with a more accurate amplification.

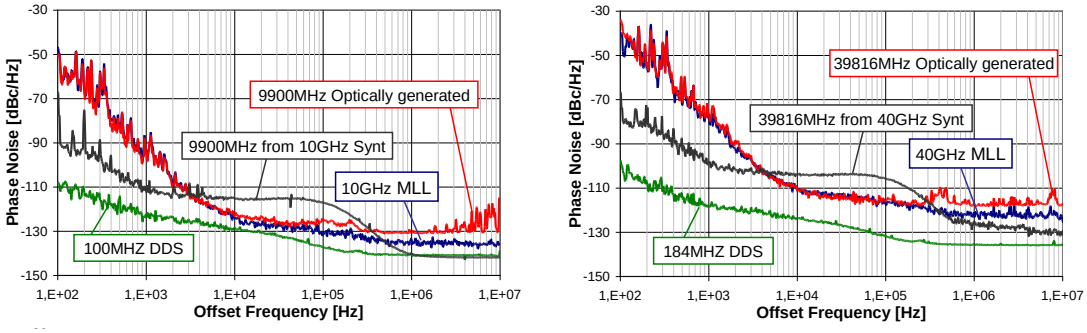

Figure 3.12 Phase noise of the generated carriers

By changing the RF-filter and resetting the DDS output to 184MHz, a 39.816GHz carrier is produced. Figure 3.12(right) shows that the phase stability of the carrier at 39.816GHz is also not affected by the shifting process, and the comparison with the synthesizer curve confirms that the proposed scheme is suitable for generating high-frequency signals for coherent radar systems, performing better than an electronic-based approach. In this case the integration of the curves gives an rms time jitter of 16.1fs for the optically generated carrier and 16.3fs for the conventionally generated one.

In order to demonstrate the effectiveness of the proposed scheme, it has been characterized by generating radar pulses implementing the most used pulse-compression techniques. The DDS is first set to generate a 25MHz linear chirp around 100MHz, i.e. a linear frequency sweep from 87.5MHz to 112.5MHz, and the RF filter centered at 9.9GHz is used. The choice of such a frequency deviation is due to the limited bandwidth of the available RF filters and of the DDS, but in principle the only bandwidth limitation is given by the precise DDS (hundreds of MHz) and by the MLL repetition rate, which must be high enough to prevent overlaps between different carrier frequencies. The modulated signal obtained with the proposed setup is analyzed by the SSA in terms of frequency and amplitude transients, as reported in Figure 3.13(left). The graph shows that the signal generated by the DDS is perfectly upconverted to 9.9GHz, producing a linearly chirped pulse across 25MHz. This proves that the proposed schemes is capable of effectively upconvert amplitude- and phase-modulated signals. Moreover, the pulsed amplitude shows an extinction ratio of about 40dB, even if a minor ripple is present on the right side of the pulses, caused by the narrow bandwidth of the RF filter

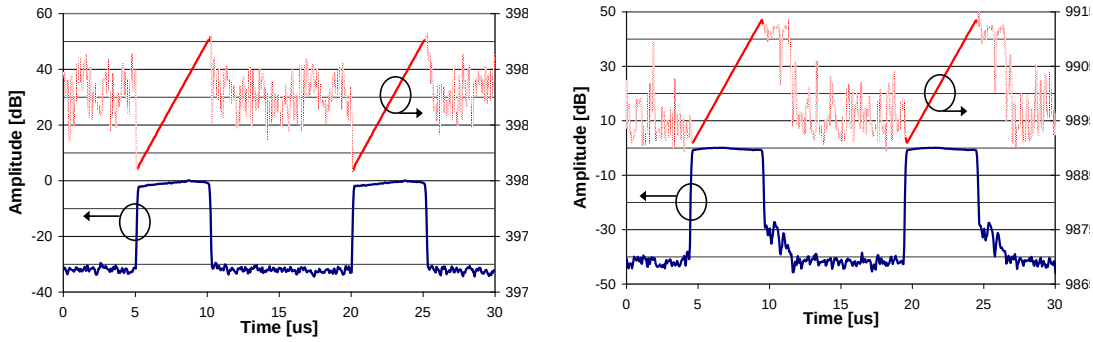

Figure 3.13 Frequency and amplitude transients of the signals measured with the SSA

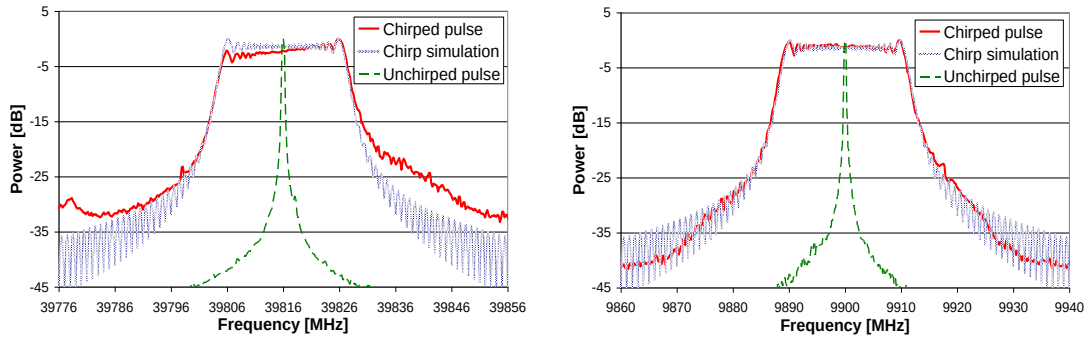

Figure 3.14 Measured electrical spectrum (RBW 100kHz) of the chirped pulses

Finally, Figure 3.14(left) reports the electrical spectrum, acquired with a 40GHz-bandwidth electrical spectrum analyzer (ESA), of the generated signal, compared with the simulated spectrum of an equivalent ideal chirped signal, showing an almost perfect match. The spectral broadening of the compressed pulse with respect to the unchirped RF pulse of the same time duration is reported in Figure 3.14(left). Since the spatial resolution ΔR of a radar system is proportional to the inverse of the signal bandwidth B ($\Delta R=c/2B$), if we use a chirped signal with a frequency deviation ΔF the range resolution becomes $\Delta R=c/(2\Delta F)$. In our case, where the signal bandwidth of the uncompressed pulse is 200kHz (a 5µs pulsed signal) and the chirp frequency deviation is 25MHz, we obtain an increased radar resolution from 750m to 6m.

By setting the DDS to generate a chirped signal centered at 184MHz and replacing the RF filter, a modulated pulsed signal at 39.816GHz is produced. The analyses reported above are applied for this case as well. In Figure 3.13(right), a lower extinction ratio is reported on the amplitude transients with respect to the case at 9.9GHz, which is due to a higher noise floor of the SSA when measuring high-frequency signals. The electrical spectrum reported in Figure 3.14(right) appears to be tilted with respect to the ideal case, with the spectral components at lower

frequencies slightly weaker than the higher frequencies. This is caused by the analog bandwidth of the DDS which is limited to 200MHz: since the chirped signal runs from 196.5MHz to 171.5MHz, its high-frequency components are slightly attenuated and transferred to the carrier at 39.816GHz. The effectiveness of the employed pulse-compression technique is also proven by the autocorrelation function (AF), calculated from a single shot trace acquired with a 40Gsample/s real-time oscilloscope, and reported in Figure 3.15. From the graph the obtained compression is clearly evident, especially compared with the AF envelope of an unchirped pulse (dotted line). Due to the limited bandwidth of the oscilloscope the AF is related to the 9.9GHz case only but, as demonstrated by the SSA and ESA traces, there are no reasons to suppose that the 39.816GHz case would be different.

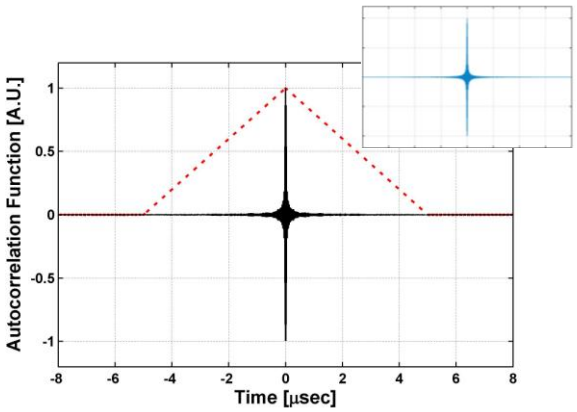

Figure 3.15 Autocorrelation function (AF) of the chirped pulses extracted from the real-time oscilloscope trace

Another frequently exploited pulse-compression technique is the binary phase coding using the Barker codes. These are particular sequences of N values a_j in the set (-1, +1) for j=1, 2,…, N, such that

$$\left| \sum_{j=1}^{N-m} a_j a_{j+m} \leq 1 \right| \qquad (3.2.7)$$

for $1 \leq m < N$. They are applied to radar pulses by dividing the pulse in N subpulses of equal duration, and modulating the carrier phase in each subpulse by 0° or 180° according to the adopted Barker code. Thanks to the coding, these kind of radar pulses show an autocorrelation peak N times narrower, and autocorrelation sidelobes N times smaller, than the AF of the uncompressed pulse. This means that, by analysing the cross-correlation between the detected radar echo and the

transmitted pulse, an N-times increased resolution can be obtained with respect to the unmodulated radar pulse, with a sensitivity improvement of $\log_{10}N$ dB, without reducing the pulse duration and thus avoiding an increase in the transmitted peak power. The code length N can range from 2 to 13 bits and determines the range resolution improvement according to the equation $\Delta R=c/2BN$. In our experiment we have used the longest code, i.e. +1, +1, +1, +1, +1, −1, −1, +1, +1, −1, +1, −1, +1, since it provides the best compression factor of 1/13 with respect to the uncompressed pulses. The DDS is set to generate a coded pulse at 100MHz, and the 9.9GHz RF filter is used. The phase-modulated signal obtained is analyzed by the SSA in terms of phase and amplitude transients, as reported in Figure 3.16(left).

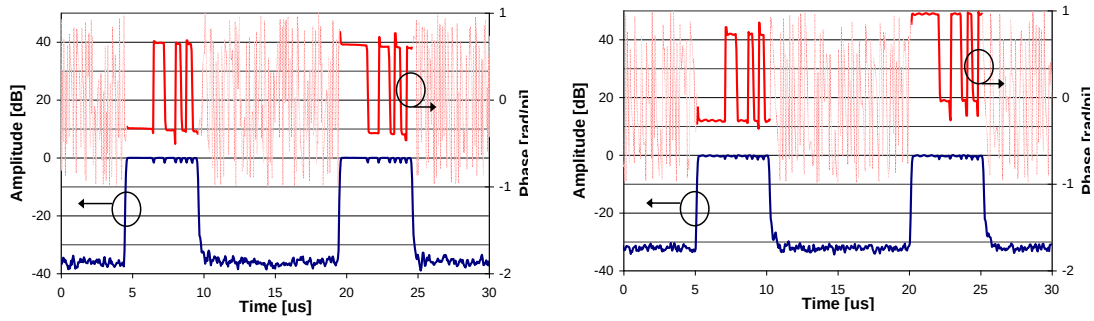

Figure 3.16 Phase and amplitude transients of the signals measured with the SSA

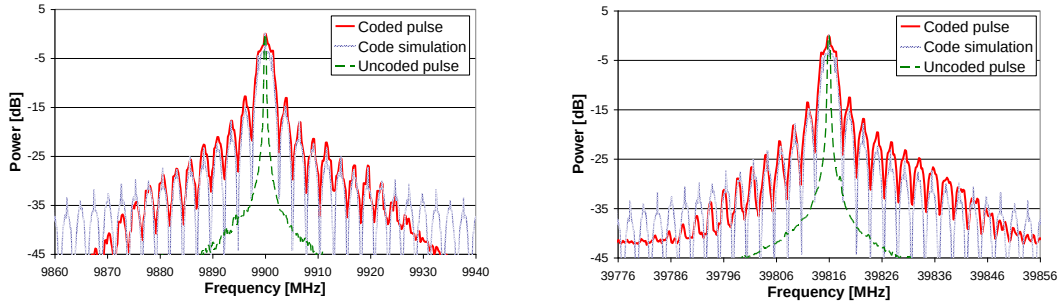

Figure 3.17 Measured electrical spectrum (RBW 100kHz) of the phase-coded pulses.

The graph shows that the signal generated by the DDS is again perfectly upconverted to 9.9GHz, producing 180° phase jumps in the pulses Figure 3.17(left) reports the electrical spectrum of the generated signal, compared with the simulated spectrum of an equivalent ideal coded signal, showing again an almost perfect match. The spectral broadening of the compressed pulse with respect to the uncoded RF pulse of the same time duration, reported in Figure 3.17(left), reveals an increased radar resolution up to 57.7m. By setting the DDS to generate a phase-coded signal at 184MHz and replacing the RF filter, a phase-

coded pulsed signal at 39.816GHz is produced. The analyses reported above are applied for this case as well, and are shown inFigure 3.16(right) and Figure 3.17(right).

In Figure 3.18 the autocorrelation function of the generated Barker coded pulse at 9.9GHz is shown. As expected from the radar theory, the normalized amplitude presents sidelobe peaks at 0.07 (1/N) and corresponds well to the simulated AF of the sequence shown in the inset. So the suitability of the proposed scheme for producing phase-coded radar signals is confirmed. With the particular code exploited, the range resolution is improved by a factor of 13 from 750m (relative to the unmodulated pulses) to 57.7m.

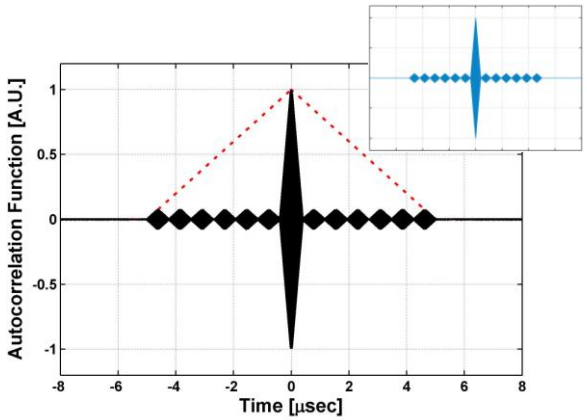

Figure 3.18 Autocorrelation function of the Barker-coded pulses extracted from the real-time oscilloscope trace

3.2.4. Conclusions

The proposed method for the generation of frequency-agile phase modulated RF signals can be of help in a large number of applications. Besides coherent radars, it can be used wherever phase modulated RF signals are needed, as for example in radio-over-fiber systems for the generation of complex modulation formats (e.g., 64QAM), or in the removal of the range ambiguity in radars and lidars [96].

Different applications and scenarios may require different carrier frequencies and modulation bandwidths, so it is necessary to choose the MLL's repetition rate carefully. A MLL with high repetition rate can allow wide-band modulation, since carrier's overlap is avoided, but it would reduce the number of available frequencies since the bandwidth of the commercial photodiodes is limited to about 100GHz. On the other hand, a low repetition rate MLL can allow a dense set of available frequencies, but reduces also the possible modulation bandwidth. As demonstrated by our measurements, the phase stability of the generated RF pulses depends on the timing jitter of the original MLL. Therefore, the better the MLL,

the better the RF signal. As it is evident, if an ultra-low-noise MLL is used as laser source [97], then the noise-limiting element becomes the exploited DDS. Although the proposed system requires readily available components, photonic hybrid integration my be helpful to further reduce the complexity of the setup [97]. This way all the optical path could be replaced by a single monolithic structure with reduced footprint, allowing its implementation even in mobile systems.

In conclusion, we have proposed an innovative scheme that exploits photonics for generating arbitrary phase-modulated RF pulses with flexible carrier frequency, and phase stability suitable for coherent radar systems. The use of a low-frequency high-quality DDS permits the maximum flexibility in the generation of software-defined modulating signals which are transferred to the modes of a MLL, without affecting their reciprocal phase stability. The digital signals are generated at an intermediate frequency, so that after detecting the optical signal, phase-modulated RF pulses can be obtained close to any multiple frequency of the MLL repetition rate, even at frequency in the EHF band. The reported experimental results confirm the generation of linearly chirped and phase-coded RF pulses with carrier frequencies of about 10GHz and 40GHz with very high phase stability, and demonstrate a spectral broadening suitable for pulse compression techniques. The flexibility of the scheme allows to implement any kind of modulation (e.g., Frank codes) at any carrier frequency. By properly choosing the MLL repetition rate, frequency agility can be implemented on close or far frequencies (as in frequency hopping or in multifunctional radars, respectively), or even both, with the advantage of a single MLL instead of a series of electronic oscillators for each carrier frequency. The carriers can be generated simultaneously or alternately, or even changed continuously. The modulating signal can also be changed meanwhile, implementing a waveform diversity technique.

Therefore the proposed technique allows the practical realization of compressed pulses for coherent radars over a wide carrier frequency range, allowing the development of software-defined systems with improved functionalities.

3.3.PHASE CODED SIGNAL GENERATION BASED ON I\Q MZM

3.3.1. Principle of operation

Given two stable CW lasers, as for examples two modes of a MLL, a phase coded RF signal is obtained if one of the CW lasers is phase modulated before they are heterodyned in a photodiode (PD). To do so, the two CW lasers should be separated along different paths by splitting and filtering, in an environmentally stable ad-hoc structure. A similar result can be achieved in a more flexible scheme which does not require wavelength-specific integrated components.

The scheme of principle of the proposed phase-modulated RF generation method is sketched in Figure 3.19. Let's consider two modes of a MLL at frequencies ν_1 and $\nu_2=\nu_1+\Delta\nu$, with equal amplitude. The field can be expressed as

$$E_a(t) = A_a\left\{\exp\left[i\omega_1 t\right]+\exp\left[i\omega_2 t\right]\right\} \qquad (3.3.1)$$

where $\omega_1=2\pi\nu_1$, $\omega_2=2\pi\nu_2$ and A indicates the field amplitude.

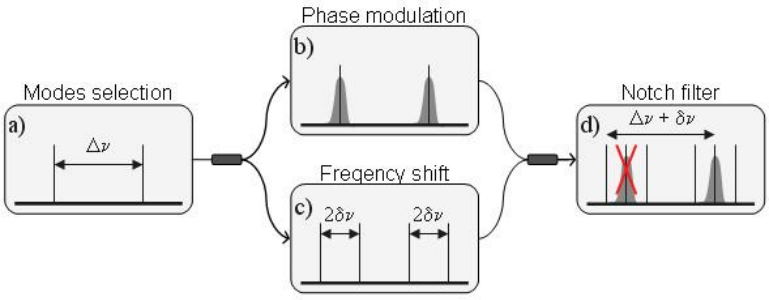

Figure 3.19 Ideal scheme of principle

The signal is split along two different paths. In the first path both the CW lasers are phase modulated. This can be done in a common $LiNbO_3$ phase modulator. In the second path, they are both suppressed to generate new slightly shifted components by a carrier-suppressed amplitude modulation driven by a low-phase-noise sinusoidal signal, generating two ±1-order sidebands. This operation can be realized in a common $LiNbO_3$ Mach-Zehnder modulator driven in its minimum transmission point. The fields in the two paths are respectively

$$E_b(t) = A_b \{\exp[i\omega_1 t] + \exp[i\omega_2 t]\} \cdot \exp[i\phi(t)] \quad (3.3.2)$$

$$E_c(t) = A_c \{\exp[i(\omega_1 - \omega_m)t] + \exp[i(\omega_1 + \omega_m)t] + + \exp[i(\omega_2 - \omega_m)t] + \exp[i(\omega_2 + \omega_m)t]\} \quad (3.3.3)$$

where $\omega_m = 2\pi\delta\nu$ is the frequency-shifting signal. The signals $E_b(t)$ and $E_c(t)$ then are coupled together. The resulting signal shows six spectral components. Let's suppose we want to obtain a phase-modulated RF signal at the nominal frequency of $\Delta\nu+\delta\nu$. In the obtained signal $E_d(t)$, two pairs of components are at a nominal frequency difference of $\Delta\nu+\delta\nu$ (the components at ν_1 and at $\nu_2+\delta\nu$, and the components at $\nu_1-\delta\nu$ and at ν_2), and one of the components in each pair is phase-modulated by $\phi(t)$ (respectively, ν_1 and ν_2). In more details, the frequency difference of the components in the two pairs is $\Delta\nu+\delta\nu+d\phi(t)/dt$ and $\Delta\nu+\delta\nu-d\phi(t)/dt$, respectively. If these components pairs were both heterodyned in a PD, they would both generate an RF signal at a frequency carrier of $\Delta\nu+\delta\nu$, but one RF signal would be phase-modulated by $\phi(t)$ while the other would be modulated by $-\phi(t)$, giving:

$$s(t) = A_s \exp[i\omega_{RF} t] \cdot \{\exp[i\phi(t)] + \exp[-i\phi(t)]\} + [\cdots] \quad (3.3.4)$$

where $\omega_{RF}=\Delta\nu+\delta\nu=\omega_2-\omega_1+\omega_m$, and […] indicates omitted terms which will be rejected by a successive RF filter. The expression (4) shows that the RF signal at $\Delta\nu+\delta\nu$ filtered out after the PD would present a modulated envelope whose shape would be given by $cos[\phi(t)]$. Therefore, before heterodyning the entire spectrum in the PD, one of the components in the two pairs at ω_{RF} must be suppressed. This can be done by filtering out either one of the phase-modulated modes from the MLL, or one of the $\delta\nu$-shifted new components.

Considering to optically filtering out the phase modulated laser mode at ω_1 using a notch filter, the RF signal at the output of the photodiode can therefore be expressed as

$$s(t) = A_s \exp\{i[\omega_{RF} t + \phi(t)]\} + [\cdots] \quad (3.3.5)$$

The expression (3.3.5) represents a phase modulated RF signal at the desired frequency ω_{RF}. The same analysis can be done considering the beating at $\Delta\nu$-$\delta\nu$ as the nominal carrier frequency.

The operations described above can be easily implemented exploiting a commercial optical I/Q modulator, using the bias voltage which controls the reciprocal phase shift between the two branches (usually named as Bias P), to modulate the phase of the two CW lasers. This device is an integrated structure in $LiNbO_3$, which ensures the necessary stability against environmental fluctuations. The carrier-suppressed frequency shift on one arm of the I/Q modulator can be driven by a very stable low-frequency RF oscillator, without affecting the original reciprocal phase stability of the modes from the MLL. Moreover, the optical I/Q modulator also has an additional MZ modulator, which can be used for modulating the amplitude of the original laser components from the MLL, thus allowing the realization of phase-modulated RF radar pulses.

The proposed scheme therefore allows the photonics-based realization of phase-modulated RF pulses exploiting a single commercial device, with a significant simplification with respect to the previously presented photonics architectures.

3.3.2. Experiment set up

The experimental setup is reported in Figure 3.20.

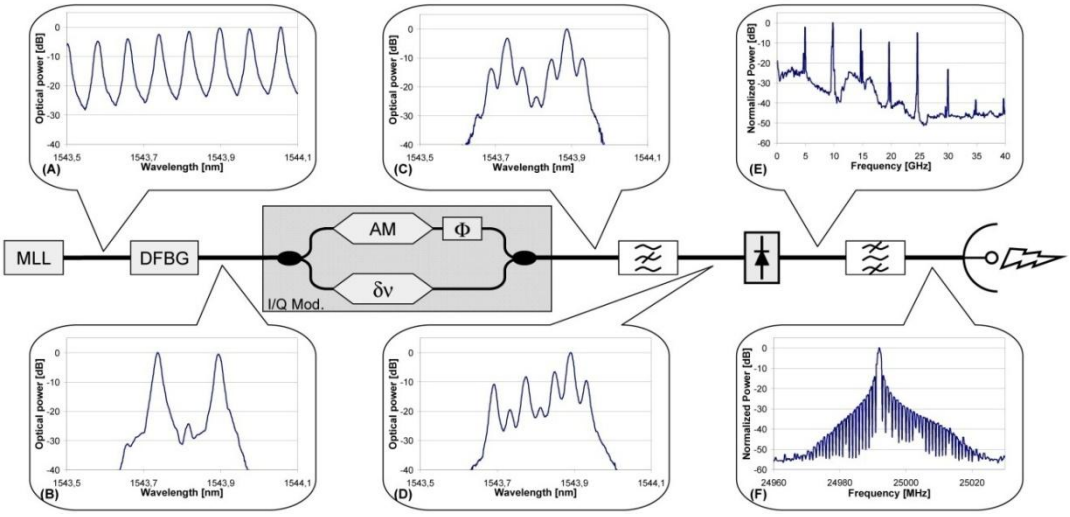

Figure 3.20 Experimental setup.

The exploited laser source is a regenerative fiber MLL with a repetition rate of 9953MHz and a central wavelength of 1554.5nm. A zoom of its optical spectrum is reported in the inset (A) of Figure 3.20. A dual fiber Bragg grating (DFBG) [98] selects two non-adjacent modes at a detuning of 20GHz, with a suppression of 25dB of the undesired adjacent modes (inset (B)). The two selected modes are then launched into an optical I/Q modulator. This is a Covega LN86 device, with an electro-optical bandwidth of 14GHz for both the MZs along the two branches. Along one of the arms of the I/Q modulator a carrier suppressed modulation is obtained by setting the relative MZ modulator to the minimum transmission point [99][100]. The modulation is driven by a precise waveform synthesizer producing a sinusoidal signal at $\delta\nu$=5086MHz with an amplitude of $0.6V_{\pi}$, thus splitting the two modes into four new spectral components at +/-$\delta\nu$ from the original modes. The second arm of the I/Q modulator is also exploited, introducing an on/off amplitude modulation (AM) on the two selected modes in order to form the radar pulses. A waveform generator modulates both the laser modes with a rectangular pulse with a duration of 1μs over a period of 3μs, and a modulation depth close to 1. Finally, the reciprocal phase difference of the two modulator branches is modulated by means of a 1GSample/s DDS, opportunely amplified and applied to the Bias P port of the I/Q modulator. The optical spectrum of the output signal from the I/Q modulator is reported in the inset (C), where the four modes at +/-5086MHz from the original two laser modes are evident. In order to suppress one of the two original carriers from the MLL, a FBG with a bandwidth of 6GHz is used as a notch filter (inset (D)), and the resulting signal is sent to a 50GHz-bandwidth photodiode. The inset (E) shows the electrical spectrum after the photodiode, where several beatings take place. An RF filter centered exactly at 25000MHz with a bandwidth of 25MHz selects the beating of interest at 24992MHz between the non-suppressed amplitude-modulated original laser mode, and the laser line obtained by shifting the other original mode of $\delta\nu$ (inset (F)). The choice of a carrier frequency not perfectly aligned with the RF filter is determined by the need of keeping the RF signal below 25GHz, in order to perform the measurements with a 50Gsamples/s real-time oscilloscope.

3.3.3. Results

Since the coherent radar systems require high phase stability, the generated signal has been first characterized in terms of phase noise. Figure 3.21 shows the measured phase noise of the generated 24992MHz carrier, compared with the phase noise of the beating generated by the two modes from the original MLL, and with the frequency shifting signal at 5086MHz generated by the synthesizer.

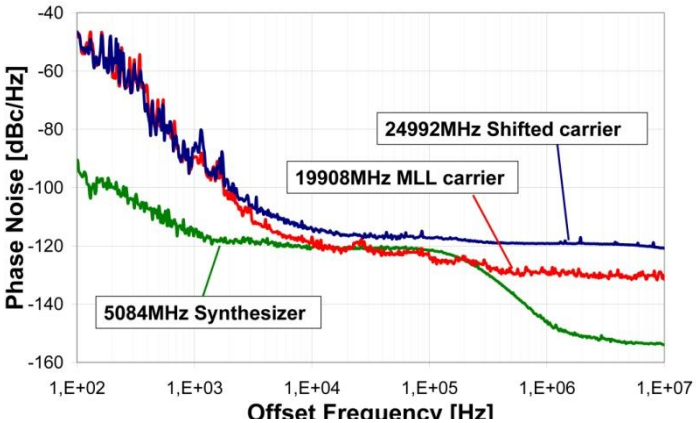

Figure 3.21 Phase noise measure of the 24.992GHz carrier compared with the phase noise of the non-shifted carrier from the MLL, and of the synthesizer.

For this analysis a continuous wave RF carrier has been generated, turning off both the phase and amplitude modulations. The phase noise is measured with a Signal Source Analyzer (SSA, Agilent E5052A) for offset frequency from 100Hz – given by the common duration of a coherent radar measurement – to 10MHz – upper limit due to the RF filter. The graph shows that the phase noise of the synthesizer is lower than the one of the MLL, except for the range of offset frequency from 10kHz to 100kHz where they are substantially equal. This would suggest the possibility to generate a frequency shifted RF signal with the same noise behavior of the original MLL. Actually, Figure 3.21 reports that the phase noise curve of the generated RF signal at 25GHz follows the behavior of the 20GHz signal at low offset frequency, but shows slightly higher phase noise from 2kHz on, and a noise floor 10dB higher for high offset frequency. We believe that this behavior is due to the added phase noise introduced by the broadband electrical amplifier exploited to boost the output signal from the photodiode, and could be improved using a low-noise narrow-bandwidth specific amplifier. Nevertheless the integration of the curves in Figure 3.21 over the entire offset frequency range shows that the obtained RF signal has a timing jitter of 286fs (equivalent to 45mrad at 24992MHz), which is only 21fs higher than that of the original MLL. The exploited MLL is a free running fiber ring laser which shows very low phase noise at high offset frequency, but is affected by mechanical vibrations that induce high phase noise at low offset frequency. It is important to note that it is possible to strongly reduce this noise if the MLL is used as an optical voltage controlled oscillator in a phase-lock loop, where a stable low-noise reference clock is used to lock the phase of the MLL at low frequency offset. This way an extremely precise optical source can be obtained [92]. It is also interesting to note here that the MLL allows to generate RF signals over a wide frequency

range by selecting modes at different detuning, without changes in the phase noise performance [101].

Once the quality of the signal is confirmed, radar pulses with no phase modulation are generated in order to be compared with the compressed ones. In Figure 3.22 the autocorrelation function (AF) of the pulses is reported, calculated from a single-shot acquisition of a 50Gsamples/s real-time oscilloscope. The receiver in a radar system operates the cross-correlation between the transmitted pulse and its echo, therefore the signal AF brings important information on the radar resolution, as will be evident in the following. In the case of non-coded pulses, the resolution is easily equal to $cT_p/2$, where c is the speed of light and T_p is the radar pulse duration, which leads to a resolution of 150m for the considered non-coded pulses of 1μs.

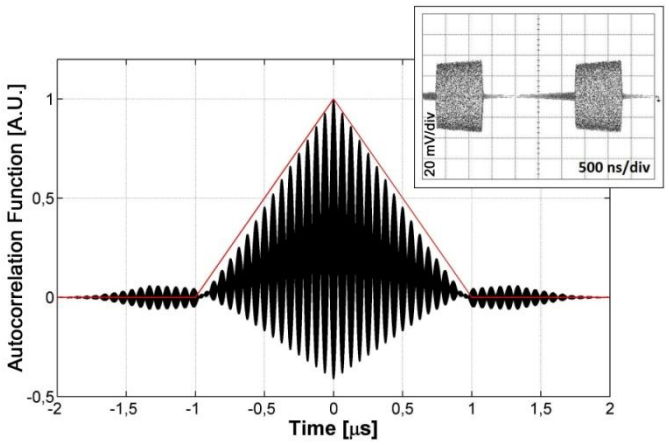

Figure 3.22 Calculated autocorrelation function (AF) of the optically generated RF pulse.

In Figure 3.22, the AF of the optically generated RF pulse is compared with the AF of an ideal base-band pulse of equal duration. As shown in the picture, the base-band AF fits well the envelope of the AF measured at RF, except for its minor side lobes. These are caused by the non-ideal suppression of the unwanted original mode after the optical notch filter, and by the narrow filtering of the RF signal. The effects of these non-idealities are also evident in the inset of Figure 3.22 showing the RF pulse waveform. As the I/Q modulator is not designed to be used as a phase modulator, its characterization is necessary. In Figure 3.23 the result of the characterization is plotted, realized applying a sinusoidal modulation at the Bias-P port and measuring the output amplitude modulation on a CW laser while changing the sine frequency. The Bias-P port shows a constant frequency response up to 7MHz and a sharp cut-off at 20MHz.

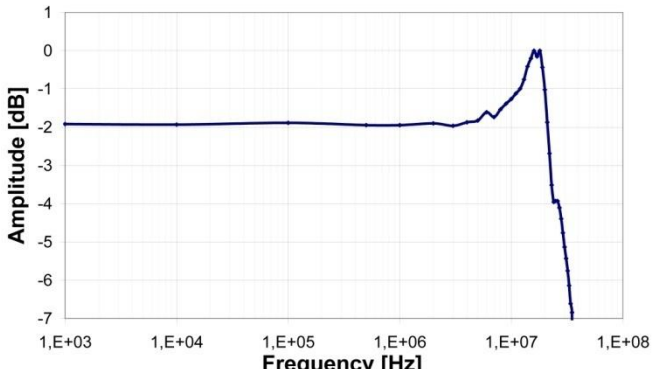

Figure 3.23 Bandwidth characterization of the Bias-P port of the I/Q modulator

Due to this limitation, the modulation bandwidth available with the considered device is limited to few MHz. Nevertheless, since 40GHz-bandwidth phase modulators are commonly implemented with state-of-the-art $LiNbO_3$ technology, we believe that the design of a custom I/Q modulator with wideband phase modulation capability would not present technological issues.

The system is then tested applying two different phase modulations commonly used in radar applications: Barker codes and linear frequency chirp.

Starting from a barker code as discussed in section 3.2.2 they are applied to radar pulses by dividing the pulse in N subpulses of equal duration, and modulating the carrier phase in each subpulse by 0° or 180° according to the adopted Barker code. Thanks to the coding, this kind of radar pulses show an autocorrelation peak N times narrower, and autocorrelation sidelobes N times smaller. This means that, by analysing the cross-correlation between the detected radar echo and the transmitted pulse, a N-times increased resolution can be obtained with respect to the unmodulated radar pulse, with a sensitivity improvement of $\log_{10}N$ dB, without reducing the pulse duration. Figure 3.24(A) reports the signal applied to the Bias-P port (upper trace) for modulating the phase, and the amplitude modulating signal applied to one of the two RF ports (lower trace). The phase-controlling signal corresponds to a 4-bit Barker code (0-0-180-0) and its amplitude is set to match the V_π voltage of the device, i.e. 4.75V. Figure 3.24(B) shows the oscilloscope trace of the radar pulses thus generated. Amplitude discontinuities are present at the phase jumps, and a limited pulse extinction ratio can be observed. Figure 3.24(C) reports the amplitude and phase transients of the radar pulse, as acquired by the SSA. As expected the phase modulation produces 180°-phase jumps in the pulses, while an amplitude extinction ratio of about 20dB is measured. The amplitude transient also shows discontinuities at the phase jumps. The limited extinction ratio and the amplitude fluctuations can be ascribed to the non-ideal suppression of the unwanted original mode after the notch filter, and to the narrow RF filtering. Those effects can therefore be reduced with a better design of both

the optical and RF filters. Moreover, the extinction ratio of the radar pulse is generally improved by the high-power amplification stage before the radar antenna, which can ensure an extinction ratio as high as 120dB

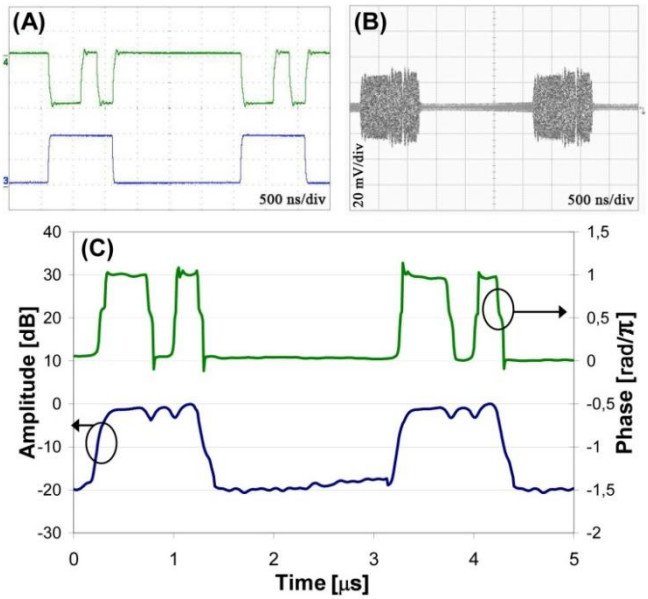

Figure 3.24 Optically generated RF pulses with 4-bit Barker code.

In Figure 3.25 the autocorrelation function of the generated Barker coded pulse is shown. As expected from the radar theory, the normalized amplitude presents sidelobe peaks at 0.25 (1/N) and fits well the simulated envelope of the sequence. So the suitability of the proposed scheme for producing phase-coded radar signals is confirmed. Also, the duration of the AF is 0.25 (1/N) the one of the non-coded pulse. This means that the coding allows the same resolution of a non-coded pulse with four times shorter duration. With the particular code exploited the range resolution is improved to 37.5m.

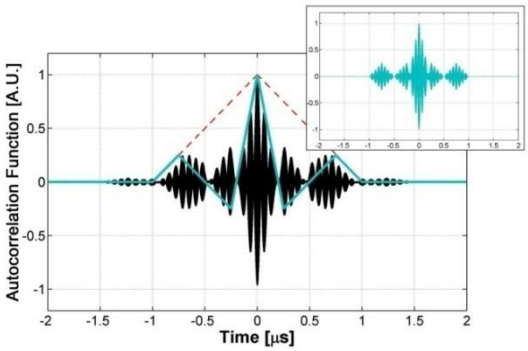

Figure 3.25 Autocorrelation function of the Barker-coded pulses extracted from the real-time oscilloscope trace.

During the experiment, unmodulated radar pulses with a Pulse Width (PW) equal to 4μs and bandwidth B, which guarantees a range resolution of 600m, and a Pulse Repetition Interval (PRI) of 20μs have been also generated. Then, phase codes have been added to the radar pulses. One of the used code is a 13-bit Barker sequence (+++++--++-+-+) which allows to enhance the radar range resolution up to 46m. A phase rotation of 180° has been achieved by modulating the Bias P port with a voltage matched to the modulator quadrature voltage Vπ. In Figure 3.26 the obtained phase transitions measured with the Agilent E5052A Signal Source Analyzer (SSA) are shown (the control signal for the phase modulation is reported in the inset).

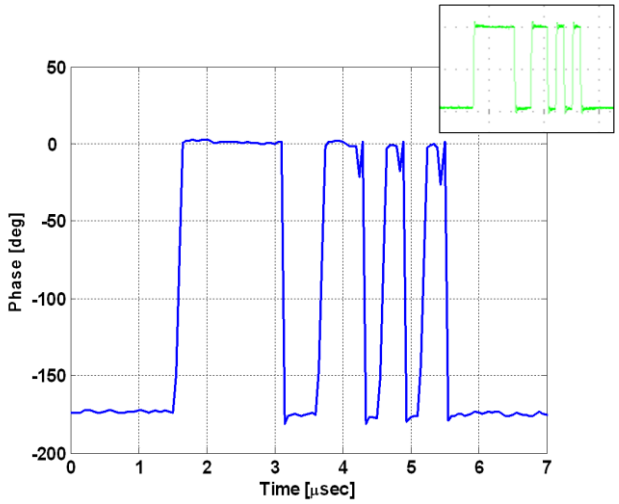

Figure 3.26 Phase transients of 13-Barker code.

The obtained Autocorrelation Function (AF) of the acquired RF phase modulated pulse is shown in Figure 3.27. The trace is compared with the AF of 4μs pulse without modulation (red line), and with the simulated envelope of a 13-bit Barker code (black line). The autocorrelation function exhibits constant side lobe peaks N_{bit} times smaller with respect to the main peak, and a range resolution N_{bit} times improved ($\Delta R=c\backslash 2BN_{bit}$).

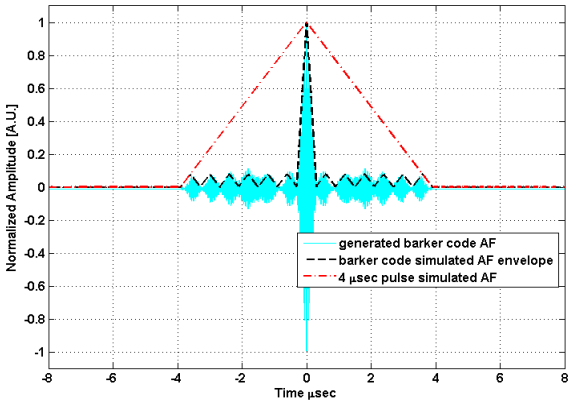

Figure 3.27 Autocorrelation function of the RF 13 bits Barker code.

By using the described scheme we have also generated polyphase codes (Frank codes) where pulses are divided into M group each one further divided into M sub-pulses with a total length code of M^2. Phase transitions of the Frank code are reported in Figure 3.28 as measured by the SSA (the control signal for the phase modulation is shown in the inset).

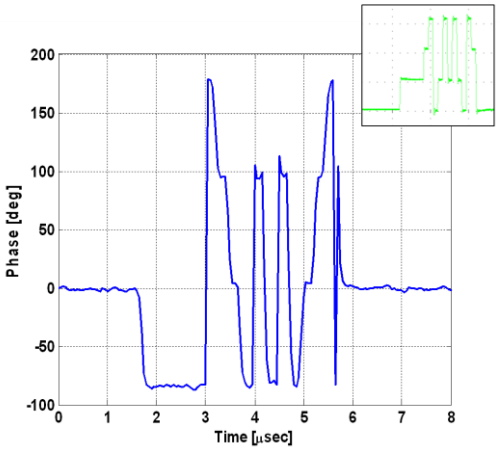

Figure 3.28 Phase transients of a polyphase Frank code with 16 sub-pulses

The obtained Autocorrelation Function (AF) of the acquired RF phase modulated pulse is shown in Figure 3.29. The trace is compared with the AF of 4μs pulse without modulation (red line), and with the simulated AF of the Frank code (inset). Frank Codes provide very good resistance to Doppler shift, in contrast to Bi-phase coded pulses where the main lobe amplitudes reduces while increasing the Doppler shifts. The compression factor is set to M^2 ($\Delta R=c\backslash 2BM^2$). Moreover the utilization of Pseudo Random Binary Sequence (PRBS) is also possible, together with a large range of other different codes. Therefore the effectiveness of the proposed photonic based solution for phase coded signal generation has been

presented and demonstrated, and results on compression effect have been analyzed.

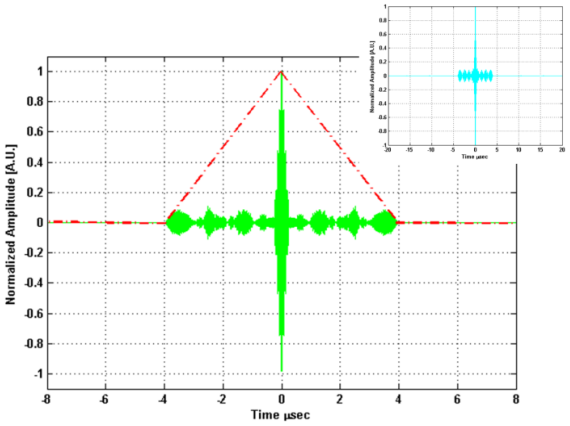

Figure 3.29 Autocorrelation function of the RF Frank code.

The frequency chirping is a phase-coding technique that induces a linear change in the radar carrier frequency along the pulse duration. In order to generate a linear frequency shift, a quadratic phase modulation must be applied to the carrier. The frequency deviation range is defined by following formula:

$$\Delta f = \frac{\Delta \phi}{\pi T_p} = \frac{\Delta V}{V_\pi T_p} \qquad (3.3.6)$$

where T_p is the pulse duration. In order to obtain a linear frequency chirp, in our experiment the DDS is set to generate a parabola. The parabolic phase modulation is reported in Figure 3.30(A) together with the pulsed amplitude modulation. The parabolic signal is designed to reach the maximum voltage variation (18V) within the radar pulse duration. Since the V_π of the employed Bias P port is 4.75V, a linear chirp of 3.8MHz is expected. From the graph, elongations are also evident at the phase jumps, introduced by the electrical amplifier. Figure 3.30 B) shows the waveform of the generated RF pulse, which appears to be amplitude-modulated by a chirped frequency. This undesired amplitude modulation is due to the non-ideal suppression of the unwanted optical carrier, that translates into an oscillating modulation. As stated by eq. (3.3.4), it is proportional to the cosine of a parabola. Figure 3.30(C) reports the traces of the frequency and amplitude transients, as acquired with the SSA. The measured frequency drift corresponds to the expected 3.8MHz and shows a linear trend. The elongations reported in Figure 3.30(A) are transferred on the frequency of the radar pulse

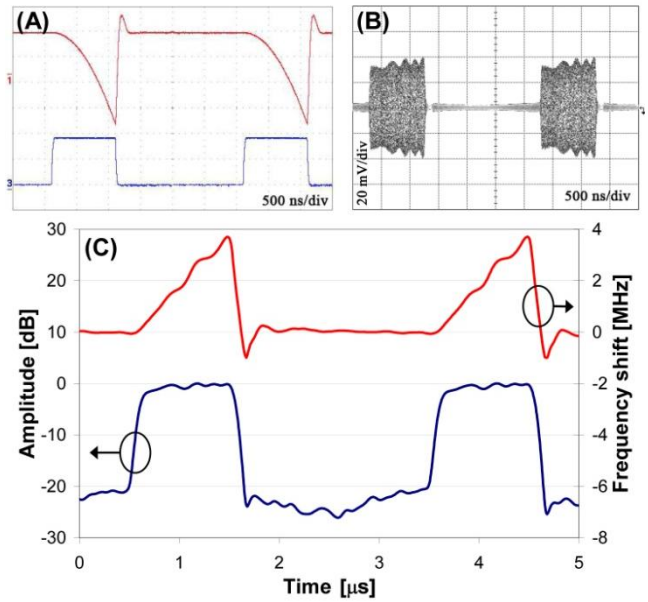

Figure 3.30 Optically generated RF pulses with linear frequency chirp.

The minor deviations from the linear behavior are probably caused by the narrow and non-regular bandwidth of the modulator Bias P (see Figure 3.23).

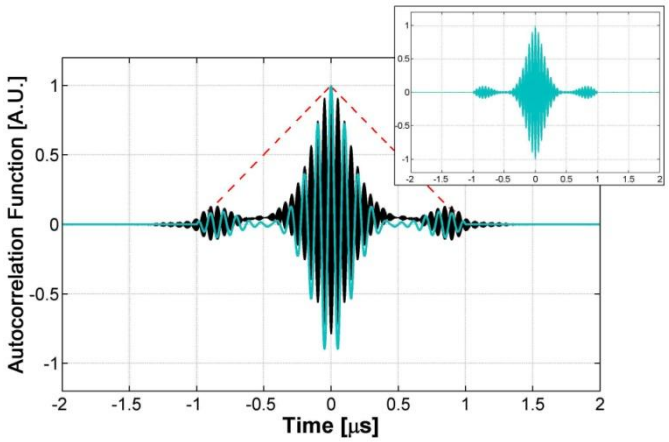

Figure 3.31 Autocorrelation function of the chirped pulses extracted from the real-time oscilloscope trace.

Figure 3.31 shows the autocorrelation function of the acquired chirped pulses, compared with the AF of a simulated ideal chirped pulse. The function calculated on the real data shows a good match with the simulated one, confirming once again the effectiveness of the proposed technique. In this case it is possible to estimate a resolution improvement up to 39m.

3.3.4. Conclusions

The experiments above demonstrate that the proposed architecture is capable of generating phase-modulated radar pulses at flexible carrier frequency exploiting a simple photonics-based setup. Besides the Barker codes and the linear frequency chirp, other pulse compression techniques would also be possible, as for example polyphase codes (Frank codes, complementary codes, or pseudo-random binary sequences applied to CW carriers), or nonlinear frequency modulations (e.g., raised cosine). Although the experimental realization has been limited to a small modulation bandwidth, larger bandwidths and phase changes can be readily achieved by designing specific I/Q modulators exploiting the current photonics technologies, thus realizing bandwidth broadening up to some GHz, further increasing the effectiveness of the proposed scheme. Moreover, the scheme can flexibly generate high-stability phase-modulated RF signals at very high carrier frequency, up to hundreds of GHz, with potentials also for THz and sub-THz signals generation, where the possibility of modulating the signal has not been extensively investigated yet. In conclusion, we have proposed a novel and practical scheme for the photonics-based generation of phase-modulated RF signals, targeted to the application in coherent radars with pulse compression techniques. The scheme is based on the exploitation of a commercial device, an optical I/Q modulator, in a non-conventional fashion, and its performance has been confirmed by experimental results. The high phase stability over a broad frequency range, and the wideband modulation capability of the proposed scheme, together with its compactness and reliability, could allow the realization of a new generation of high frequency fully digital phase coded radars, with wide application opportunities even in the related field of wireless communications.

CHAPTER 4

4. PHOTONIC ANALOG-TO-DIGITAL CONVERTER FOR WIDEBAND SIGNALS

The evolution of software defined radar (SDR) receivers strongly depends on the progress of high speed analog-to-digital converters (ADCs). For SDR systems the hardware components are embedded in a digital processor and the digitization process represents a critical issue. The key challenges for a high-speed ADC are the large input bandwidth (BW) and high sampling rates, the capability to receive small signals and reject larger interferers (measured as spurious-free dynamic range, SFDR), the sensitivity in term of signal-to-noise ratio (SNR), and the quality of the digitized signal in term of effective number of bits (ENOB). Today's best electronic ADCs show only few GHz of analog BW, with a sampling clock aperture jitter of hundreds of femtoseconds [58] which limits the development of ADCs with larger bandwidth and high ENOB.

In the following two paragraphs the photonic analog-to-digital converter based on time division demultiplexing and based on photonic assisted downconversion (both in downsampling working conditions) will be presented and discussed.

4.1. FOUR CHANNELS TIME INTERLEAVED ANALOG-TO-DIGITAL CONVERTER

The optical sampling can overcome the limitations faced by electronic ADCs [102], as demonstrated by several photonics-assisted ADCs proposed in the last decade, based on the electrical detection of modulated optical pulses with subsequent samples parallelization [65][66]. Most of these works resort to the concept of undersampling to acquire RF signals with BW up to few GHz but carrier frequency up to several tens of GHz. This approach well fits the radar applications, which are requiring bandpass signals with carriers in the SHF and EHF band (from 3GHz to 300GHz) to reduce the antenna dimension. The use of narrow-pulse mode-locked lasers (MLLs) with very low temporal jitter guarantees a precise sampling time and a digitized signal with low jitter-limited noise floor. The high electro-optical BW of the optical modulators can broaden the analog input BW of photonic-assisted ADCs, accepting RF signal with carriers up to tens of GHz. The sample parallelization by time- or wavelength-interleaving schemes enlarges the instantaneous BW (e.g., the maximum signal BW) of the photonic ADCs by exploiting a set of parallel low-speed high-precision electronic converters. The digitized signals can then be reconstructed by interleaving the parallel data arrays. But the interleaving operation can also produce spurious peaks due to the inequalities of gain and offset of the data arrays in the parallel channels, and to the non idealities of the parallelizing method as time skew and crosstalk [65]. While wavelength-interleaving is most sensible to the time skew, time-interleaving suffers the inter-channels crosstalk due to the limited extinction ratio (ER) of the optical switching matrix. Digital post-processing techniques are usually applied to minimize the effect of such spurious components and to maximize the precision of the photonic ADC [66].

4.1.1. Principle of operation

In the following section the basic principle of the photonic ADC based on the sample time-interleaving is presented, together with its main sources of non-linearity. The concept is based on the consideration that high-sampling-rate low-jitter optical pulses can largely overcome the performance of electronic ADCs. In fact, MLL with high pulse repetition rate (up to several GHz) and very low timing jitter (few fs) are easily available, and optical modulators with huge electro-optical bandwidth (up to a hundred GHz) allow the optical sampling of RF signals with large BW and carrier frequency in the millimeter waveband. Moreover, after the optical sampling process, a subsequent pulse switching is capable to split the

pulsed samples into several parallel flows at lower sample rate, allowing to exploit precise narrow-BW electronic ADCs. Then the digital samples are time-interleaved to re-establish the original data flow at the MLL sampling frequency.

The non idealities of the optical modulator represent the major source of system non-linearity. The most linear optical modulator is the Mach-Zehnder modulator (MZM), which nevertheless presents a squared cosine transfer function. With this kind of modulators, according to the modulation depth (the amplitude of the modulating signal with respect to the π-shift voltage of the MZM), the optical samples contain information on the input RF signal and on its higher order harmonics [66]. The finite ER of the optical switching matrix produces other spurious tones at frequencies given by:

$$f = \left(k\frac{F_S}{M} \pm \sum_n f'_{RFn} \right)\Bigg|_{k=1}^{M} \tag{4.1}$$

where F_S is the aggregate sampling rate, M is the number of parallel channels, and f'_{RFn} are the RF signal harmonics as detected by the undersampling process, $f'_{RFn} = nf_{RF} \bmod F_S/2$, with f_{RF} the signal frequency. As can be seen, this kind of distortion is a multiplicative noise, therefore the frequency of the spurious tones depends on both the sampling frequency and the RF signal harmonics [65][66]. Other spurious tones appear when the digital data arrays are recombined together. In fact, different insertion losses or photodiodes responsivity in the parallel channels cause a fixed-pattern additive noise. Since the pattern noise is independent of the RF signal, it causes spurious peaks at:

$$f = k\frac{F_S}{M}\Bigg|_{k=1}^{M} \tag{4.2}$$

In addition, the different gain and offset of the M ADCs also generate spurious tones at the same frequencies given by the equations (4.1) and (4.2) [103].

These sources of error reduce the sensitivity and dynamic range of the entire system.

4.1.2. Experiment set up

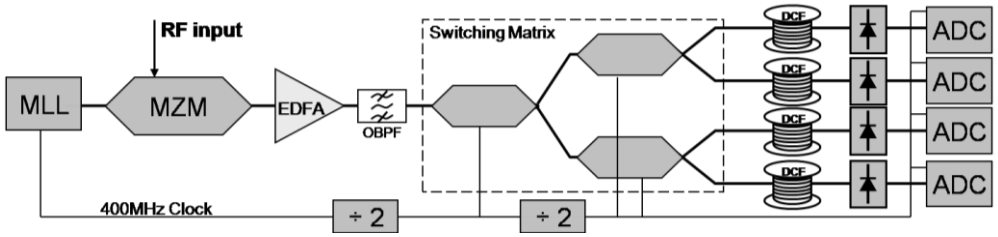

Figure 4.1 Photonic analog-to-digital converter

In Figure 4.1 the scheme of the photonic ADC is reported. A 400MHz repetition rate MLL generates 400fs-long optical pulses with a time jitter of about 10fs (measured for offset frequencies in the range 10kHz - 10MHz). The pulses sample the RF signal from a precise synthesizer (Agilent E8257D) in a standard 40GHz-bandwidth Mach-Zehnder modulator. To maximize the pulse modulation, the RF signal amplitude approaches the MZM V_π of 5V. An Erbium-doped fiber amplifier (EDFA) with 27dBm output power, followed by a 9nm-bandwidth optical band-pass filter (OBPF), boosts the signal before the time domain parallelization. This is done exploiting an integrated 1x4 LiNbO3 switching matrix, which consists of three dual-output MZMs (D-MZMs) in cascaded configuration. Each D-MZM is provided with an electrode precisely controlling the 2x2 coupler at the end of the Mach-Zehnder interferometer, thus maximizing the switching ER and reducing the crosstalk between the four outputs. An ER >25dB is guaranteed on all the output ports. The switching matrix is driven by two signals at 100 and 200MHz, directly derived from the laser clock and amplified to match the D-MZMs V_π. The parallelized optical pulses are then broadened with four spools of dispersion compensating fiber (DCF) with a chromatic dispersion of 300ps/nm, and photodetected with 2GHz-bandwidth photodiodes. The pulse broadening reduces the peak power and allows the photodiodes to work in their linear regime. No electrical amplifiers are used before the ADCs. Finally, the modulated pulses are quantized by means of four 100MSample/s 14-bit ADCs (National Instruments PXIe5122) synchronized with the pulse peaks.

4.1.3. Results

The performance of the photonic ADC is tested by applying single-tone signals at different frequencies. The synthesizer is set to generate carriers at 9.92GHz, 25.02GHz and 39.82GHz. Figure 4.2(left), Figure 4.4(left) and Figure 4.6(left) shows the fast Fourier transform (FFT) of both the acquired signals (with 4x10000 points) without post-processing algorithms. The tone at 9.92GHz appears aliased

at 80MHz, while the tones at 25.02GHz and 39.82GHz are aliased at 180MHz. The noise floor appears at clearly different levels in the graphs, and this is due to the increasing influence of the sampling jitter in the digitization of signals at increasing frequency. Other broadband noise sources as the thermal noise do not depend on signal frequency, so the effect of MLL sampling jitter is clearly predominant in the noise floor. In both the spectra, the high spurious peaks limit the dynamic range of the acquired signals. As discussed in section II, the peaks at 100MHz and 200MHz are due to the inequalities in the four parallel channels. The remaining spurious tones are related to the higher harmonics of the modulator, and to the inter-channel crosstalk due to the limited ER of the demultiplexer [65].

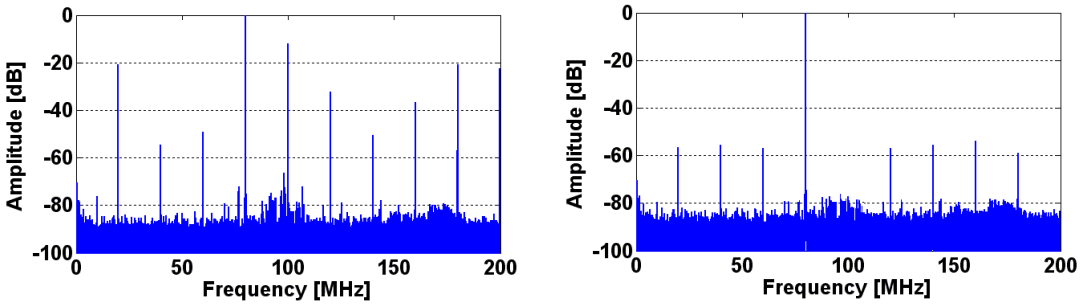

Figure 4.2 FFT of the interleaved sampled signals (9.92GHz) before (left) and after (right) post-processing.

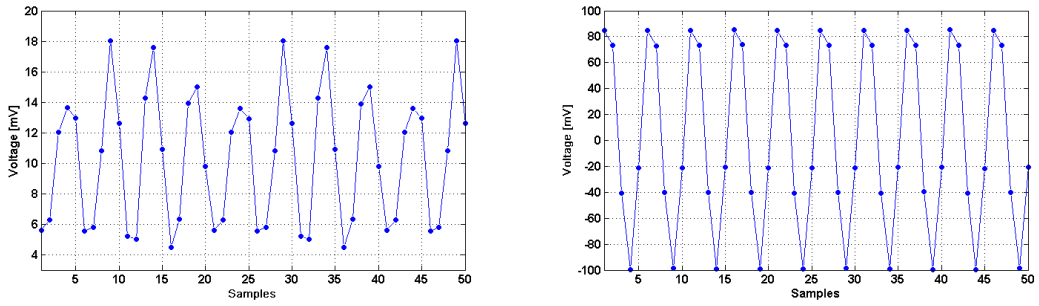

Figure 4.3 Time domain representation of the four interleav channels (9.92GHz) before (left) and after (right) post-processing.

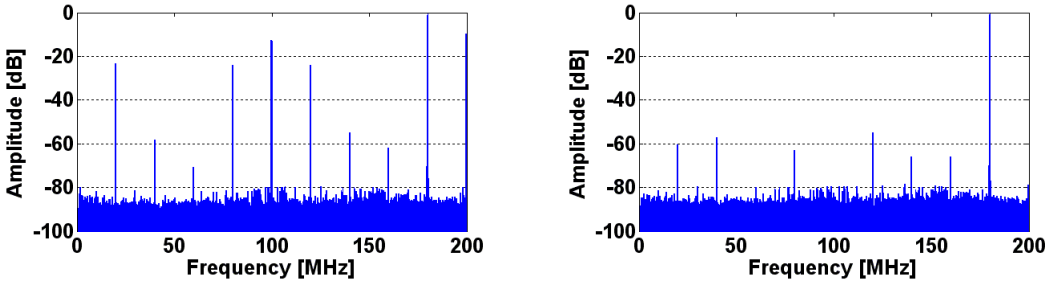

Figure 4.4 FFT of the interleaved sampled signals (25.02GHz) before (left) and after (right) post-processing.

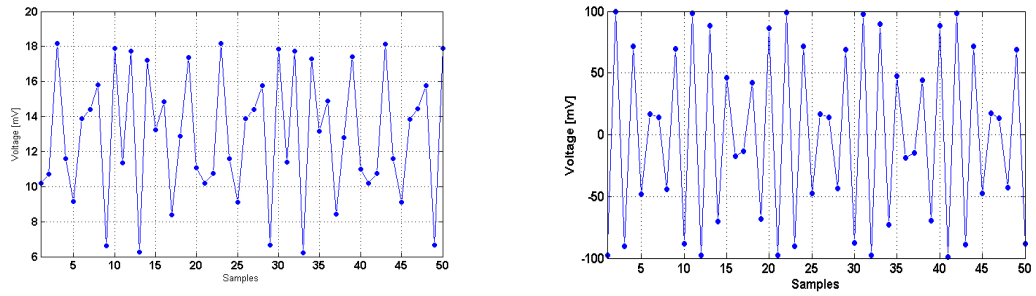

Figure 4.5 Time domain representation of the four interleav channels (25.02GHz) before (left) and after (right) post-processing.

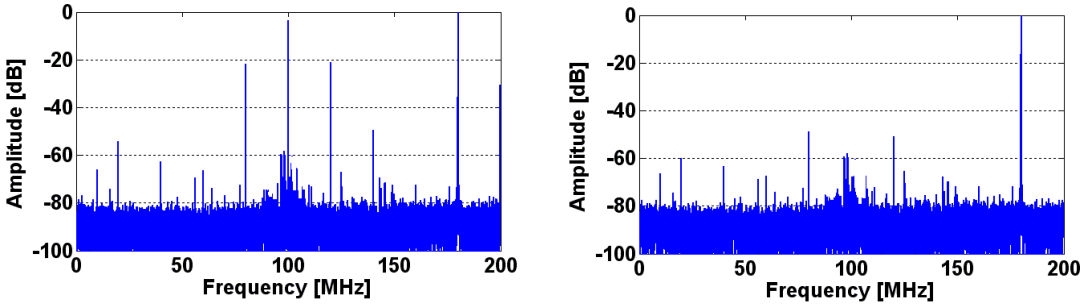

Figure 4.6 FFT of the interleaved sampled signals (39.82GHz) before (left) and after (right) post-processing.

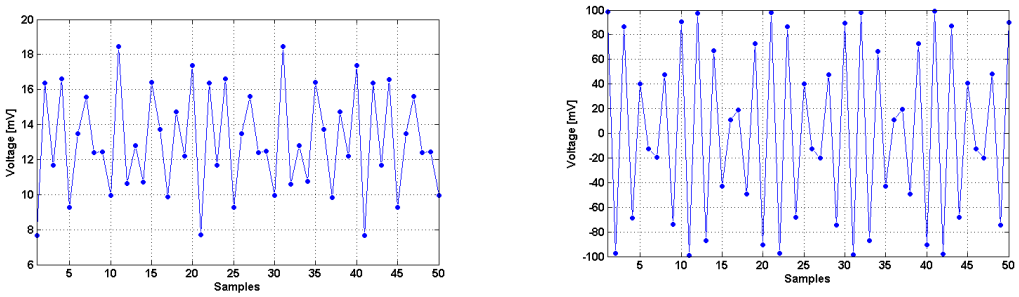

Figure 4.7 Time domain representation of the four interleav channels (39.82GHz) before (left) and after (right) post-processing.

In order to minimize the effects of the spurious peaks, a real-time post-processing algorithm is implemented. The algorithm compensates for the MZM higher harmonics through a digital linearization of the modulator transfer function [66]. On the other hand, channels inequalities due to different offsets and gains are equalized in the time domain comparing the modulation amplitudes and the mean values of each channel. In Figure 4.2(right), Figure 4.4(right) and Figure 4.6(right) the results of the post-processing algorithm are presented. The algorithms don't change the noise floors, while the spurious peaks drastically decrease, showing enhanced performance in term of SFDR. In Figure 4.3, Figure 4.5 and Figure 4.7 are also reported the time domain representation of the raw interleaved data (left) and the equalized sginals (right) for the 9.92GHz, 25.02GHz, and 39.82GHz, respectively.

In Figure 4.8 a particular of the extended so-called "Walden plot" [104] is shown, where it is possible to compare the performance in term of analog bandwidth and precision of the best electrical ADCs, and of the system proposed here. The theoretical upper bounds for sampling systems with an aperture jitter of 10fs is also reported. Since each measure in our experiment lasts 100μs (40k points at 400MS/s), the jitter of the sampling MLL that affects the measures must be calculated for offset frequency from 10kHz on, and is equal to about 10fs (9.87fs). Our system reaches an ENOB of 7.4, 7.1, and 7.0 for 9.92GHz, 25.02GHz, and 39.82GHz, respectively, with an instantaneous bandwidth of 200MHz. As can be seen from Figure 4.8, the proposed photonic ADC performs significantly better than the reported electrical ADCs.

It is possible to see that at 40GHz the system performance is close to the theoretical upper bound given by the aperture jitter of 10fs, while it moves away from that limit for lower signal frequency. The upper bound given by the time jitter is relative to a wideband ADC, while our system operates in undersampling mode. Nevertheless, considering only the noise due to the aperture jitter (i.e.,

neglecting the spurious tones as well as other noise sources), the two approaches become comparable.

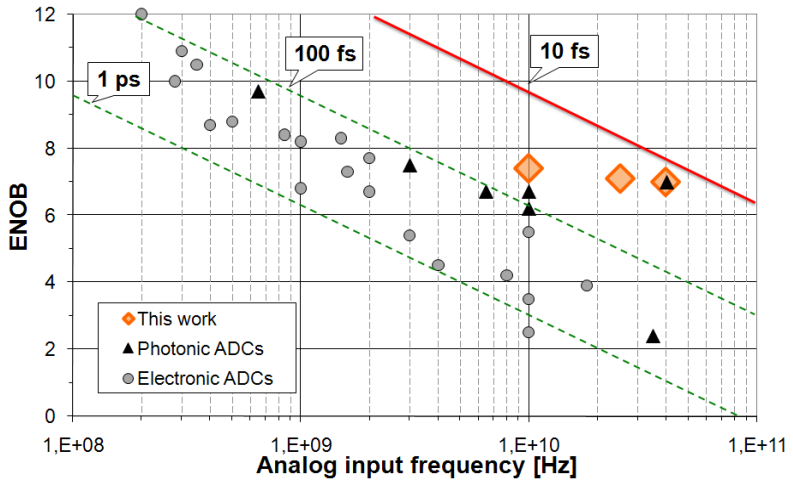

Figure 4.8 Particular of the "Walden plot"

As can be seen from the FFT in Figure 4.2 and Figure 4.6, while the SFDR remains almost constant with frequency, the noise floor at 39.82GHz is higher than that at 9.92GHz. This means that at lower frequency the system ENOB is limited by the spurious peaks, while at higher frequency it is mostly limited by the time jitter of the MLL, since the spurious tones become comparable with the noise floor. A strong improvement in the system performance could be reached increasing the instantaneous bandwidth of the ADC by increasing the aggregate sampling rate [105].

Therefore a MLL at higher sampling rate can be used with a greater number of parallel channels. Increasing the number of parallel channels induces further spurious tones in the FFT of the digitized signal, but the time duration of the acquisition process remains unchanged. So the laser phase noise must be integrated in the same offset frequency interval, leading to the same time jitter and noise floor. In order to demonstrate this, results considering one, two or four channels are presented in Figure 4.9 left and right. The ENOB is calculated both considering (SINAD) and neglecting (SNR) the spurious tones.

Using only one channel, corresponding to the Nyquist BW of 50MHz, the spurious tones due to the interleaving are not present, and the ENOB is maximized. On the other hand, when two channels are used (corresponding to the Nyquist BW of 100MHz), the appearing of the interleaving spurious peaks degrades the ENOB.

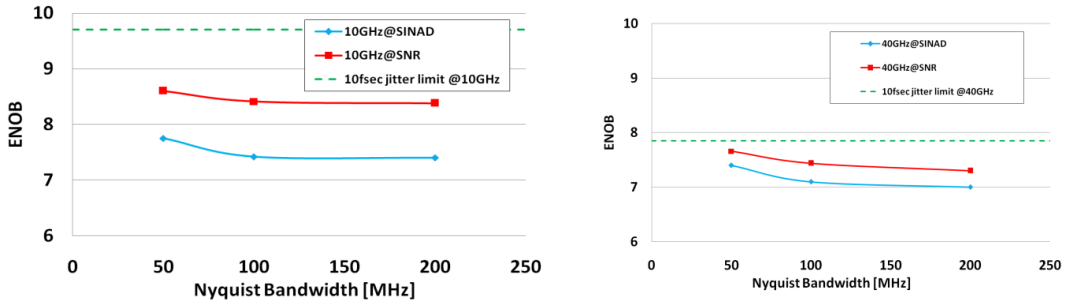

Figure 4.9 ENOB calculated considering 1-2-4 interleaved channels. 10GHz (left), 40GHz (right).

Nevertheless considering four interleaved channels (with Nyquist BW of 200MHz) the appearing of multiple spurious tones does not further degrade the system ENOB, although reaching broadband instantaneous BW, as explained above [104]. Further system improvements could be achieved by increasing the extinction ratio of the switching matrix, for example by means of an additional MZM on each of its output. Moreover, resorting to a differential detection would further improve the behavior of the photonic ADC in terms of both SNR and SFDR.

4.1.4. Conclusions

A photonic-assisted ADC with four time-interleaved channels has been presented, which can fully exploit the low jitter of the optical sampling technique avoiding the time skew issues. The proposed photonic ADC has been tested with RF signals over a large frequency range, demonstrating a state-of-the-art precision >7bit for input signals up to 40GHz and bandwidth up to 200MHz. The results show that the scheme is fundamentally limited by the sampling jitter and it approaches the theoretical limits for the considered signal frequencies. Further improving the ER of the switching matrix, and making use of a differential detection, would increase the system precision pushing it even closer to the theoretical limits imposed by the MLL timing jitter. The sampling scheme can be easily scaled to larger signal BW with the current technologies with minimal resolution degradation, and can therefore candidate as a promising flexible acquisition system for software defined radio applications.

CHAPTER 5

5. PHOTONIC WIDEBAND UP\DOWN CONVERTER

The generation of ultra-stable RF signals from UHF to MMB is made possible by resorting to photonic technologies [106]. The heterodyning of modes of a MLL generates a frequency comb of phase-locked RF oscillations that can be employed as carrier signals over different frequency bands. The timing jitter of a MLL can reach values as low as few fs and, since the phase noise of the *N*-th mode in the electrical spectrum of a MLL scales as N^2, all the generated carriers are affected by the same low timing jitter [107].

5.1.1. Principle of operation and experimental set up

Figure 5.1 shows the scheme of principle of the transceiver. It is composed of a MLL, cascaded with a MZM and a photodiode. The structure is replicated twice to obtain both a transmitter and a receiver in the same module, sharing the same MLL.

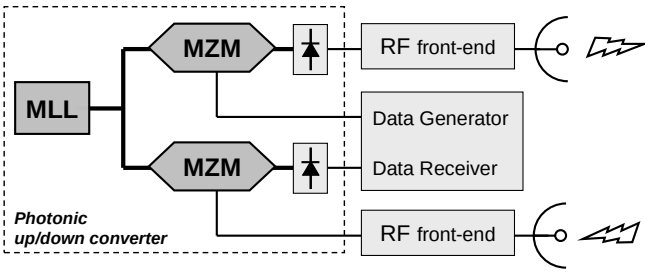

Figure 5.1 Scheme of principle of the transceiver

If a modulation signal at frequency fs is applied to the output of a MLL, an optical DSB-modulated signal is obtained: the signal spectrum is replicated as an upper- and lower-side band (USB and LSB, respectively) around every line in the MLL spectrum. When this comb of optical channels is fed into the photodiode, the heterodyning of all the components produces an electrical spectrum in which the signal is replicated every fs+N$f$rep, as an USB, and every fs-N$f$rep, as a LSB, whereas $f$rep is the MLL repetition frequency, and N is a non-negative integer. This way, a signal generated at a low intermediate frequency (IF) can be up-converted to a carrier frequency at IF+N$f$rep to be transmitted, even in multiple frequency bands, and a signal received at that frequency can be down-converted back to its IF. An electronic front-end between the photonic up/down-converter and the antenna provides the necessary filtering and amplification operations.

In the experimental activity an active, harmonic, 10GHz-repetition rate MLL is employed, together with a 40GHz MZM and a 40GHz linear photoreceiver with a trans-impedence amplifier (TIA). The average output power of the MLL is 5dBm. An Agilent PSG-E8267D vector signal generator (VSG) is employed to obtain the RF UWB signals around the IF and a 40GHz bandwidth MZM driver amplifies them, as shown inFigure 5.2.

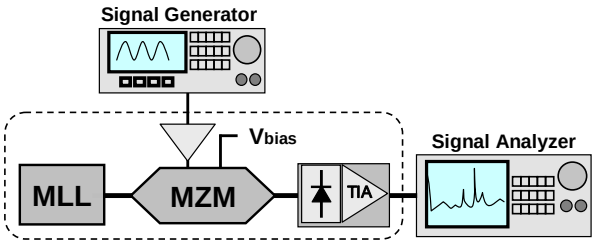

Figure 5.2 Experimental Setup

The MZM RF input power is around 5dBm. Each sub-channel consists in 52 OFDM sub-carriers, carrying 54Mbps over a 64-QAM pattern and occupying 22MHz of bandwidth, according to the 802.11g standard. Then, 22 of these sub-channels are combined to obtain a single UWB channel with a bandwidth of 484MHz and a data rate around 1.2Gbps. In the experiment, 8 adjacent UWB channels are generated, and their IFs are chosen between DC and 5GHz, viz. the half of the MLL repetition frequency $f$rep. Thus, the symmetry of the DSB-modulated optical spectrum is ensured, and interferences due to folded replicas of the beating channels are avoided.

The produced electrical spectrum is depicted in Figure 5.3. The UWB RF signal spectra, generated by the VSG around IF, are replicated as USB and LSB, around every harmonic of the MLL, and are symmetrically spaced by IF from the respective MLL line. The first two harmonics of the MLL are depicted at 10GHz

and 20GHz, and the groups of 8 adjacent 484MHz-wide channels are clearly visible as well.

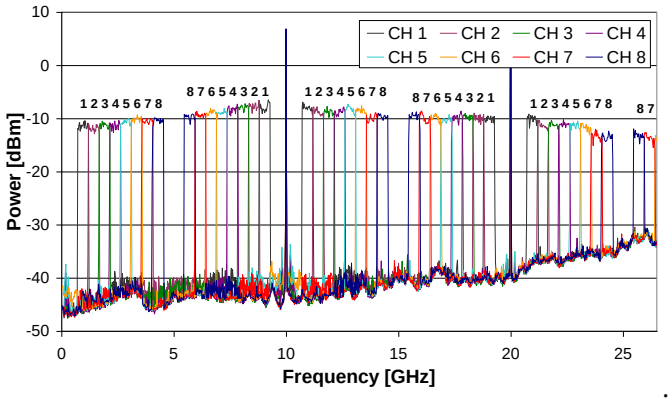

Figure 5.3 Electrical spectrum of the transmitted signal

5.1.2. Results

The performance of the presented system has been evaluated by measuring the EVM of the central 22MHz sub-channel of every up-converted and down-converted 484MHz channel, receiving the signals with a 26.5GHz bandwidth Vector Signal Analyzer (VSA) Agilent MXA-N9060A. Figure 5.4 depicts the EVM of three channels at IF 0.9GHz, 3.32GHz, and 4.29GHz, i.e. channels 1, 6, and 8 respectively. The channels at IF are directly generated by the VSG. These channels are then up-converted with the presented system as 10GHz USB replicas (10.9GHz, 13.32GHz, and 14.32GHz respectively) and as 30GHz LSB replicas (in this case, due to the VSA bandwidth limitations, only channels 6 and 8 are reported, at 25.7GHz and 26.49GHz respectively). In order to compare the photonic up-converter with the electronic RF generation, Figure 5.4 reports also the EVM of the same signals directly generated at higher frequencies

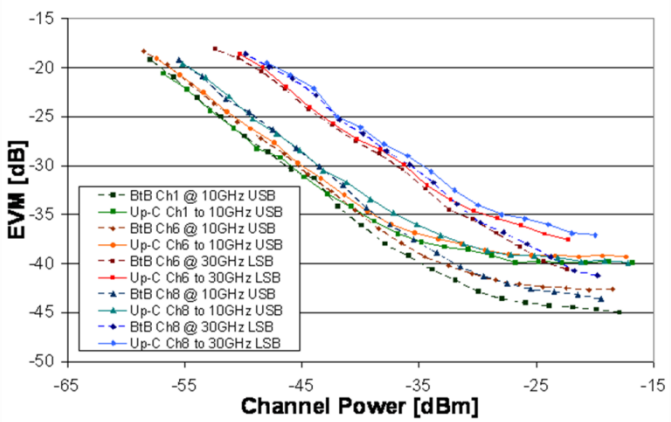

Figure 5.4 EVM of channels 1, 6, and 8 up-converted to two different frequencies

As shown by the EVM curves, the performance difference between the two methods is negligible, except for the different floor level for higher power values. This is probably to be ascribed to the saturation of the TIA at the VSA input and to the time/amplitude jitter of the laser. Actually, this difference does not represent an issue, because the 802.11g standard defines the error-free working region for power values corresponding to EVM < -25dB. The couples of curves at different frequency also present a power offset, i.e. increasing the frequency, the power needed to obtain a certain EVM also increases. This is only due to the different sensitivity of the VSA, which is clearly visible form the noise floor in Figure 5.3. The performances of the photonic down-conversion are also evaluated, measuring the EVM. Figure 5.5 reports the EVM values for channels 1, 6, and 8 optically down-converted (Down-C) to IF from their 10GHz USB and 30GHz LSB frequencies, compared with the channels generated at IF. Here again, except for the higher floor of the optically down-converted channels, the Down-C EVM curves show excellent performance.

Since the system is designed to occupy the whole available bandwidth, second and third order distortions (MZM non-linearity, higher order beatings) may cause cross-talk or self-interference on the up- or down-converted signals. To better evaluate the system behaviour in this eventuality, a channel centered on 3.333GHz has been up-converted to 13.333GHz. This represents the worst case, because such a channel overlaps with the third harmonic of the 20GHz LSB, as well as with all the beatings given by the N-th laser mode USB and (N+2)-th mode LSB in the optical spectrum.

Figure 5.6 reports the EVM curve of the Up-C channel, compared with a detuned channel which does not suffer from distortion. Though the distorted channel presents a higher floor, the power penalty for lower EVM values is again

negligible. Moreover, the inset in Figure 5.6 shows the high difference between the channel power level and the noise and distortions level.

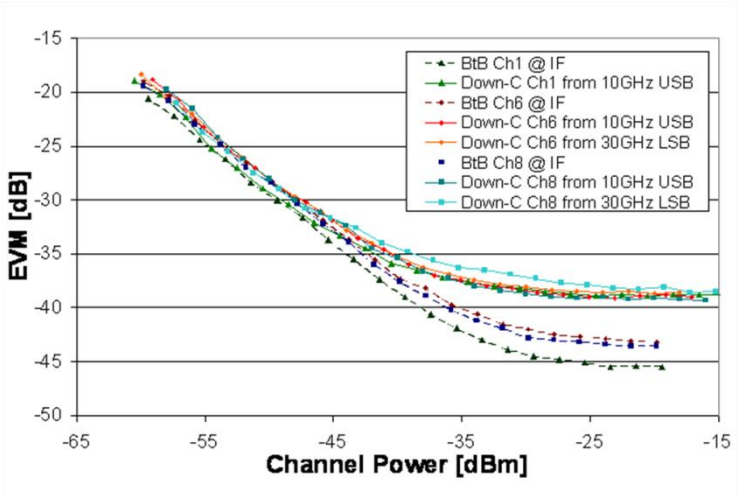

Figure 5.5 EVM of channels 1, 6, and 8 generated at IF (BtB), and of the same channels down-converted back to IF (Down-C)

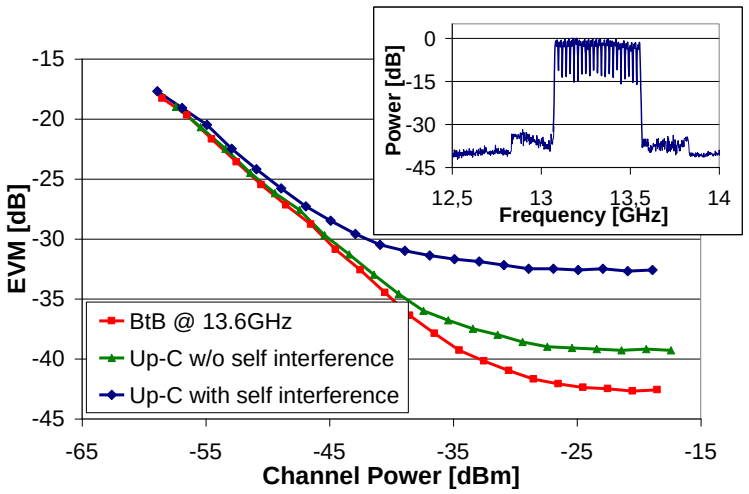

Figure 5.6 EVM for the channel with worst case self-interference

The power penalty is explicitly represented in Figure 5.7.

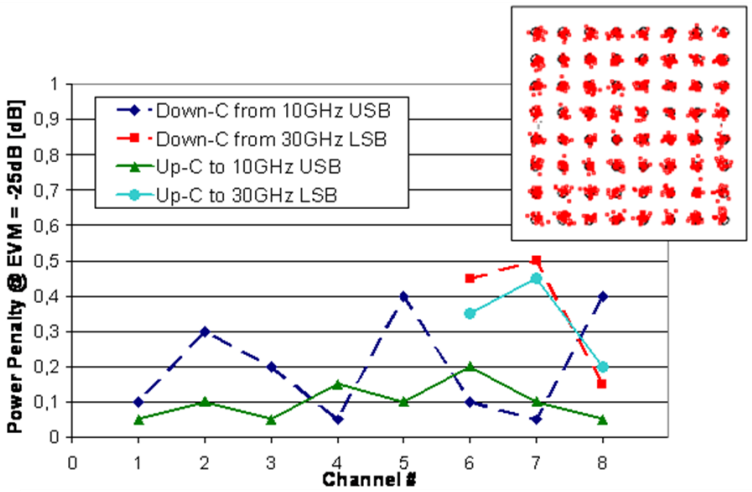

Figure 5.7 Power penalty in up- and down-conversion for every channel up- or down-converted to or from different frequencies

In compliance with the 802.11g standard, the penalty is measured as the difference between the minimum power needed to obtain EVM = -25dB for a given channel directly generated at its carrier frequency, and the minimum power to obtain the same EVM for the corresponding optically up-converted (or down-converted) channel. The penalty is reported for each channel from 1 to 8, measured on the USBs of the 10GHz MLL line (from 10.9GHz to 14.29GHz). To evaluate the performance of the system at the highest possible frequency, we also measured penalties for some channels from the 30GHz-line sidebands. Here again, due to the VSA bandwidth limitations, only the three lowest frequency LSB channels could be analyzed (from 25.7GHz to 26.5GHz). The measured power penalty values are negligible both in up- and down-conversion, never exceeding 0.5dB.Finally, Figure 5.8 reports the penalty on the EVM for a received channel power of -25dBm, in the case of all the eight 10GHz-USB channels and three 30GHz-LSB channels. This power value has been chosen because, for that power, all the measured EVM curves have already entered their floor region. In any of the analyzed cases, the EVM penalty varies in a maximum range of 2dB, and turns to be smaller for Up-C channels, at any considered frequency. This can be explained considering that, in the Down-C, the signal to be down-converted is first electronically up-converted inside the VSG and this slightly lowers the RF signal quality with respect to the reference signal generated at low frequency.

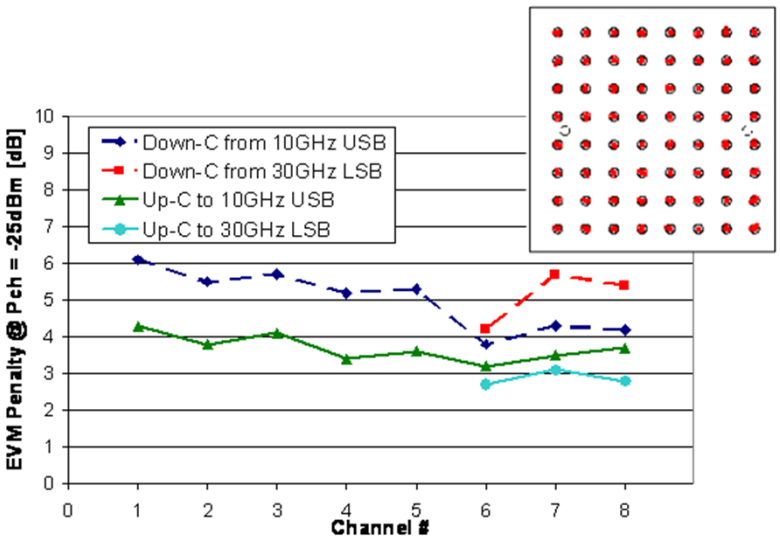

Figure 5.8 EVM penalty measured for a received power of -25dBm, in up- and down-conversion for every channel up- or down-converted to or from different frequencies

5.1.3. Conclusions

In this section the high performance and negligible power penalty of an UWB photonic-assisted system for simultaneous multi-band up- or down-conversion of wireless signals has been presented and demostrated. The scheme is easily based on the modulation of the laser modes of a MLL in a MZM, followed by the heterodyning of the optical signal in a photodiode. The large optical spectrum of the MLL and the wide electro-optical bandwidth of the MZM and of the photodiode allow using the scheme as an up- or down-converter of RF signals up to the MMB. The presented system has been tested up to 26.5GHz, with a maximum power penalty lower than 0.5dB with respect to the signal generated directly at high frequencies (for Up-C) or low frequency (for Down-C), keeping high the quality of the signals both in transmission and reception. Since the very same device can act both as an up- and down-converter, two of them can form a two-branched complete transceiver, sharing a single MLL. The photonic system can easily work at frequencies higher than the tested 26.5GHz, employing a larger bandwidth photoreceiver (100GHz photodiodes are commercially available) and E/O modulator, and is particularly suitable for the implementation of a multi-band, multi-protocol transceiver for future mobile networks. Since it is based only on a MLL, a MZM, and a photoreceiver, the presented architecture is very compact, suitable for the integration, and apt to be employed in base stations as well as in mobile devices.

CHAPTER 6

6. RADAR PROTOTYPE

The main objective of this prototype is to implement a fully digital radar transceiver with further experimental validation and testing.

6.1.1. System requirements

The study has been focused on a pulsed radar system at X band (about 10GHz) for the detection of civil aerial target in a range up to tens of kilometres. The reference scenario allows us to simplify the radar signal processing neglecting the ground clutter contribution. A monostatic approach has been chosen in order to simplify the realization of both the prototype and signal processing chain. Reffering to [108] the main characteristics are listed in the following table:

Parameters	Value
Radar Cross Section	100 m^2
Carrier Frequency	X-Band (about 10 GHz)
Pulse Width	1 μs
Range Resolution	150 m
Pulse Repetition Interval	1 ms
Maximum Observable Range	10 km
Minimum Observable Range	1.5 km

Antenna Gain	30 dB
Integrated Pulses	40-100
Transmitted Peak Power	20 – 40 Watt
False Alarm Probability	10e-6
Detection Probability	0.8

Table 6.1 Prototype system requirements

6.1.2. Photonic transceiver

In Figure 6.1 Photonic radar front end electrical scheme of the transceiver will be presented. Then some parameters are detailed in Table 6.2 while photographs of the assembly are shown in Figure 6.2 and Figure 6.3.

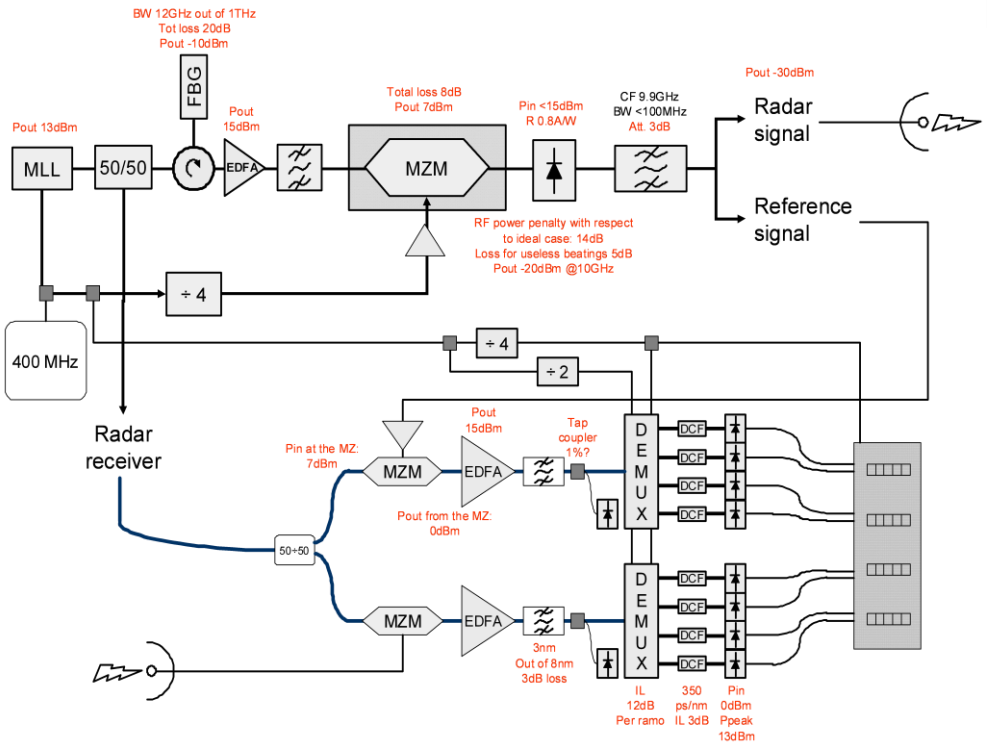

Figure 6.1 Photonic radar front end electrical scheme

Figure 6.2 Photonic radar transmitter

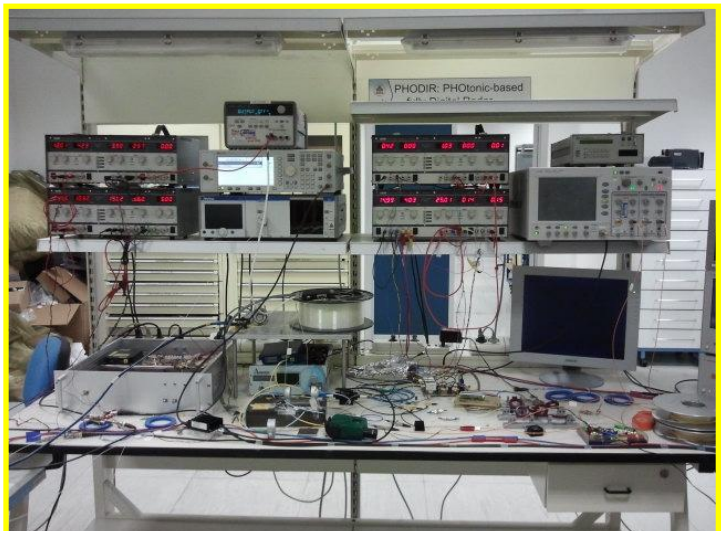

Figure 6.3 Photonic radar receiver

MZM Vpi [V]	**5**
MZM bandwidth [GHz]	20
Laser Jitter [fsec]	10
Laser RIN [%]	0.008
Laser Pulse width [fsec]	300
Laser Frequency [MHz]	400
Max MZM Bias Voltage [V]	2.5
PD max power [dBm]	16
PD bandwidth [GHz]	2

Table 6.2 Photonic radar receiver

6.1.3. Transceiver front-end

Figure 6.4 Radar Front end electrical scheme presents the electrica schme of the amplification RF stages for the transmitter and the receiver.

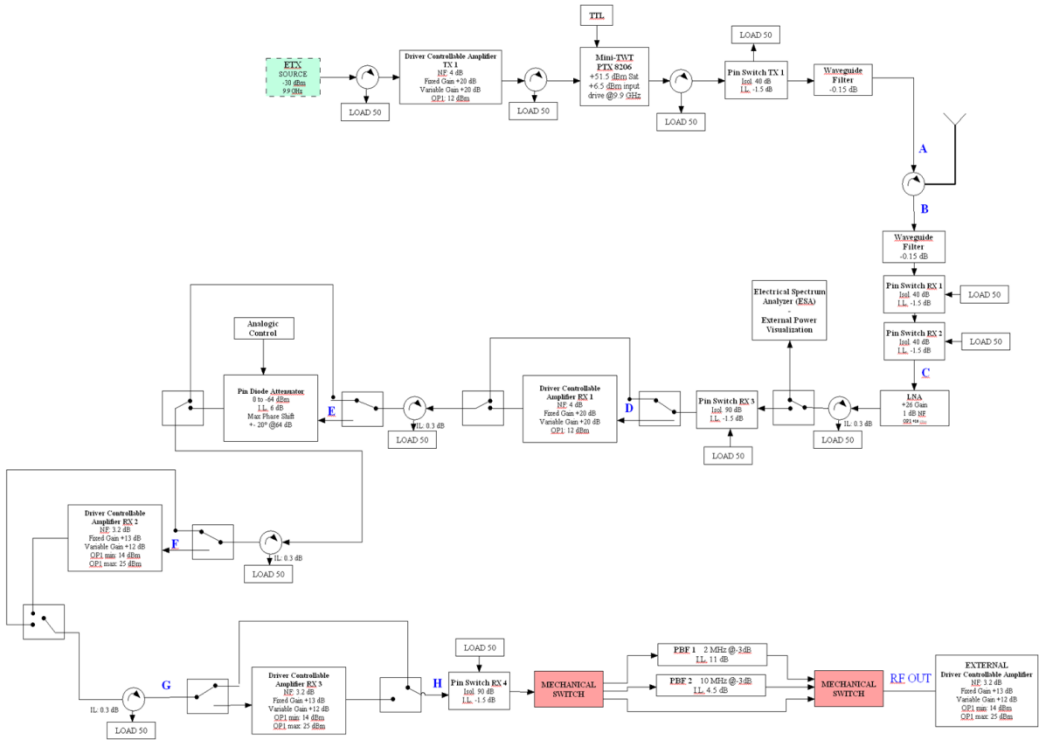

Figure 6.4 Radar Front end electrical scheme

The total transmission amplification has been divided in two different section: the driver pre amplifier and the high power amplifier for a total amplification gain of about 80 dB in order to achieve a +50 dBm transmitted signal with an external source of -30 dBm achieved via electro optical devices. The received chain is composed by a sequence of Pin Diode Switch attenuator, Low Noise Amplifier and Gain Controllable amplifier. Furthermore a Sensitive Time Control could be added in the chain to eliminate the signal variation due to the received signal dynamic. As said before a switchable filter bank has been introduced to increase the receiver sensibility. The estimation of the maximum and minimum received power at the antenna (point B in Figure 6.4) has been calculated under these operative conditions: For the maximum received power

$$P_T = [15,30] Watt,\ G_{Antenna} = 30dB,\ Range_{\min} = 400m\ ,\sigma = 100m^2\ ,Loss = 7.1dB$$

$$P_{RX\max} = [-83, -80]\, dB$$

For the minimum received power

$$P_T = [15, 30]\, Watt,\ G_{Antenna} = 30 dB,\ Range_{\max} = 10 km\ , \sigma = 100 m^2\ , Loss = 7.1 dB$$

$$P_{RX\max} = [-139, -136]\, dB$$

In the following consideration we refer to a received power in the range:

$$\boxed{P_{RX} = [-109, -50]\, dBm}$$

The LNA (point C in Figure 6.4) input power has been calculated considering the characteristics of the amplifier (fixed gain 26 dB and $OP1_{dB}$ 10 dBm) and a cautelative 7 dB of losses as well as in the transmitter stage (cable between mini TWT and circulator). Assuming this value the linearity of the 1st stage amplifier is guaranteed. The power outupt of the LNA is in the range between $P_{RX} = [-90, -31]\, dBm$.

Following the scheme the power input at the 1st Driver Controllable Amplifier RX1 we consider a 0.3 dB loss due to the isolator, therefore the power input in the point D of the Figure 6.4 is:

$$\boxed{P_{RX} = [-90.3, -31.3]\, dBm}$$

For the selected driver amplifier we have these characteristics:

Gain max	40 dB	OP1	12 dBm
Gain min	20 dB	OP1	-8 dBm

For both the considered values (full gain and minimum gain) we don't have any problem in term of linearity considering the $OP1_{dB}$ of the amplifier.

The power input of the Sensitive Time Control could be calculated considering the full gain and the minimum gain cases of the before mentioned driver controllable amplifier RX1. Therefore in the point E of the Figure 6.4 considering a 0.3 dB of isolator loss we have a received power:

minimum gain case (20 dB)

$$P_{RX} = [-70.6, -11.6] dBm$$

maximum gain case (40 dB)

$$P_{RX} = [-50.6, +9.6] dBm$$

The attenuator STC block will be driven with an analogical voltage and has maximum input power of +10 dBm.

In the following for the estimation of the power range in the received chain (in particular with respect of the driver controllable amplifier RX2 RX3 and filter bank, point F and G and H in Figure 6.4) we consider two operative steps:

- **Sensitive Time Control ON**
- **Sensitive Time Control OFF**

Case Sensitive Time Control ON

For the estimation of the power in the point F of the chain we assume:

1. Driver Controllable Amplifier RX1 with minimum gain: 20 dB

$$P_{RX} = -70.6 - 0.3 = -70.9 dBm$$

2. Driver Controllable Amplifier RX1 with full gain: 40 dB

$$P_{RX} = -50.6 - 0.3 = -50.9 dBm$$

For the selected driver amplifier we have these characteristics:

Gain max	25 dB	OP1	25 dBm
Gain min	13 dB	OP1	14 dBm

So with the STC ON the estimated power input in to the driver controllable amplifier RX2 should not introduce problems of linearity for both the operative conditions.

For the power estimation at the point G we consider four different cases:

1. Driver Controllable Amplifier RX1 with minimum gain: 20 dB and Driver Controllable Amplifier RX2 with minimum gain: 13 dB.

$$P_{RX} = -70.9 + 13 - 0.3 = -58.2 dBm$$

2. Driver Controllable Amplifier RX1 with minimum gain: 40 dB and Driver Controllable Amplifier RX2 with minimum gain: 13 dB

$$P_{RX} = -50.9 + 13 - 0.3 = -38.2 dBm$$

3. Driver Controllable Amplifier RX1 with minimum gain: 20 dB and Driver Controllable Amplifier RX2 with minimum gain: 25 dB

$$P_{RX} = -70.9 + 25 - 0.3 = -46.2 dBm$$

4. Driver Controllable Amplifier RX1 with minimum gain: 40 dB and Driver Controllable Amplifier RX2 with minimum gain: 25 dB

$$P_{RX} = -50.9 + 25 - 0.3 = -26.2 dBm$$

For the selected driver amplifier we have these characteristics:

Gain max	25 dB	OP1	25 dBm
Gain min	13 dB	OP1	14 dBm

So with the STC ON the estimated power input in to the driver controllable amplifier RX3 (point G) should not introduce problems of linearity for both the operative conditions.

For the estimation of the filter bank power input (point H in Figure 6.4 which correspond to the output of the driver controllable amplifier RX3) we should consider eight different cases:

1. Driver Controllable Amplifier RX1 with minimum gain: 20 dB, Driver Controllable Amplifier RX2 with minimum gain: 13 dB and Driver Controllable Amplifier RX3 with minimum gain: 13 dB

$$P_{RX} = -70.9 + 13 - 0.3 + 13 = -45.2 dBm$$

2. Driver Controllable Amplifier RX1 with full gain: 40 dB, Driver Controllable Amplifier RX2 with minimum gain: 13 dB and Driver Controllable Amplifier RX3 with minimum gain: 13 dB

$$P_{RX} = -50.9 + 13 - 0.3 + 13 = -25.2 dBm$$

3. Driver Controllable Amplifier RX1 with minimum gain: 20 dB, Driver Controllable Amplifier RX2 with full gain: 25 dB and Driver Controllable Amplifier RX3 with minimum gain: 13 dB

$$P_{RX} = -70.9 + 25 - 0.3 + 13 = -33.2 dBm$$

4. Driver Controllable Amplifier RX1 with full gain: 40 dB, Driver Controllable Amplifier RX2 with full gain: 25 dB, Driver Controllable Amplifier RX3 with minimum gain: 13 dB

$$P_{RX} = -50.9 + 25 - 0.3 + 13 = -13.2 dBm$$

5. Driver Controllable Amplifier RX1 with minimum gain: 20 dB, Driver Controllable Amplifier RX2 with minimum gain: 13 dB and Driver Controllable Amplifier RX3 with full gain: 25 dB

$$P_{RX} = -70.9 + 13 - 0.3 + 25 = -33.2 dBm$$

6. Driver Controllable Amplifier RX1 with full gain: 40 dB, Driver Controllable Amplifier RX2 with minimum gain: 13 dB and Driver Controllable Amplifier RX3 with full gain: 25 dB

$$P_{RX} = -50.9 + 13 - 0.3 + 25 = -13.2 dBm$$

7. Driver Controllable Amplifier RX1 with minimum gain: 20 dB, Driver Controllable Amplifier RX2 with full gain: 25 dB, Driver Controllable Amplifier RX3 with full gain: 25 dB

$$P_{RX} = -70.9 + 25 - 0.3 + 20 = -21.2 dBm$$

8. Driver Controllable Amplifier RX1 with full gain: 40 dB , Driver Controllable Amplifier RX2 with full gain: 25 dB, and Driver Controllable Amplifier RX3 with full gain: 25 dB

$$P_{RX} = -50.9 + 25 - 0.3 + 25 = -1.2 dBm$$

The amplifier power values and the relative check on the amplifiers $OP1_{dB}$ are summarized in the following table:

	Driver Amplifier 1 Gain	***OP1 Driver Amplifier 2 check***	***Driver Amplifier 2 Gain***	***OP1 Driver Amplifier 3 check***	***Driver Amplifier 3 Gain***

	[dB]		*[dB]*		*[dB]*
	20	OK	13	OK	13
	40	OK	13	OK	13
	20	OK	25	OK	13
STC	40	OK	25	OK	13
ON	20	OK	13	OK	25
	40	OK	13	OK	25
	20	OK	25	OK	25
	40	OK	25	OK	25

Table 6.3 Amplification strategy and warning - STC ON

The maximum and minimum values are respectively -45.2 dBm and -1.2 dBm. Considering the filter bank we have a power range between:

- -45.2 dBm and -1.2 dBm (without filters)
- -56.2 dBm and -12.2 dBm (with PBF1 and IL of about 11 dB).

In this case in order to achieve an RF_OUT power of 10 dBm we assume an exteranl amplification stage with the following characteristics:

Gain max	25 dB	OP1	25 dBm
Gain min	13 dB	OP1	14 dBm

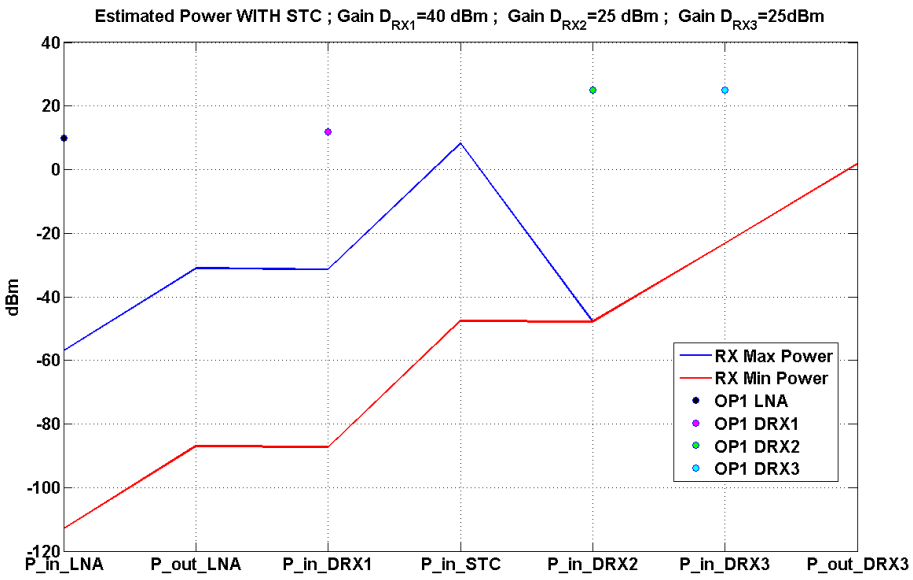

Figure 6.5 Example of Estimated power with Sensitive Time Control

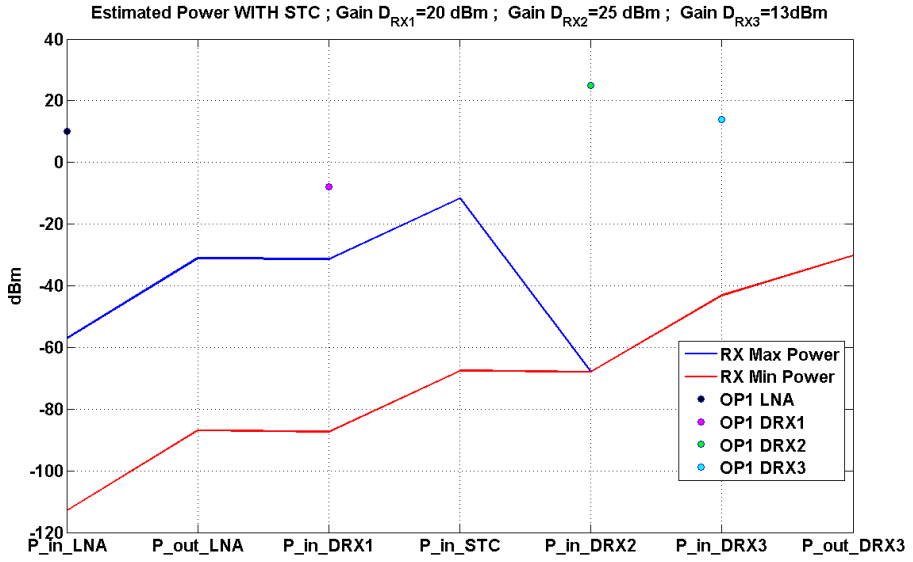

Figure 6.6 Example of Estimated power with Sensitive Time Control

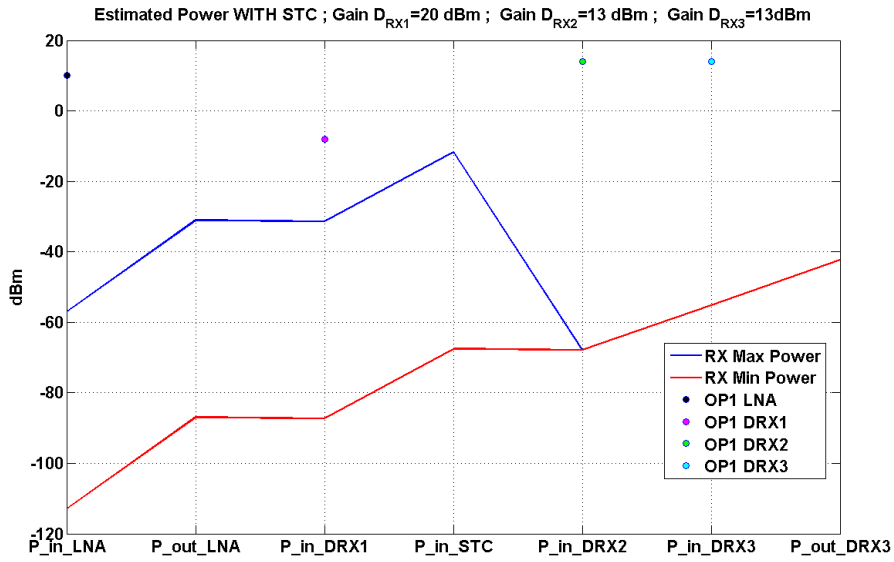

Figure 6.7 Example of Estimated power with Sensitive Time Control

Case Sensitive Time Control OFF

With the STC switched off we have:

1. Driver Controllable Amplifier RX1with minimum gain: 20 dB

$$P_{RX} = [-70.6, -11.6] - 0.3 = [-70.9, -11.9] dBm$$

2. Driver Controllable Amplifier RX1 with full gain: 40 dB

$$P_{RX} = [-50.6, +9.6] - 0.3 = [-50.3, +9.3] dBm$$

Referring to the "Driver Controllable Amplifier RX2

Gain max	25 dB	OP1	25 dBm
Gain min	13 dB	OP1	14 dBm

Without the STC the input power range and the gain of the driver amplifiers RX1 with the minimum gain we don't have problem at the driver controllable amplifier RX2 for both its minimum and maximum gain. On the other hand if we use the 1st stage at its maximum gain the power input value (about 10 dBm) at the driver amplifier RX2 (when it's used with minimum gain) are in the same region of the OP1dB (about 14 dBm). Under this assumption we can use the driver amplifier RX1 with lower gain.

At the input of the third driver controllable amplifier (point G in Figure 6.4) we have four different cases:

1. Driver Controllable Amplifier RX1 with minimum gain: 20 dB and Driver Controllable Amplifier RX2 with minimum gain: 13 dB

$$P_{RX} = [-90.3, -31.3] + 20 - 0.3 - 0.3 + 13 - 0.3 = [-58.2, 0.8]\, dBm$$

2. Driver Controllable Amplifier RX1 with full gain: 40 dB and Driver Controllable Amplifier RX2 with minimum gain: 13 dB

$$P_{RX} = [-90.3, -31.3] + 40 - 0.3 - 0.3 + 13 - 0.3 = [-38.2, 20.8]\, dBm$$

3. Driver Controllable Amplifier RX1 with minimum gain: 20 dB and Driver Controllable Amplifier RX2 with full gain: 25 dB

$$P_{RX} = [-90.3, -31.3] + 20 - 0.3 - 0.3 + 25 - 0.3 = [-46.2, 12.8]\, dBm$$

4. Driver Controllable Amplifier RX1 with full gain: 40 dB and Driver Controllable Amplifier RX2" with full gain: 25 dB

$$P_{RX} = [-90.3, -31.3] + 20 - 0.3 - 0.3 + 25 - 0.3 = [-26.2, 32.8]\, dBm$$

referring to the Driver Controllable Amplifier RX3 we obtain only two cases with the input power at the 3th driver lower than its $OP1_{dB}$. They are the case 1 and 3 where we use the Driver Controllable Amplifier RX1 at its minimum gain.

For the estimation of the power in the point H of the Figure 6.4 we have:

1. Driver Controllable Amplifier RX1 with minimum gain: 20 dB, Driver Controllable Amplifier RX2 with minimum gain: 13 dB and Driver Controllable Amplifier RX3 with minimum gain: 13 dB

$$P_{RX} = [-90.3, -31.3] + 20 - 0.3 - 0.3 + 13 - 0.3 + 13 = [-45.2, 13.8]\, dBm$$

2. Driver Controllable Amplifier RX1" with full gain: 40 dB, Driver Controllable Amplifier RX2 with minimum gain: 13 dB and Driver Controllable Amplifier RX3 with minimum gain: 13 dB

$$P_{RX} = [-90.3, -31.3] + 40 - 0.3 - 0.3 + 13 - 0.3 + 13 = [-25.2, 33.8]\, dBm$$

3. Driver Controllable Amplifier RX1 with minimum gain: 20 dB, Driver Controllable Amplifier RX2 with full gain: 25 dB, Driver Controllable Amplifier RX3 with minimum gain: 13 dB

$$P_{RX} = [-90.3, -31.3] + 20 - 0.3 - 0.3 + 25 - 0.3 + 13 = [-33.2, 25.8]\, dBm$$

4. Driver Controllable Amplifier RX1 with full gain: 40 dB, Driver Controllable Amplifier RX2 with full gain: 25 dB, Driver Controllable Amplifier RX3 with minimum gain: 13 dB

$$P_{RX} = [-90.3, -31.3] + 20 - 0.3 - 0.3 + 25 - 0.3 + 13 = [-13.2, 45.8]\, dBm$$

5. Driver Controllable Amplifier RX1 with minimum gain: 20 dB, Driver Controllable Amplifier RX2 with minimum gain: 13 dB and Driver Controllable Amplifier RX3 with full gain: 25 dB

$$P_{RX} = [-90.3, -31.3] + 20 - 0.3 - 0.3 + 13 - 0.3 + 25 = [-33.2, 25.8]\, dBm$$

6. Driver Controllable Amplifier RX1 with full gain: 40 dB, Driver Controllable Amplifier RX2 with minimum gain: 13 dB and Driver Controllable Amplifier RX3 with full gain: 25 dB

$$P_{RX} = [-90.3, -31.3] + 40 - 0.3 - 0.3 + 13 - 0.3 + 25 = [-13.2, 45.8]\, dBm$$

7. Driver Controllable Amplifier RX1 with minimum gain: 20 dB, Driver Controllable Amplifier RX2 with full gain: 25 dB, Driver Controllable Amplifier RX3 with full gain: 25 dB

$$P_{RX} = [-90.3, -31.3] + 20 - 0.3 - 0.3 + 25 - 0.3 + 13 + 25 = [-21.2, 37.8]\, dBm$$

8. Driver Controllable Amplifier RX1" with full gain: 40 dB, Driver Controllable Amplifier RX2 with full gain: 25 dB, Driver Controllable Amplifier RX3 with full gain: 25 dB

$$P_{RX} = [-90.3, -31.3] + 20 - 0.3 - 0.3 + 25 - 0.3 + 13 + 25 = [-1.2, 57.8]\, dBm$$

Taking into account the maximum and minimum values for the eight cases we have in the RF_OUT point a received power in the range -45.2 dBm and 57.8 dBm (without the filters) and between -56.2 dBm 46.8 dBm (with the filter PBF1). Therefore without the Sensitive Time Control we manually set the amplifiers gain in order to achieve a maximum power at the RF_OUT point of 10 dBm as requested and to operate in safety condition. Under this assumption we cannot use the external amplifier. In the next table are represented the operative conditions and the relative warning due to an excessive power.

	Driver Amplifier 1 Gain [dB]	***OP1 Driver Amplifier 2 check***	***Driver Amplifier 2 Gain [dB]***	***OP1 Driver Amplifier 3 check***	***Driver Amplifier 3 Gain [dB]***
STC OFF	20	OK	13	OK	13
	40	OK	13	**Warning**	13
	20	OK	25	OK	13
	40	OK	25	**Warning**	13
	20	OK	13	OK	25

	40	OK	13	OK	25
	20	OK	25	OK	25
	40	OK	25	**Warning**	25

Table 6.4 Amplification strategy and warning - STC OFF

The next figures report examples of the before mentioned concept.

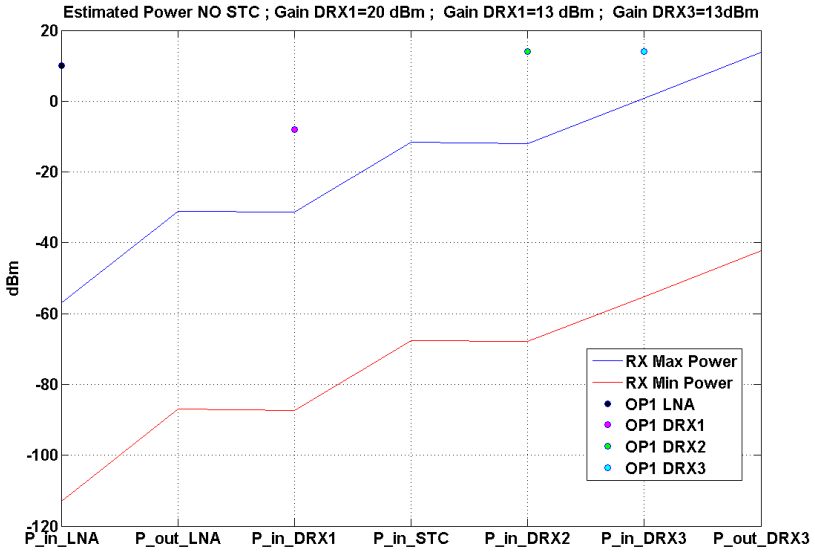

Figure 6.8 Example of Estimated power without Sensitive Time Control

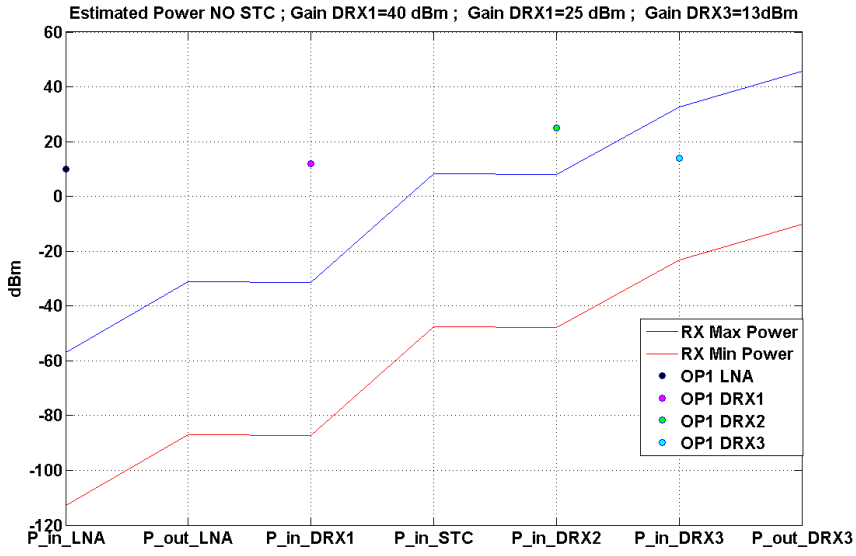

Figure 6.9 Example of Estimated power without Sensitive Time Control

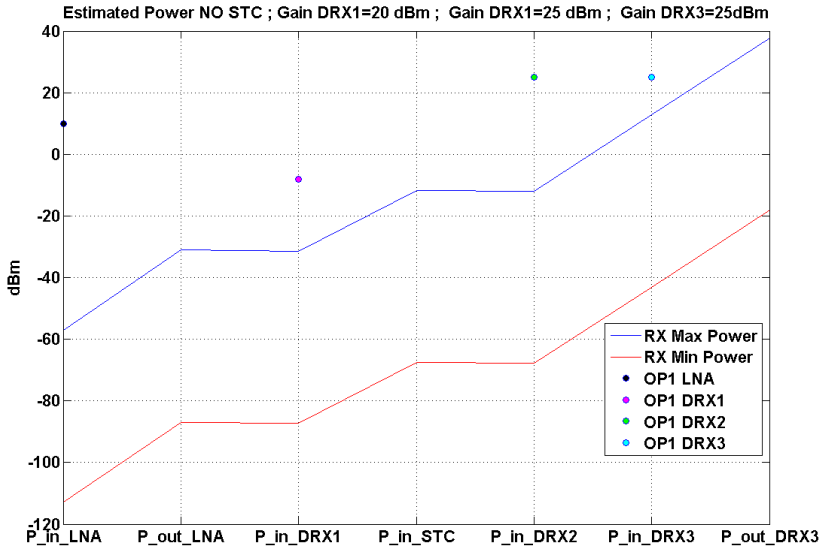

Figure 6.10 Example of Estimated power without Sensitive Time Control

In the following text a summary of the selected devices with their relative characteristics used in the RF radar front-end are reported. The summary will be organized in five different sections:

- Antenna & Circulator

Configuration	1 mt parabolic reflector horn special feed
Frequency Range [GHz]	9.5 – 10.7
Gain [dB]	30 dBi @ 9.5 Gz
Beam Width	Flat top topped 6° @ -3 dB
Interface	WR90

Table 6.5 Antenna Parameters

Material	Aluminum
Frequency Range [GHz]	9.5 – 10.7
Power [W]	120 CW
Isolation [dB]	30

Insertion Loss [dB]	0.1
Interface	WR90

Table 6.6 Circulator Parameters

- Power Amplifier & Low Noise Amplifier

Frequency Range [GHz]	9.5 – 10.7
RF Output Power [W]	100
Small Signal Typical Gain [dB]	56
Duty Cycle	0 – 100%
RF Pulse Rise Time [nsec]	30
RF Pulse Fall Time [nsec]	26
Max RF input Power [dBm]	**3**
Noise Power Density ON [dBm/MHz]	**-26**
Noise Power Density OFF [dBm/MHz]	**-90**
Typical Wide Band Spurious [dBc]	**-70**
Phase Noise Denisty [dBc/Hz]	**-120 @ 10 KHz**
	-125 @ 100 KHz
	-130 @ 1 MHz

Table 6.7 Mini TWT Power Amplifier

Frequency Range [GHz]	9.5 – 10.7
Gain min [dB]	26
Gain Flatness [dB]	± 0.5
Noise Figure [dB]	0.9
Output P1dB [dBm]	10
IP3 [dBm]	20
Impedance [Ω]	50

Table 6.8 Low Noise Amplifier

- Driver Amplifier

Frequency Range [GHz]	9.5 – 10.7
Gain [dB]	40
Gain Control Range [dB]	0-20
Gain Control Type	DC Voltage – Non Linear Control
Output P1dB [dBm]	12 min
Noise Figure [dB]	4 @ full gain

Table 6.9 Driver Controllable Amplifier

Frequency Range [GHz]	6 – 12
Gain [dB]	25
Gain Control Range [dB]	0-12
Gain Control Type	DC Voltage – Non Linear Control
Output P1dB [dBm]	25 max
	14 min
Noise Figure [dB]	3.2 @ no gain control
	7 @ gain control

Table 6.10 Driver Controllable Amplifier

- Pin Diode Attenuator & Pin Diode Switch

Frequency Range [GHz]	9.8 – 10
Attenuation Range [dB]	64
Attenuation Control [V]	0 - 6 VDC non linear
Phase Error [deg]	±15 @ -64 dB
Amplitude Error [dB]	±1
Insertion Loss [dB]	6

Power [dBm]	10
Harmonic Rejection [dBc]	35 @ 10 dBm
Commutation Speed [nsec]	350

Table 6.11 Pin Diode Attenuator

Frequency Range [GHz]	8 – 11
Input Power [dBm]	20 max
Insertion Loss [dB]	2.5
Isolation [dB]	90 min
Switch Speed [nsec]	50
Control	TTL

Table 6.12 Pin Diode Attenuator

Frequency Range [GHz]	9.5 – 10.7
Input Power [W]	120 CW
Insertion Loss [dB]	1.5
Isolation [dB]	40 min
Switch Speed [nsec]	300
Control	TTL

Table 6.13 Pin Diode Attenuator

- Waveguide Filters

Center Frequency [GHz]	9.9
Bandwidth [MHz]	10
Insertion Loss [dB]	4.5
Rejection [dB]	40 @ f_0 ± 30 MHz
Rejection 2^{th} 3^{th} harmonics [dB]	40
Group Delay [nsec]	62

Table 6.14 Receviver Waveguide Filter

Center Frequency [GHz]	9.9
Bandwidth [MHz]	2
Insertion Loss [dB]	11
Rejection [dB]	40 @ $f_0 \pm 10$ MHz
Rejection 2^{th} 3^{th} harmonics [dB]	40
Group Delay [nsec]	177

Table 6.15 Receviver Waveguide Filter

Figure 6.11 X-band RF transmitter chain front (left) and rear (right)

Figure 6.12 X-band RF receiver chain section 1; front (left) and rear (right)

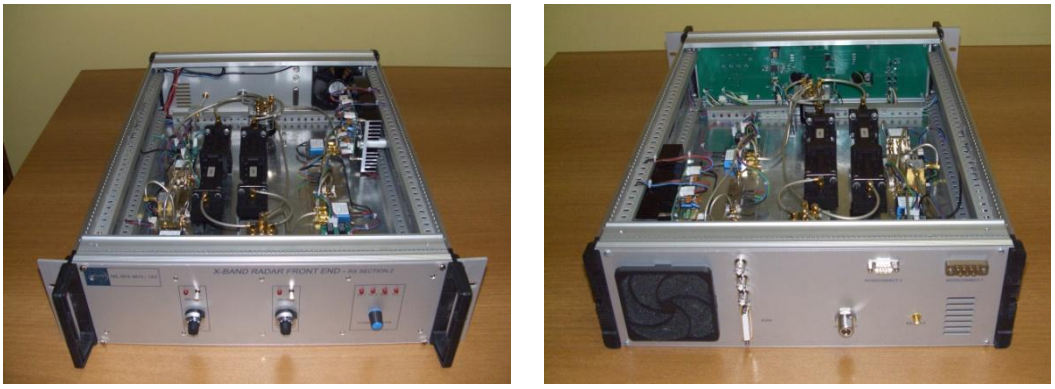

Figure 6.13 X-band RF receiver chain section 2; front (left) and rear (right)

CONCLUSIONS

Microwave photonic aims to combine radio and light waves technologies for synergistic operations between the millimeters\sub-millimeters and infrared regions. In the last two decades MWP has becoming an interesting and growing research field where, both civil and military applications could directly benefit from. Key advantages of a MWP system with respect to MIC are high speed and high bandwidth, very high dynamic range, reduced cost, size and weight, low power consumption and costant attenuation, reliability, tunability and high immunity to the electromagnetic interferences. Historical developments of MWP systems are in the field of analog microwave photonic link, antenna remoting and true time delay beamforming for phased array antenna and electronic warfare applcations. Recent improvements in device's fabrication open intriguing applications including high frequency and low noise photonic microwave and Therahertz signal generation, microwave photonic signal processing, photonic analog to digital converters and high data rate broadband wireless access networks.

The objective of this thesis was the study, development, realization and testing of MWP demonstrators and prototypes for a frequency\waveforms agile, digital and wideband radar\telecommunications system. After a brief introduction on the MWP concepts and devices in the first two chapters, experiments and results on the photonic signal generation, analog to digital conversion and microwave photonic up\down conversions have been presented.

The architecture of a photonic reconfigurable microwave signal generator has been presented in sections 3.1. It is based on the beating in a photodiode of two laser modes coming from an ultra stable MLL. Results up to 40GHz show excellent spectral purity compared to a state of the art synthesizer showing that the optically generated signals are characterized by lower phase noise at high offset frequency, and by comparable amplitude fluctuations. The stability performances in terms of time jitter of the RF source have been evaluated at 10 and 40 GHz. The jitter values integrated over the entire range are around 510fs, increasing to about 530fs at 40 while integrating from 5kHz, the time jitter drops down to around 4fs.

Than two innovative techniques for optically generating phase-modulated RF pulses, (suitable for wideband modulation) with flexible and stable carrier, have been presented in sections 3.2 and 3.3. Both the proposed schemes exploit a commercial device: a standard MZM (3.2), and a dual-parallel MZM (3.3), and they can generate softwaredefined amplitude/phase-coded signals allowing a new generation of advanced radio systems with reduced complexity and cost. In the first set up a high-quality DDS permits the generation of software-defined modulating signals (at intermediate frequency) which are transferred to the modes of a MLL by means of a standard MZM, without affecting their reciprocal phase stability. Therefore after detecting the optical signal, phase modulated RF pulses can be obtained close to any multiple frequency of the laser repetition rate, even at frequency in the EHF band. Finally a set of RF filters can select the radar signal at the desired carrier frequency. The carriers can be generated simultaneously or alternately, or even changed continuously. The modulating signal can also be changed meanwhile, implementing a waveform diversity technique. A demonstration has been made by applying code sequences or linear frequency modulation at about 10GHz and 40GHz with a time jitter on the RF carrier of about 14.2fs for the optically generated carriers and 15.3fs for the conventionally generated once, confirming the noise performance of the proposed scheme. The technique implemented in the second scheme exploits an optical I/Q modulator driven by a low-sample rate and low-noise DDS to modulate the phase of only one mode of the filtered MLL. The two laser modes are then heterodyned in a PD, and a RF pulse is properly filtered out. multilevel or binary coded sequences can be easily generated in this set up, a chirped signal is limited in bandwidth because the maximum frequency deviation is proportional to a multiple of the Vπ of the I\Q MZM. In this case modulations have been applied at 25GHz of carrier frequency with a timing jitter of 286fs over the entire offset frequency range.

A photonic jitter limited sampling system with electrical quantization has been presented, in the paragrpah 4.1. It is based on low jitter optical pulses provided by a MLL with subsequennt four time-interleaved channels. Since higher sampling system is achievable (by easily scaling the system for larger signal BW) it represents flexible acquisition system for software defined radio applications. System performances have been tested with RF signals over a large frequency range, demonstrating a high level of precision (greater than 7 bits) up to 40GHz. The results show that the scheme is fundamentally limited by the sampling jitter and it approaches the theoretical limits for the considered signal frequencies. Further improving the ER of the switching matrix, and making use of a differential detection, would increase the system precision pushing it even closer to the theoretical limits imposed by the MLL timing jitter. In the paragraph 5 a high performance UWB photonic-assisted multi-band up\down-conversion of sparse wireless signals has been demostrated. It is easily based on the modulation of the laser modes of a MLL in a MZM, followed by the heterodyning of the optical

signal in a photodetector. Conversion of RF signals up to the MMB has been achieved thanks to the large optical spectrum of the MLL and to the wide electro-optical bandwidth of the MZM and of the PD. The presented system has been tested up to 26.5GHz, with a maximum power penalty lower than 0.5dB with respect to the signal generated directly at high frequencies or low frequency, keeping high the quality of the signals both in transmission and reception

Finally in the chapter 6 the radar system requirements for a photonic-based full digital radar system operating at X-band have been presented. Furthermore the opto-electronic and radio frequency sub-systems implementations and characteristics have been discussed and detailed.

REFERENCES

[1] Seeds, A., Lee, C. H., Funk, E. & Nagamura, M. Guest editorial: Microwave photonics. J. Lightwave Technol. 21, 2959−2960 (2003).

[2] Seeds, A. Microwave photonics. IEEE Trans. Microwave Theory Tech. 50, 877−887 (2002).

[3] Cox. C.H., Ackerman E. I., Microwave Photonics: past, present and future, Photonics Systems, Inc. Billerica, MA, USA.

[4] Camapny J., Novak D., Microwave Photonics combies two worlds, Nature Photonics, Vol 1, June 2007.

[5] Bach, L. et al. Enhanced direct-modulated bandwidth of 37 GHz by a multi-section laser with a coupled-cavity-injection-grating design. Electron. Lett. 39, 1592−1593 (2003).

[6] Chrostowski, L. et al. 50-GHz optically injection-locked 1.55-μm VCSELs. IEEE Photon. Technol.Lett. 18, 367−369 (2006).

[7] Dolfi , D. W. & Ranganath, T. R. 50 GHz velocity-matched broad wavelength LiNbO3 modulator with multimode active section. Electron. Lett. 28, 1197−1199 (1992).

[8] Spickermann, R., Sakamoto, S. R., Peters, M. G. & Dagli, N. GaAs/AlGaAs traveling wave electro-optic modulator with electrical bandwidth greater than 40 GHz. Electron. Lett. 32, 1095−1096 (1996).

[9] Wey, Y. G. et al. 110-GHz GaInAs/InP double heterostructure p-i-n photodetectors. J. Lightwave Technol. 13, 1490−1499 (1995).

[10] Umbach, A., Trommer, D., Mekonnen, G. G., Ebert, W. & Unterborsch, G. Waveguide integrated 1.55-μm photodetector with 45 GHz bandwidth. Electron. Lett. 32, 2143−2145 (1996).

[11] Giboney, K. S. et al. Travelling-wave photodetectors with 172-GHz bandwidth and 76-GHz bandwidth-effi ciency product. IEEE Photon. Technol. Lett. 7, 412−414 (1995).

[12] Ishibashi, T. et al. Uni-traveling-carrier photodiodes. Tech. Dig. Ultrafast Electron. Optoelectron. 83−87 (1997).

[13] Rachel Won, Microwave Photonic Shines, Interview Technology Focus, Nature Photonics, Vol 5, December 2011.

[14] Roberto Llorente and Marta Beltrán, “Radio-over-Fibre Techniques and Performance”.

[15] Yao J., “A Tutorial on Microwave Photonics”.

[16] Revision of part 15 of the commission’s rules regarding ultra-wideband transmission systems : ‘New public safety applications and broadband internet access among uses envisioned by FCC authorization of Ultra-Wideband technology’, Report and order, adopted February 14, 2002, released July 15, 2002, http://www.fcc.gov

[17] CEPT Report 017 Report from CEPT to the European Commission in response to the Mandate to: identify the conditions relating to the harmonised introduction in the European Union of radio applications based on ultra-wideband (UWB) Technology, 2007.

[18] J. P. Yao, F. Zeng, and Q. Wang, “Photonic generation of Ultra-Wideband signals,” J. Lightw. Technol., vol. 25, no. 11, pp. 3219–3235, Nov. 2007.

[19] F. Ponzini, F. Cavaliere, G. Berrettini, M. Presi, E. Ciaramella, N. Calabretta, and A. Bogoni, “Evolution scenario toward WDM-PON,” J. Opt. Commun. Netw., vol. 1, no. 4, pp. C25–C34, Sep. 2009.

[20] S. Pan and J. P. Yao, “Provision of IR-UWB wireless and baseband wired services over a WDM-PON,” Opt. Express, vol. 19, no. 26, pp. B209–B217, Dec. 2011.

[21] “WiGig White Paper”, http://wigig.org/specifications.

[22] S. Yaalob, W. R. Wan Abdullah, M. N. Osman, A. K. Zamzuri, R. Mohamad, M. R. Yahya, A. F. Awang Mat, M. R. Mokhtar, and H. A. Abdul Rashid, “Effect of laser bias current to the third order intermodulation in the radio over fibre system,” RF and Microwave Conference, Sept. 2006, pp. 444–447.

[23] D. Hassin and R.Vahldieck, “Feedforward linearization of analog modulated laser diodes—Theoretical analysis and experimental verification,” IEEE Trans. Microw. Theory Tech., vol. 41, no. 12, pp. 2376–2382, Dec. 1993.

[24] L. Roselli, V. Borgioni, F. Zepparelli, F. Ambrosi, M. Comez, P. Faccin, and A. Casini, “Analog laser predistortion for multiservice radio-over-fiber systems,” J. Lightw. Technol., vol. 21, no. 5, pp. 1211–1223, May 2003.

[25] A. Katz, W. Jemison, M. Kubak, and J. Dragone, “Improved radio over fiber performance using predistortion linearization,” in IEEE MTT-S Int. Microw. Symp. Dig., Philadelphia, PA, Jun. 2003, pp. 1403–1406.

[26] V. Magoon and B. Jalali, “Electronic linearization and bias control for externally modulated fiber optic link,” in IEEE Int. Microw. Photon. Meeting, Oxford, U.K., Sep. 2000, pp. 145–147.

[27] J. H. Schaffner and W. B. Bridges, “Inter-modulation distortion in high dynamic range microwave fiber-optic links with linearized modulators,” J. Lightw. Technol., vol. 11, no. 1 pp. 3–6, Jan. 1993.

[28] E. I. Ackerman, “Broad-band linearization of a Mach–Zehnder electrooptic modulator,” IEEE Trans. Microw.Theory Tech., vol. 47, no. 12, pp. 2271–2279, Dec. 1999.

[29] M.L. Skolnik, Introduction to radar systems, 2nd Ed., McGraw-Hill, New York, 1980.

[30] Hamish Meikie, Modern Radar Systems, Artech House, Boston, 2001.

[31] Ng, W. et al. Th e fi rst demonstration of an optically steered microwave phased array antenna using true-time-delay. IEEE J. Lightwave Technol. 9, 1124−1131 (1991).

[32] Esman, R. D. et al. Fiber-optic prism true time-delay antenna feed. IEEE Photon. Technol. Lett. 5, 1347−1369 (1993).

[33] Molony, A., Edge, C. & Bennion, I. Fibre grating time delay element for phased array antennas. Electron. Lett. 31, 1485−1486 (1995).

[34] Zmuda, H., Soref, R., Payson, P., Johns, S. & Toughlian, E. N. Photonic beamformer for phased array antennas using fibre grating prism. IEEE Photon. Technol. Lett. 9, 241−243 (1997).

[35] Roman, J. E., Frankel, M. Y., Matthews, P. J. & Esman, R. D. Time-steered array with a chirped grating beamformer. Electron. Lett. 33, 652−653 (1997)

[36] Corral, J. L., Marti, J. & Fuster, J. M. in Dig. IEEE Microwave Th eory Tech. Symp. Baltimore, Maryland, USA 1379−1382 (1998).

[37] Y. Liu, J. Yang, and J. P. Yao, “Continuous true-time-delay beamforming for phased array antenna using a tunable chirped fiber grating delay line,” IEEE Photon. Technol. Lett., vol. 14, no. 8, pp. 1172–1174, Aug. 2002.

[38] B. M. Jung, J. D. Shin, and B. G. Kim, “Optical true time-delay for two-dimensional X-band phased array antennas,” IEEE Photon. Technol. Lett., vol. 19, pp. 877–879, Jun. 2007.

[39] B. M. Jung and J. P. Yao, “A two-dimensional optical true time-delay beamformer consisting of a fiber Bragg grating prism and switch-based fiber-optic delay lines,” IEEE Photon. Technol. Lett., vol. 21, no. 10, pp. 627–629, May 2009.

[40] Dispenza, M. et al.: Tuneable optoelectronic oscillator based on a frequency shifter, in Proc. of the 6th European Radar Conf., 2009, paper 262.

[41] Song, S.-C.; Hong, Y.-S.: A new approach for evaluating the phase noise requirements of STALO in a Doppler radar, in Proc. of the 37th European Microwave Conf., October 2007, Munich, Germany.

[42] U. Gliese, T. N. Nielsen, S. Nørskov, and K. E. Stubkjaer, "Multifunctional fiber-optic microwave links based on remote heterodyne detection," IEEE Trans. Microwave Theory Tech., vol. 46, no. 5, pp. 458-468, May 1998.

[43] J. Sun, Y. Dai, X. Chen, Y. Zhang, and S. Xie, "Stable dual-wavelength DFB fiber laser with separate resonant cavities and its application in tunable microwave generation," IEEE Photon. Technol. Lett., vol. 18, no. 24, pp. 2587-2589, Dec. 2006.

[44] Goldberg, L.; Taylor, H.F.; Weller, J.F.; Bloom, D.M.: Microwave signal generation with injection laser diodes. Electron. Lett., 19 (13) (1983), 491−493.

[45] Z. F. Fan and M. Dagenais, "Optical Generation of a mHz- Linewidth microwave signal using semiconductor lasers and a discriminator-aided phase-locked loop," IEEE Trans. Microwave Theory Tech., vol. 45, no. 8, pp. 1296-1300, Aug. 1997.

[46] J. J. O'Reilly, P. M. Lane, R. Heidemann, and R. Hofstetter, "Optical generation of very narrow linewidth millimeter wave signals," Electron. Lett., vol. 28, no. 25, pp. 2309–2311, 1992.

[47] J. J. O'Reilly and P. M. Lane, "Fiber-supported optical generation and delivery of 60 GHz signals," Electron. Lett., vol. 30, no. 16, pp. 1329–1330, 1994.

[48] P. Shen, N. J. Gomes, P. A. Davies, W. P. Shillue, P. G. Huggard, and B. N. Ellison, "High-purity millimeter-wave photonic local oscillator generation and delivery," in Proc. Int. Microwave Photonics Topical Meeting, Sep. 10–12, 2003, pp. 189–192.

[49] G. Qi, J. P. Yao, J. Seregelyi, C. Bélisle, and S. Paquet, "Generation and distribution of a wide-band continuously tunable mm-wave signal with an optical external modulation technique," IEEE Trans. Microw. Theory Tech., vol. 53, no. 10, pp. 3090- 3097, Oct. 2005.

[50] W. Li and J. P. Yao, "Microwave frequency multiplication using two cascaded Mach-Zehnder modulators," 2009 Asia- Pacific Microwave Photonics Conference, Beijing, China, 22-24 April 2009.

[51] A. Wiberg, P. P-Millán, M. V. Andrés, and P. O. Hedekvist, "Microwave-photonic frequency multiplication utilizing optical four-wave mixing and fiber Bragg gratings," J. Lightw. Technol., vol. 24, no. 1, pp. 329–334, Jan. 2006.

[52] Q. Wang, H. Rideout, F. Zeng, and J. P. Yao, "Millimeterwave frequency tripling based on four-wave mixing in a semiconductor optical amplifier," IEEE Photon. Technol. Lett., vol. 18, no. 23, pp. 2460-2462, Dec. 2006.

[53] H. Rideout, J. Seregelyi, S. Paquet, and J. P. Yao, "Discriminator-aided optical phase-lock loop incorporating a frequency down-conversion module," IEEE Photon. Technol. Lett., vol. 18, no. 22, pp. 2344-2346, Nov. 2006.

[54] X. Chen, Z. Deng, and J. P. Yao, "Photonic generation of microwave signal using a dual-wavelength singlelongitudinal-mode fiber ring laser," IEEE Trans. Microw. Theory Tech., vol.54, no. 2, pp. 804-809, Feb. 2006.

[55] Yilmaz, T., DePriest, C. M., Turpin, T., Abeles, J. H. & Delfyett, P. J. Toward a photonic arbitrary waveform generator using modelocked external cavity semiconductor laser. IEEE Photon. Technol. Lett. 14, 1608−1610 (2002).

[56] McKinney, J. D., Leaird, D. E. & Weiner, A. M. Millimeter-wave arbitrary waveform generation with a direct space-to-time pulse shaper. Opt. Lett. 27, 1345−1347 (2002).

[57] Chou, J., Han, Y. & Jalali, B. Adaptive RF-Photonic arbitrary waveform generator. IEEE Photon. Technol. Lett. 15, 581−583 (2003).

[58] R.Walden, "Analog-to-digital conversion in the early twenty-first century," Wiley Encyclopedia of Computer Science and Engineering, (Wiley, 2008).

[59] Workshop on ultrafast analog-to-digital (A/D) converters., Proc. IEEE MTT-S Int. Microwave Symp. (2004).

[60] Marc Carrei, "High-Performance Photonic Analog-lo-Digital Converter and Low-Noise Mode-Locked Fiber Lasers", Naval Research Laboratory, NRLIMlRI650w-03-8679, Washington, DC 20375-5320.

[61] J. U. Kang and R. D. Esman, "Demonstration of time-interweaved photonic four-channel WDM sampler for hybrid analogue–digital converter," Electron. Lett., vol. 35, pp. 60–61, 1999.

[62] T. R. Clark, J. U. Kang, and R. D. Esman, "Performance of a timeand wavelength-interleaved photonic sampler for analog–digital conversion," IEEE Photon. Technol. Lett., vol. 11, pp. 1168–1170, Sept. 1999.

[63] A. S. Bhushan, F. Coppinger, S. Yegnanarayanan, and B. Jalali, "Non-dispersive wavelength-division sampling," Opt. Lett., vol. 24, pp. 738–740, 1999.

[64] F. Coppinger, A. S. Bhushan, and B. Jalali, "12 Gsample/s wavelength division sampling analogue-to-digital converter," Electron. Lett., vol. 36, pp. 316–318, 2000.

[65] R.C. Williamson et al., "Effects of crosstalk in a demultiplexers for photonic analog-to-digital converters," J. Lightwave Technol., v.19, pp. 230-236 (2001).

[66] T.R. Clark et al., "Digitally linearized wideband photonic link," Journal of Lightwave Technology, vol. 19, issue 2, 172-179 (2001).

[67] Minasian, R. A. Photonic signal processing of microwave signals. IEEE Trans. Microwave Th eory Tech. 54, 832−846 (2006).

[68] Pastor, D., Ortega, B., Capmany, J., Fonjillaz, P.-Y. & Popov, M. Tunable microwave photonic fi lter for noise and interference suppression in UMTS base stations. Electron. Lett. 40, 997−999 (2004).

[69] Sugiyama, T., Suzuki, M. & Kubota, S. An integrated interference supression scheme with adaptative equalizer for digital satellite communication systems. IEICE Trans. Commun. E79-B, 191−196 (1996).

[70] José Capmany, Beatriz Ortega, Daniel Pastor, "A Tutorial on Microwave Photonic Filters", J. Lightwave Technol, Vol. 24, No. 1, January 2006.

[71] R. Paschotta et al., "Picosecond pulse sources with multi-GHz repetition rates and high output power", New J. Phys. 6, 174 (2004).

[72] Ch. Spielmann, "Ultrabroadband femtosecond lasers", IEEE J. Quantum Electron. 30 (4), 1100 (1994)

[73] David Larsson, "Fabrication and characterization of low noise monholitic mode locked laser", PhD Thesis.

[74] Stavros Iezekie," Microwave Photonics: Devices and Applications", IEEE Computer Society Press, 2009.

[75] Chi. H. Lee, "Microwave Photonics", CRC Press, 2007.

[76] A. Vilcot, B. Capon, J. Chazelas, "Microwave Photonics: from components to applications and systems", Kluwer Academic Publisher, 2010

[77] Edward I. Ackerman e Charles H. Cox III – RF Fiber-Optic Link

[78] Charles Cox III, Gary Betts, Leonard M. Johnson – An Analytic and Experimental Comparison of Direct and External Modulation in Analog Fiber-Optic Links, IEEE Transactions on Microwave Theory and Techniques, VOL.38, N° 5, May 1990 Performance, IEEE Microwave Magazine, December 2001.

[79] Enrico Maria Fabbri, "Progetto, Realizzazione e caratterizzazione di un Collegamento Analogico in Fibra Ottica per Applicazioni Radioastronomiche", Master Degree Thesis, 2004.

[80] Jason D. McKinney, Keith J. Williams, "Analog Photonic Links for Built-in-Testing of Electronicm Support Measures (ESM) Systems" Naval Research Laboratory, Washington DC, 20375-5320, NRL/MR/5652--09-9194.

[81] F. Bucholtz, V. J. Urick, M. Godinez, and K. J. Williams, "Graphical approach for evaluating performance limitations in externally modulated analog photonic

links," IEEE Trans. Microwave Theory Tech., vol. 56, no. 1, pp. 242–247, Jan. 2008.

[82] Edward I. Ackerman, "The "Effective" Gains and Noise Figures of Individual Components in an Analog Photonic Link".

[83] M. C. Kemp 'Millimetre Wave and Terahertz Technology for the Detection of Concealed Threats – A Review', Proc SPIE 6402, 2006.

[84] V. Ravenni, "Performance evaluations of frequency diversity radar system", European Microwave Conference 2007, pp. 1715-1718, Dec. 2007.

[85] G. Serafino, P. Ghelfi, G.E. Villanueva, J. Palaci, P. Pérez-Millán, J-L-Cruz, C. Porzi, A. Bogoni, "Stable optically generated RF signals from a fibre mode-locked laser", IEEE Photonics Society Annual Meeting 2010, TuK4, Denver, Co, USA.

[86] Z. Li, W. Li, H. Chi, X. Zhang, J. Yao, "Photonic Generation of Phase-Coded Microwave Signal With Large Frequency Tunability", IEEE Photonics Technology Letters, vol. 23, no. 11, pp. 712-714, June 2011.

[87] H. Chi and J. P. Yao, "An approach to photonic generation of highfrequency phase-coded RF pulses," IEEE Photon. Technol. Lett., vol. 19, no. 10, pp. 768–770, May 15, 2007.

[88] Ghelfi, P.; Serafino, G.; Berizzi, F.; Bogoni, A.: Generation of highly stable microwave signals based on regenerative fiber mode locking laser, Proc of Laser and Electro-Optics Conference, CLEO 2010.

[89] Cox, C.H. III: Limits on the performance of RF-over fiber links and their impact on device design. IEEE Trans. Microw. Theory Tech., 54 (2) (2006), 906−920.

[90] Bogoni, A.; Berizzi, F.: PHOtonic-based Full Digital Radar, Tech. Rep. WP1-Feasibility Study, National Lab of Photonic Network and RaSS Center, 2009.

[91] MAXIM: Clock (CLK) Jitter and Phase Noise Conversion, Application Note 3359, December 10, 2004.

[92] Walt Kester: Converting Oscillator Phase Noise to Time Jitter, Analog Device MT-008 Tutorial.

[93] L. Banchi, F. Rossi, M. Ferianis, A. Bogoni, L. Potì, P. Ghelfi, "Synchronization of 3GHz repetition rate harmonically mode-locked fiber laser for optical timing applications", Proceedings of DIPAC 2007, Italy.

[94] Serafino, G. et al.: Photonic Generation of RF Multiple Carriers Using a Mode-Locked Laser and a Single Photodiode, Paper Number 7960-27, Photonics West, San Francisco 2010.

[95] P.J. Delfyett, S. Gee, F. Quinlan, P. Juodawlkis, J. Plant, “Low noise and stabilized mode-locked diode lasers for arbitrary waveform generation”, IEEE Lasers and Electro-Optics Society Annual Meeting, 2008, LEOS 2008.

[96] M.U. Piracha, D. Nguyen, D. Mandridis, T. Yilmaz, I. Ozdur, S. Ozharar, P.J. Delfyett, “Range resolved lidar for long distance ranging with sub-millimeter resolution”, Optics Express, Vol. 18, No. 7, pp. 7184-7189, March 2010.

[97] S. Cheung, J. Baek, R.P. Scott, N.K. Fontaine, F.M. Soares, X. Zhou, D.M. Baney, S.J. Ben Yoo, "1-GHz Monolithically Integrated Hybrid Mode-Locked InP Laser", IEEE Photonics Technology Letters, vol. 22, no. 24, pp.1793-1795, Dec 2010.

[98] P. Pérez-Millán, A. Wiberg, P. O. Hedekvist, P. A. Andrekson, and M. V. Andrésa, “Optical demultiplexing of millimeter-wave subcarriers for wireless channel distribution employing dual wavelength FBGs,” Opt. Commun., vol. 275, no. 2, pp. 335–343, Jul. 2007.

[99] K. Sasagawa, M. Tsuchiya, "Low-Noise and High-Frequency Resolution Electrooptic Sensing of RF Near-Fields Using an External Optical Modulator," J. Lightwave Technol. 26, pp. 1242-1248, 2008.

[100] Dong-Joon Lee and J. F. Whitaker, "Bandwidth enhancement of electro-optic field sensing using photonic down-mixing with harmonic sidebands," Opt. Express 16, pp. 14771-14779, 2008.

[101] G. Serafino, P. Ghelfi, G.E. Villanueva, J. Palací, P. Pérez-Millán, J.L. Cruz, C. Porzi, A. Bogoni, “Stable Optically Generated RF Signals from a Fibre Mode-Locked Laser”, IEEE Photonics Society Annual Meeting 2010, TuK4, Denver, Co, USA.

[102] G.C. Valley, “Photonic analog-to-digital converters,” Opt. Express, vol. 15(5), pp. 1995-1982 (2007).

[103] J. Elbornsson et al., “Blind equalization of time errors in a time-interleaved ADC system,” IEEE Trans. Signal Processing, v.53, n.4, 2005.

[104] A. Khilo et al., “Photonic ADC: overcoming the bottleneck of electronic jitter,” Opt. Express, vol. 20(4), pp. 4454-4469 (2012).

[105] J. Chou et al., “Photonic bandwidth compression front end for digital oscilloscopes,” IEEE J. Lightwave Technol., v.27, n.22, 2009.

[106] Seeds, A. J. et al., “Microwave Photonics”, JLT, vol. 24, Issue 12, p. 4628 – 4641, Dec. 2006.

[107] Serafino G. et al., “Phase and Amplitude Stability of EHF-Band Radar Carriers Generated From an Active Mode-Locked Laser”, JLT, vol. 29, Issue 23, p. 3551 – 3559, Dec.1, 2011.

[108] PHODIR WP1 internal report. “System Requirements”

AKNOLEDGMENTS

At the end of my route I would like to thanks people around me during this life period. First of all great acknowledgments go to my tutors, Prof. Fabrizio Berizzi and Eng. Antonella Bogoni for the opportunity to conduct a very exciting and interesting work in this specific field of study. At the same time I have the opportunity to thank all my colleagues from the University of Pisa, the CNIT RaSS & NLPN and the TECIP institute and in particular Dr. Paolo Ghelfi and Eng. Filippo Scotti for the helpful discussions and the huge collaboration.

Finally, special thank goes to my mother Loredana and my family for their unconditional support and for believing in me, to my girlfriend Giulia for her constant presence in my life and to Mauro and Rossana for making me feel at home.

LIST OF PUBLICATIONS

Patent

1. P. Ghlefi, F.Scotti, F. Laghezza, A. Bogoni. “Photonics Generation of High-Stability Amplitude/Phase-Coded Multi-Carrier RF Pulses with Carrier Frequency Agility for Software-Defined Radio applications” – P35908.

Prize

2. F. Laghezza, Short-listed at 2012 IET International Radar Conference best student paper, Glasgow, United Kingdom
3. F. Laghezza Keynote speech selection for the Optronic in Defence and Security Conference (OPTRO), Paris, France.

Journal

4. G Pupillo, E Salerno, S Pluchino, M Bartolini, S Montebugnoli, M Di Martino, S Righini, F Schilli O, F Berizzi, E Dalle Mese, F Laghezza, A Konovalenko, A Nabatov, “A potential Italian radar network for NEO and space debris observations”, Mem. S.A.It. Suppl. Vol. 16, 59, 2011
5. F. Laghezza, F. Berizzi, A. Capria, A. Cacciamano, P. Ghelfi, G. Serafino, A. Bogoni. “Reconfigurable Radar Transmitter Based on Photonic Microwave Signal Generation”. INTERNATIONAL JOURNAL OF MICROWAVES AND WIRELESS TECHNOLOGIES Volume 3, Special Issue 03, pp 383-389. 2011.
6. Ghelfi P. Scotti F., Laghezza F., Bogoni A.,"Photonic Generation of Phase-Modulated RF Signals for Pulse Compression Techniques in Coherent Radars", JOURNAL OF LIGHTWAVE TECHNOLOGY, vol. 30, Page(s): 1638-1644, 2012
7. Ghelfi P., Scotti F., Laghezza F., Bogoni A., "Phase Coding of RF Pulses in Photonics-Aided Frequency-Agile Coherent Radar Systems", IEEE JOURNAL OF QUANTUM ELECTRONICS, vol. 48, Page(s): 1151-1157, 2012
8. Ghelfi P., Scotti F., Serafino G. Laghezza F., Bogoni A. “Flexible receiver for multiband orthogonal frequency division multiplexing signals at the millimeter waveband based on optical downconversion”, OPTICS LETTERS / Vol. 37, No. 18 / September 15, 2012.

Conferences

9. F. Laghezza, F. Berizzi, A. Capria, E. Dalle Mese, S. Montebugnoli, G. Pupillo, E. Salerno, M. Di Martino. "Italian Bistatic Radar System for Surveillance of space Debris in Low Earth Orbit". IEEE Radar Conference 2010. 2010 May, 10-14, Washington DC (USA).
10. F. Laghezza, F. Berizzi, A. Capria, A.M. Ricci, V. Carulli, R. Trinci. "Low Earth Orbit Space Debris Detection". IEEE GOLD 2010. 2010,April, 29-30, Livorno (taly).
11. F. Laghezza, F. Berizzi, A. Capria, A. Cacciamano, P. Ghelfi, G. Serafino, A. Bogoni. "Reconfigurable Radar Transmitter Based on Photonic Microwave Signal Generation". EUropean RAD ar Conference 2010 (EURAD). Sept/Oct 01 - 02 , Paris (France).
12. F. Laghezza, A. Capria, A. Cacciamano, F. Berizzi, P. Ghelfi, A. Bogoni. "Electro optical radar transmitter chain modelin and simulation". International Radar Symposium (IRS 2011) September 06 - 09 2011, Leipzig (Germany).
13. Laghezza Francesco, Scotti Filippo, Ghelfi Paolo, Bogoni Antonella, "Flexible Photonic Generation of Low Phase Noise Phase Coded Radar Pulses", Optronic in Defence and Security (OPTRO), Paris, France.
14. P. Ghlefi, F.Scotti, F. Laghezza, A. Bogoni. "High-Stability Phase-Coded RF Pulses for Coherent Radars from a Mode-Locking Laser". OFC/NFOEC 2012, March 4-8, 2012 in Los Angeles, California, USA.
15. F.Scotti, F. Laghezza, P. Ghlefi, A. Bogoni. "Photonics Generation of Phase-Modulated RF Pulses with Carrier Frequency Agility for Software Defined Coherent Radar". "OFC/NFOEC 2012, March 4-8, 2012 in Los Angeles, California, USA.
16. P. Ghlefi, F.Scotti, G. Serafino, F. Laghezza, A. Bogoni, "Flexible Multi-Band OFDM Receiver Based on Optical Down-Conversion for Millimeter Waveband Wireless Base Stations" ECOC 2012.
17. F. Laghezza, F. Scotti, P. Ghelfi, F. Berizzi, A. Bogoni "Photonic Generation of Microwave Phase Coded Radar Signal", IET International Radar Co nference 2012.
18. A. Bogoni, P. Ghelfi, G. Serafino, F. Laghezza, F. Scotti "Photonics Techniques for the Flexible Generation of Ultra-Stable Microwave and Millimeterwave Radar Signals" International Photonics and OptoElectronics Meetings (POEM 2012) NOV. 1-2, 2012
19. F. Laghezza, F.Scotti, P. Ghelfi, S. Pinna, and A. Bogoni, "Jitter-Limited Photonic Analog-to-Digital Converter with 7 Effective Bits for Wideband Radar Applications", 2013 International Radar Conference, Ottawa, Canada, May 2013.

This page was intentionally left blank